City Research Online

City, University of London Institutional Repository

Blood Vessel Segmentation and Shape Analysis for Quantification of Coronary Artery Stenosis in CT Angiography

A Thesis Submitted to

City University London, School of Engineering and Mathematical Science

In Full Fulfilment of the Requirements for the Degree

Doctor of Philosophy in

Information Engineering

By

Yin Wang

December, 2011

Contents

List of Figures

ix

List of Tables

Acknowledgements

This thesis could not be completed without the support I have received from many people during my time as a PhD student at City University London. First of all, I would like to express my gratitude to my supervisor Professor Panos Liatsis, for his advice, friendship and encouragement over these years. With his motivating enthusiasm and admirable insights, he has taught me about life, science, friendship and of course image processing. It has been a real pleasure to work with you. I would like to give many thanks to all the members in the lab, for their support, friendship, advice and discussions.

I also would like to acknowledge the support of City University, which enable this research through the award of a University Research Studentship and our collaborators at St Thomas' and Guys' Hospitals for their invaluable advice and for the provision of the CTA datasets.

My last words go to my parents, who always give me unconditional support, love and reassurance. I owe my life and every achievement to them.

Declaration

No portion of the work referred to in this thesis has been submitted in support of an application for another degree or qualification of this or any other university or other institute of learning. I hereby grant powers of discretion to the University Librarian to allow this thesis to be copied in whole or in part without further reference to the author. This permission covers only single copies made for study purposes, subject to normal conditions of acknowledgement.

Abstract

This thesis presents an automated framework for quantitative vascular shape analysis of the coronary arteries, which constitutes an important and fundamental component of an automated image-based diagnostic system. Firstly, an automated vessel segmentation algorithm is developed to extract the coronary arteries based on the framework of active contours. Both global and local intensity statistics are utilised in the energy functional calculation, which allows for dealing with non-uniform brightness conditions, while evolving the contour towards to the desired boundaries without being trapped in local minima. To suppress kissing vessel artifacts, a slice-by-slice correction scheme, based on multiple regions competition, is proposed to identify and track the kissing vessels throughout the transaxial images of the CTA data. Based on the resulting segmentation, we then present a dedicated algorithm to estimate the geometric parameters of the extracted arteries, with focus on vessel bifurcations. In particular, the centreline and associated reference surface of the coronary arteries, in the vicinity of arterial bifurcations, are determined by registering an elliptical cross sectional tube to the desired constituent branch. The registration problem is solved by a hybrid optimisation method, combining local greedy search and dynamic programming, which ensures the global optimality of the solution and permits the incorporation of any hard constraints posed to the tube model within a natural and direct framework. In contrast with conventional volume domain methods, this technique works directly on the mesh domain, thus alleviating the need for image upsampling. The performance of the proposed framework, in terms of efficiency and accuracy, is demonstrated on both synthetic and clinical image data. Experimental results have shown that our techniques are capable of extracting the major branches of the coronary arteries and estimating the related geometric parameters (i.e., the centreline and the reference surface) with a high degree of agreement to those obtained through manual delineation. Particularly, all of the major branches of coronary arteries are successfully detected by the proposed technique, with a voxel-wise error at 0.73 voxels to the manually delineated ground truth data. Through the application of the slice-by-slice correction scheme, the false positive metric, for those coronary segments affected by kissing vessel artifacts, reduces from 294% to 22.5%. In terms of the capability of the presented framework in defining the location of centrelines across vessel bifurcations, the mean square errors (MSE) of the resulting centreline, with respect to the ground truth data, is reduced by an average of 62.3%, when compared with initial estimation obtained using a topological thinning based algorithm.

Notations

This section only lists the important symbols and notations used in this thesis. Symbols and notation not listed here include local symbols, i.e., the definition only covering the localised section, and notation that are introduced to describe concepts.

a	Length of the major axis of ellipse
b	Length of the minor axis of ellipse
φ	Tilt angle of ellipse
$\boldsymbol{u}$	Centre of ellipse
ϑ	Angular parameter
rad	Radius of the search space
ds	Grid size of the search space
d	Average distance between centreline points
m	Solution space size
α	Elasticity weight
β	Stiffness weight
η	External energy weight
γ	Constrained energy weight
c	Axis constraint
$\boldsymbol{v}_i$	i-th moving node on the central axis of the deformable tube
$\boldsymbol{s}$	$s(t)=[x(t),y(t)]$, parameterisation variable
μ	Smoothness weight
ν	Global energy weight

C_0	Initial centreline data obtained through mesh contraction algorithm
N	The number of moving node
Num	The number of suboptimal solutions for each node
$C(\boldsymbol{x})$	A contour identified by $\boldsymbol{x}$ in the continuous domain
ϕ	Level set function
ϕ_t	Level set function at time t
x'	$x'=\phi_x$, 1st-order partial derivative of ϕ along x-direction
y'	$y'=\phi_y$, 1st-order partial derivative of ϕ along y-direction
z'	$z'=\phi_x$, 1st-order partial derivative of ϕ along z-direction
x''	$x''=\phi_{xx}$, 2nd-order partial derivative of ϕ along x-direction
y''	$y''=\phi_{yy}$, 2nd-order partial derivative of ϕ along y-direction
z''	$z''=\phi_{zz}$, 2nd-order partial derivative of ϕ along z-direction
Ω	Image data
$\Omega_{\boldsymbol{x}}$	Localised image centred at position $\boldsymbol{x}$
$\kappa(\boldsymbol{x})$	Local curvature at position $\boldsymbol{x}$
$I(\boldsymbol{x})$	Intensity value at position $\boldsymbol{x}$
$L(\boldsymbol{x})$	A fuzzy label, at position x, measuring the probability of the voxel belonging to the object
$E(C)$	The minimal path energy along the curve C
E_{Int}	The internal energy term of snake-like energy functional
E_{Ext}	The external energy term of snake-like energy functional
E_{Con}	The constraint energy term of snake-like energy functional
$\boldsymbol{p}$	A point in an image
w	The smoothness constant in minimal path energy functional
L	The length of a curve

∇G	The gradient of Gaussian function
f_k	The system function of a dynamic system at time k
h_k	The measurement function of a dynamic system at time k
σ	The intensity variance derived from an image region
λ_k	The k-th eigenvalue of Hessian matrix
$V(\boldsymbol{x})$	Vesselness measurement at $\boldsymbol{x}$
TP	True positive metric
FN	False negative metric
FP	False positive metric
OM	Overlapping metric
(d_H)	Hausdorff distance
tan	Tangent function
sig	Sigmoid function

Publications

The results of the research described in this thesis have been published in the following papers:

[1] Y. Wang and P. Liatsis, "A Fully Automated Framework for Segmentation and Stenosis Quantification of Coronary Arteries in 3D CTA Images," *presented at the Developments in eSystems Engineering*, Abu Dhabi, UAE, 2009, pp. 136-140.

[2] Y. Wang and P. Liatsis, "An Automated Method for Segmentation of Coronary Arteries in Coronary CT Imaging," *in Proc. of Third International Conference on Developments in eSystems Engineering (DeSE '2010)*, London, United Kingdom, 2010, pp. 12-16.

[3] Y. Wang and P. Liatsis, "Automated Segmentation of Coronary Arteries in 3D CTA Images by Considering Kissing Vessel Artifacts," *IEEE Transactions on Information Technology in BioMedicine*, Submitted for Review, 2011.

[4] Y. Wang and P. Liatsis, "3D Quantitative Vascular Shape Analysis for Arterial Bifurcations via Dynamic Tube Fitting," *IEEE Transactions on Biomedical Engineering*, Accepted, 2011.

Chapter 1

Introduction

This thesis presents the development of a fully automated framework for segmentation and quantitative vascular shape analysis of the coronary arteries based on coronary Computed Tomography Angiography (CTA) images, which constitutes an essential and fundamental component of a computer-aided system for the early diagnosis of coronary artery disease. In this chapter, we commence with a brief introduction of the clinical background associated to this research, including the anatomy of the heart and coronary arteries, coronary artery disease as well as the diagnostic imaging procedures for the assessment of coronary artery disease in Sections 1.1-1.3. Finally, an outline of the thesis is given in the final section of this chapter, Section 1.4.

1.1 Anatomy of the Heart and Coronary Arteries

The heart, positioned within the mediastinum, is the centre of the circulatory system. It is composed of cardiac muscle tissue, which continuously contracts and relaxes, and requires a constant supply of oxygen and nutrients in order to keep continuous blood circulation. Coronary arteries are the network of blood vessels that pump blood to the myocardium (the heart muscle) to feed it with oxygen and nutrients [1]. As illustrated in Fig. 1, the arterial tree comprises two main branches, namely the Left Coronary Artery (LCA) and the Right Coronary Artery (RCA), which originate at the root of the aorta, near the top of the heart. In the LCA branch, the initial segment between the aorta and the first bifurcation is called the Left Main (LM) coronary. The LM coronary typically branches into the Left Anterior Descending (LAD) and the Left Circumflex (LCX) arteries. On the other hand, the RCA normally originates at the right coronary cusp and travels to the posterior interventricular branch. In 85% of the cases, the RCA is the dominant vessel and supplies blood to the posterior descending branch, which travels in the Posterior

Interventricular Vein (PIV) groove. However, the exact anatomy of the coronary arteries could exhibit a wide range of geometries, depending on the individual [2].
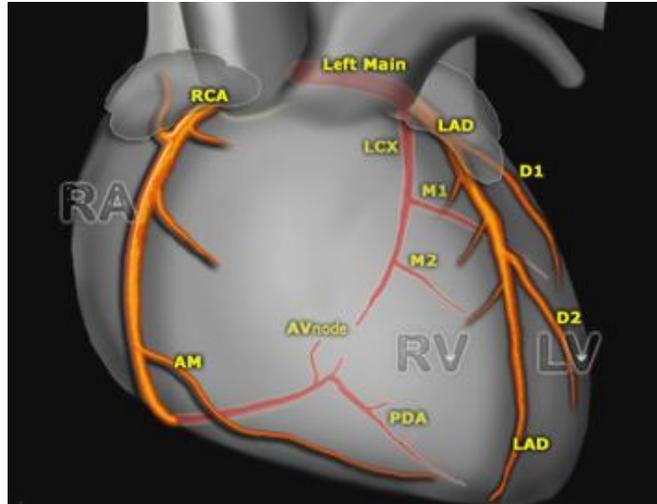
Figure 1.1: Illustration of the major coronary arteries of the heart, including the right coronary (RCA), the left anterior descending (LAD) and the left circumflex (LCX) arteries [2].

1.2 Coronary Artery Disease

Coronary Artery Disease (CAD) occurs when the coronaries are occluded and become constricted, which leads to the heart becoming starved for oxygen and other nutrients and eventually stop beating. According to the most recent statistics by the World Health Organization (WHO), CAD is one of the most prevalent causes of death in the world and affects an increasing number of people. Approximately 17 million people were killed due to one or more types of CAD year worldwide in 2011 [3]. Atherosclerosis is a condition in which plaques, typically made up of fat, cholesterol, calcium and other substances found in the blood, become clogged up in the medium and large arteries of the heart. If this is left untreated, it will harden and narrow the arteries over a period of time. As a consequence, the flow of oxygen-rich blood to organs and other parts of body will be reduced, which may cause serious problems, including myocardial infarction, or even death. Fig. 1.2 illustrates a comparison before and after plaque builds up within a blood vessel. The abnormal blood flow can be identified at the site where the plaques are present in the arterial wall.

Normal artery

Artery wall

Normal blood flow

Artery cross section

Narrowing of artery

Abnormal blood flow

Plaque

Narrowed Artery

Plaque

(a)   (b)
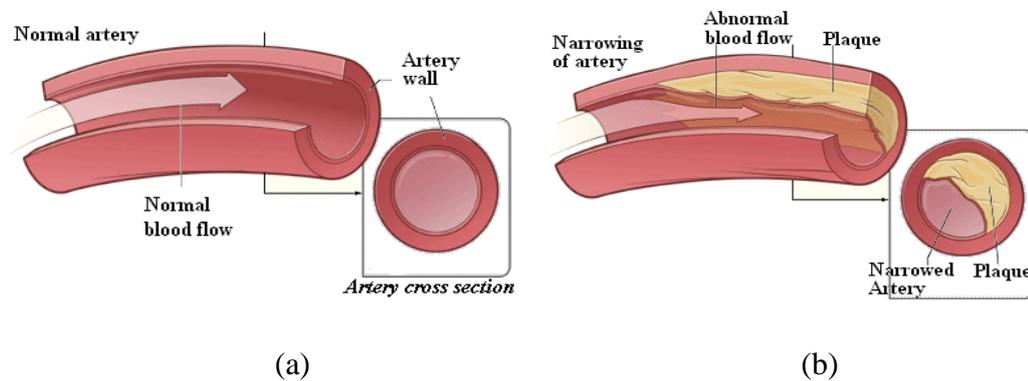
Fig 1.2: Illustration of blood flow in (a) A normal artery, (b) A narrowing artery with plaque buildup [4].

1.3 Diagnostic Imaging of Coronary Artery Disease

From the clinician's point of view, it is important to image the entire coronary arterial tree in order to assess the prognosis of coronary abnormalities, such as evaluate the severity of stenosis (narrowing arteries), and facilitate subsequent treatment. In the following subsections, we will go through the routine clinical procedures for imaging of coronary arteries and illustrate example images produced by these imaging modalities.

1.3.1 Coronary Artery Angiography

Coronary artery angiography is an X-ray examination of the vessels and chambers of the heart, which is often done to identify any narrowed or clogged coronary arteries that may prevent blood from reaching the heart muscle. The study can be also used to measure the size and the function of the chambers of the heart and the function of heart valves. During the procedure, the patient is firstly placed on a table equipped with a fluoroscope and an X-ray imaging device, as illustrated in Fig. 1.3(a). Then, the fluoroscope moves around the patient's chest in all directions to record pictures of the heart and the coronary arteries from multiple angles.
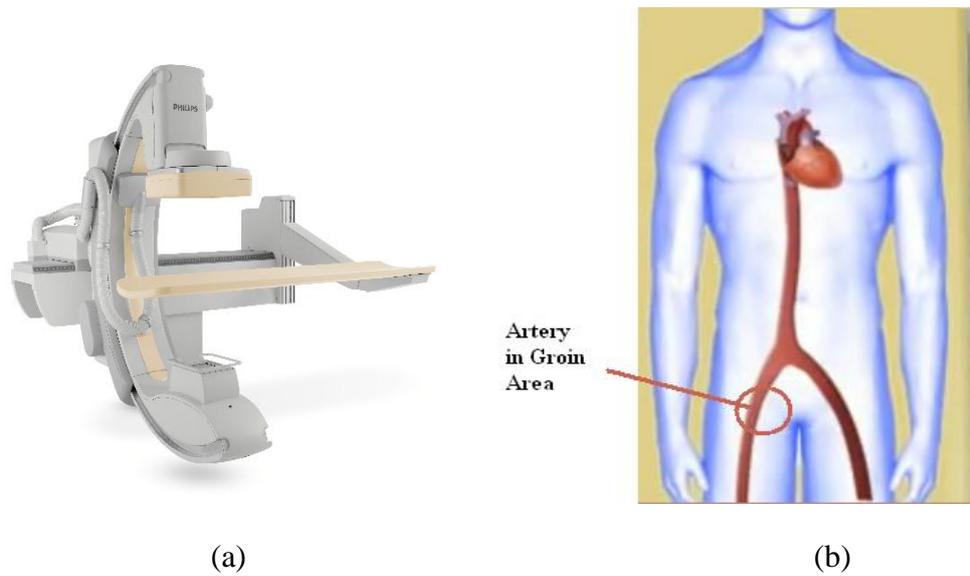
Figure 1.3: Imaging the coronary arteries through the conventional cardiac catheterisation examination. (a) An illustration of a modern cardiovascular X-ray system designed for interventional radiology, (b) Illustration of the commonly used entry site, i.e., the artery in the groin area, for cardiac catheterisation [5].
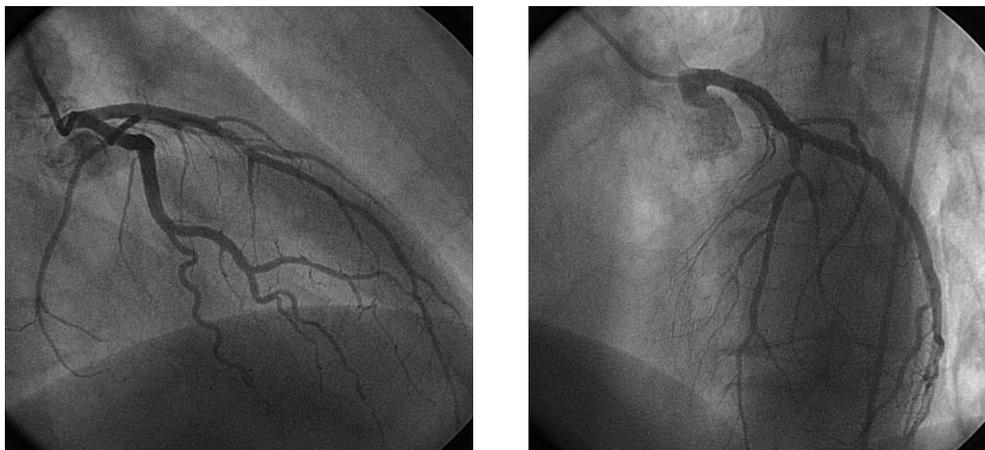
Figure 1.4: Examples of conventional coronary angiography images.

Most cardiac catheterisation procedures take place in the arteries of the groin area and the arteries of the arms. When the doctor decides the entry site, an introducer, which is a thin plastic tube, is inserted into the artery. Once this introducer is placed, a wire passes through the introducer and is gently guided through the arterial system to the heart. Next, the catheter, a small flexible tube, is inserted over the wire and carefully advanced through the aorta and the coronary arteries, where the catheter

movement is viewed through the X-ray screens. As soon as the catheter reaches the coronary arteries, a special dye is injected, which allows the fluoroscope to take X-ray images, so called angiograms, of the arteries. Any blockages can then be clearly identified as the arteries are filled with dye (see Fig. 1.4).

Figure 1.5: A modern multiple slice Computed Tomography machine. The patient is placed on the table, moving through the ring unit, which is comprised of the X-ray source and the detector [5].

1.3.2 Computed Tomography Angiography

Although cardiac catheterisation is capable of providing high resolution coronary images and is still treated as the gold standard for the assessment of stenotic coronaries, some complications and limitations have been identified. Firstly, as it is an invasive imaging modality, it carries moderate risks of morbidity and mortality [6]. In very rare occasions, it could damage the blood vessels as the catheter is threaded to the heart. The risk of complications is higher in people who have diabetes and kidney disease. In addition, conventional cardiac catheterisation is only able of producing 2D images of the arterial lumen and cannot image atherosclerotic plaques, which contain clinically meaningful information about the associated risk of developing coronary heart disease [7].

Computed Tomography (CT) is a non-invasive medical imaging modality, which provides an alternative way for imaging the coronary arteries. Since its first commercial deployment in 1972, CT has been intensively used in radiology departments to image the human body. Recent advances in vascular imaging technology using multiple-slice CT allow for providing volumetric datasets with high spatial and temporal resolution of the body. State-of-the-art CT scanners, with up to 320-row detectors, are capable of imaging the coronary arteries within a single heart beat, producing a 3D image dataset with less than half a millimetre spatial resolution in all three directions [8, 9]. This has given rise to CT becoming a reliable routine examination for the assessment of cardiovascular disease in clinical practice. As illustrated in Fig. 1.5, a modern CT scanner, in general, consists of a tunnel-like structure with an X-ray tube on one side and the detector on the other side. Before scanning, the patient is placed on the table, and the medical technician places an intravenous (IV) line to the patient's arm, which will provide the actual contrast to view the arteries by injecting the contrast material. To synchronise image acquisition and reconstruction with the heart motion, the electrocardiogram (ECG) signal is usually monitored. By continuously monitoring the ECG signal, cross sectional images of the heart are imaged and reconstructed at the same cardiac cycle, which compensates for the motion of the beating heart (see Fig. 1.6). During the examination, the IV contrast agent is automatically injected and the patient is advised to hold their breath for 3-5 seconds. The CT scanner records the X-ray attenuation through a plane with a finite thickness cross section of the patient, and these attenuation measurements are then reconstructed using a dedicated computerised system to produce a 3D volumetric image dataset of the body. These images permit the cardiologist to determine whether plaque or blockages are present in the arterial walls.
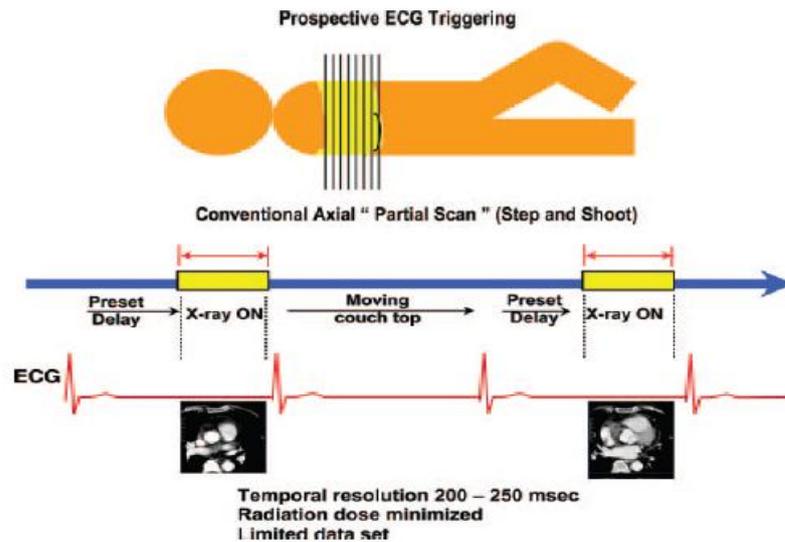
Figure 1.6: Illustration of the ECG-triggered cardiac CT scanning mode. During the procedure, the X-rays are turned on at predetermined *R*-wave to *R*-wave (R-R) intervals to acquire sufficient data of the coronary arteries for image reconstruction [10].

Fig. 1.7(a) shows an example of a transaxial coronary CT image. It is also possible to visualise the CT volume data in such a way as to follow the course of the artery, which displays the lumen and surrounding tissues of the vessel in a single image. Such a technique is referred to as curved planar reconstruction (CPR) [11, 12], and is a useful tool to view a CT image sequence from a perspective angle rather than the transaxial acquisition plane (see Fig. 1.7(b)). This technique will be discussed in more detail in Section 2.3.

(a)   (b)
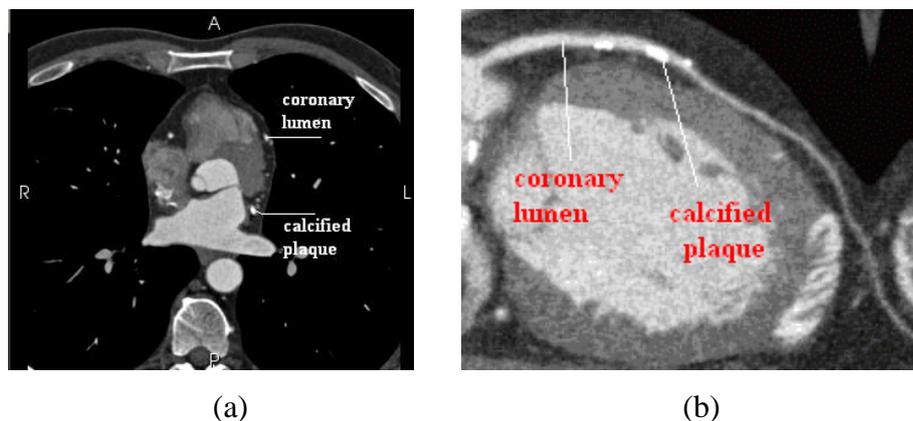
Figure 1.7: Examples of different post-processing techniques for visualisation of the coronary artery. (a) An axial image taken from a coronary CT volume image, and (b) Illustration of the curved planar reconstructed CT image of the coronary artery.

1.4 Outline of the Thesis

Following this introduction, the thesis proceeds by exploring the literature in vascular image analysis in Chapter 2. In Section 2.1, a review of vascular structures extraction algorithms is firstly provided, with particular emphasis in 3D contrast enhanced vessel imaging modalities, i.e., CT and MRA. Then, we present recent developments in coronary quantification methods for the assessment of the severity of stenosis in Section 2.2. Finally, commonly used post-processing techniques for visual examination of coronary arteries are briefly introduced in Section 2.3.

Chapter 3 presents an automated framework for extraction of the entire coronary arterial tree in 3D CTA images. The chapter commences with a description of the pre-processing stage of the proposed framework, which is followed by the presentation of the two-step algorithm for segmentation of coronary arteries, taking into considering the problem of kissing vessel artifacts (Section 3.4.4). In the following section, we present the experimental results obtained from using hold out methods to demonstrate the efficiency and the accuracy on various synthetic and clinical datasets.

Chapter 4 proposes a dedicated algorithm for performing 3D quantitative vascular shape analysis in CTA images. The method is primarily aimed at providing the true reference surface and centreline data in the bifurcation regions, which usually exhibit irregular geometry and have not been addressed by conventional vessel quantitative analysis algorithms. The proposed method is based on the registration of an elliptic cross sectional tube model to each constituent branch of the bifurcation. The registration process is governed by a generic active contour based energy functional, which is minimised, when the fitted tube is registered onto the desired constituent vessel branch of the bifurcation, which will be explained with great detail in Sections 4.2-4.4.

Chapter 5 concludes this thesis and provides a list of recommendations for possible future directions and improvements to the existing work.

Chapter 2

Literature Review of Coronary Image Processing

Thanks to the continuing development of vascular imaging techniques, modern angiography imaging equipment is now capable of providing reliable 3D images for the assessment of vascular disease in clinical practice. Given the size and complexity of the 3D images produced by modern imaging devices, manual interpretation and analysis of these images can quickly add up to several hours of processing. Hence, there is an urgent need to develop dedicated systems to assist in the analysis of angiography images and facilitate subsequent diagnostic procedures. In this chapter, we begin with a review of the state-of-the-art in vascular structures extraction techniques with particular interest in 3D contrast enhanced imaging modalities, such as MRA and CT, as vessel extraction is a crucial component in developing automatic radiological systems. Next, existing work in the quantitative analysis of coronary arteries, such as plaque characterisation and stenosis grading, is explored in Section 2.2. This is followed by a short introduction of commonly used post-processing techniques, including Curved Planar Reconstruction (CPR), Maximum Intensity Projection (MIP) and Volume Rendering (VR), for the examination of coronary lesions in Section 2.3. Finally, Section 2.4 concludes this chapter.

2.1 A Brief Review of Vascular Structures Extraction

During the past decade, intensive research effort has been dedicated in designing semi- or fully automated algorithms for delineation of vascular structures in medical images (i.e., detection of vessel boundaries and centreline extraction). However, there is still no general solution for all applications, as methods vary in terms of the image modalities, anatomical applications (e.g., cerebral, cardiac and retinal, etc) and many other application-specific factors. Rather than providing an exhaustive review of all of the existing work in the field of vessel segmentation and centreline

extraction, we focus our analysis in the research dedicated to 3D contrast enhanced image applications (i.e., MRA and CTA). In this section, we survey vessel extraction techniques, covering both early and current work, and structure them in three categories based on the extraction schemes, namely, minimum (shortest) path based methods, stochastic tracking based techniques (for instance, Bayesian filters) and active contour models based approaches. Certainly, given the great amount of research in this field, it is possible to categorise published work on a number of alternative criteria. Comprehensive reviews of 3D vessel extraction algorithms can be found in [13, 14].

2.1.1 Minimum Path Based Vessel Extraction

Minimum (shortest) path algorithms have been studied for a long time as a means of solving computer vision tasks. In the context of vascular structures extraction, minimum path based approaches are particularly popular for searching for the centreline of vessels between user supplied endpoints. This technique enables the determination of the global optimal of the associated minimal path energy, thus making the resulting path less sensitive to local spurious image features. Let $C(s)$ denote a curve starting at point p_0 and ending at p_1 (where s represents the parameterisation variable). The minimum path problem can be generally defined in the following form [15]:

$$A_{p_0 p_1} \to R$$

$$C \mapsto E(C) = \int_\Omega w \left\| \frac{\partial C}{\partial s}(s) \right\|^2 + P(C(s))ds = wL(C) + \int_\Omega P(C(s))ds = \int_\Omega \tilde{P}(C(s))ds \tag{2.1}$$

with

$$\tilde{P}(p) = w + P(p) \tag{2.2}$$

where $A_{p_0 p_1}$ represents the search space of all curves connecting the two endpoints constrained by the boundary conditions: $C(0)=p_0$, $C(L)=p_1$, and L denotes the length of the path between the two ends. The potential P is derived from the image data, Ω, and varies according to the specific tasks. w is a constant controlling the smoothness

of the extracted path. In terms of the numerical schemes employed to solve the minimum path problem, existing algorithms can be categorised into two notable classes, namely, discrete Dijkstra graph based methods [16-19] and Fast marching based algorithms [20, 21].

In Dijkstra's approach, an image is mapped to a graph, where each voxel is a vertex, and is connected to neighbouring voxels through edges. The weights on the vertices are defined by the potential (i.e., the associated minimum path energy), derived from the image. Distance transform (mapping) is one of the simplest and the most commonly used potentials in the Dijkstra shortest path problem. In these methods, a distance field is firstly constructed by calculating the distance from the user defined source point to each pixel/voxel inside the object of interest. Then, the shortest path between an arbitrary pixel/voxel to the source point is obtained by backtracing from such pixel/voxel to the source, along the gradient direction of the distance field. In order to reduce the computational cost of the distance transform, a variety of distance approximations have been proposed, such as the Manhattan metric [22], the Chamfer distance [23] and the Euclidean distance [24].

Despite these methods enjoying the advantage of computational efficiency, the shortest path, extracted based on distance transform methods, often deviates from the position of the central axis of the vascular structures and tends to follow the boundaries at high curvature positions, as shown in Fig 2.1(b). This is due to the fact that all voxels (i.e., both the boundary and the central voxels of the object) are treated equally, whereas the 'hugging corner' effect simply leads to a shorter path. To address this problem, Samara *et al*., [22] proposed the determination of the centreline by averaging two shortest paths obtained by starting from each of the endpoints. However, this simple averaging procedure cannot guarantee resolving the 'centricity problem' at sharp turn locations.

(a)   (b)
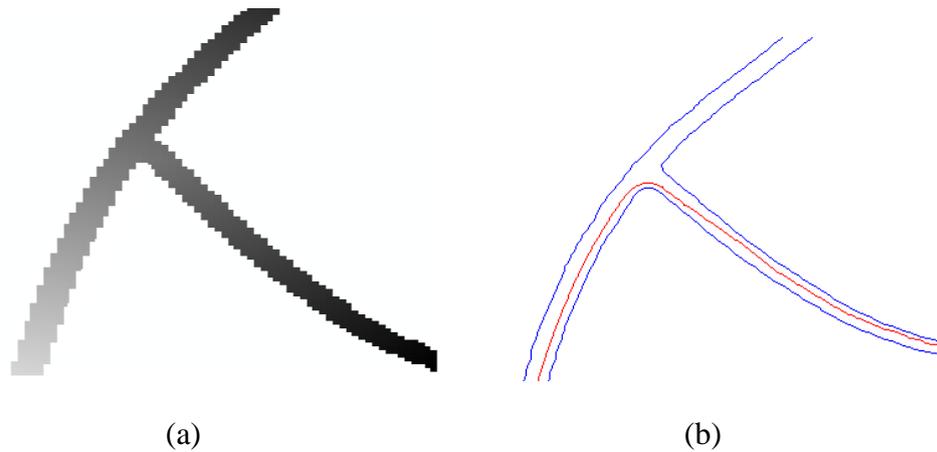
Figure 2.1: Illustration of the 'hugging corner' effect [22] in a synthetic image. (a) The distance map, (b) The centreline (shown in red) is extracted through the application of Dijkstra searching algorithm based on the distance field in (a). The centreline is attracted to the boundaries of the object (in blue) at sharp turn positions.

Wan *et al.*, [25, 26] proposed a potential function based on the distance from the boundary (DFB) field, where the Euclidean distance for each voxel inside the object to its nearest boundary point is calculated. In their approach, each vertex x of the Dijkstra's graph is weighted in terms of its distance to the nearest boundary $(1/DFB(x))$, and thus, the centricity of the centreline is improved at high curvature positions by assigning high weights to vertices near the boundaries. Closely related to the DFB based methods, Bitter *et al.*, [27-29] proposed the suppression of the 'hugging corner' effect by finding the minimum cost path in a penalised distance field (PDEF). The PDEF field is constructed from the Dijkstra graph, as illustrated in Fig. 2.2, but with additional edges and vertices associated with the penalty term. The additional vertices and edges penalise the path from coming close to the boundaries of the objects, thus improving the accuracy and robustness of the resulting path in high curvature positions. Calculating the distance from the boundaries, however, involves additional computational costs causing lower efficiency of these methods. By realising the fact that boundaries voxels contribute less in determining the centreline in Dijkstra shortest path based approaches, the dimension of the Dijkstra problem can be therefore reduced if we only conduct our analysis in the voxels near the centreline to be extracted. To this end, Jiang *et al.*, [30] proposed cutting off boundary voxels to reduce the number of voxels that need

to be processed. In [27-29], the voxels around the centreline are detected through the analysis of the neighbour pattern of the gradient flow vector of the DFB field.

(a)   (b)
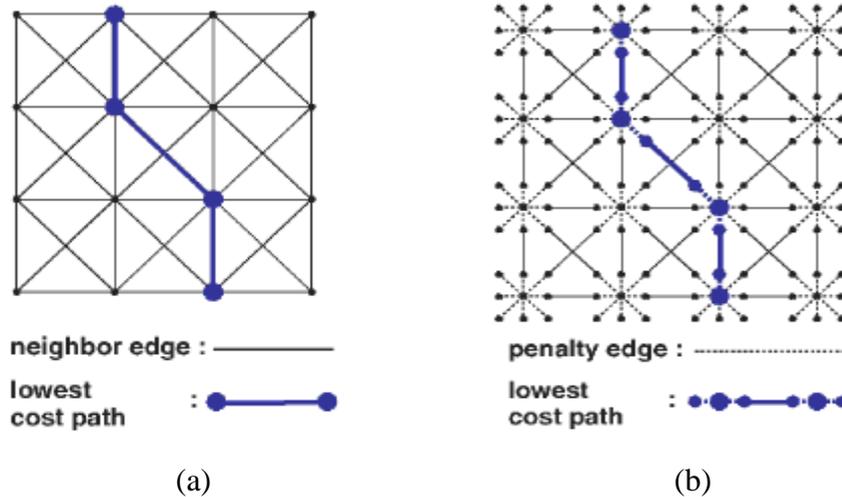
Figure 2.2: Illustration of the mapping from the image voxel grid onto an undirected graph in 2D view. (a) Distance field defined on a graph based on a simple mapping from the image grid, (b) Penalised distance field for the same region as in (a). Solid lines depict the weights, which depend on the distance between the vertices. Dashed lines denote the penalty edges associated to the voxel [28].

Previously discussed distance transform based methods generally require a binary representation of the vascular structures prior to performing the shortest path based centreline extraction, which involves unnecessary costs when the objective is only to extract the centreline. Furthermore, as these methods solely work on the segmented binary image, the detected path may depend heavily on the initial segmentation. To eliminate the need for the pre-segmentation, recent research has emerged into the detection of the shortest path directly from image features. Vessel enhancement filters [31-33], based on the eigenvalue analysis of the Hessian matrix, are a popular technique in searching for tubular geometries in medical images. Under the assumption that vessels are cylindrical structures with Gaussian distributed profiles along their normal direction, the eigenvalues of the Hessian matrix are used as the shape descriptor to detect the presence of the vascular structures. In general, these filters respond at the location of each pixel/voxel by returning the likelihood of such pixel/voxel belonging to a vascular structure. The filter response reaches its maximum at the centre of the vessel, when the scale of the

filter matches the size of the vessel. Early work based on the response of vessel enhancement filters as the shortest path potential was reported by Wink *et al.*, [34], where the authors proposed the combination of the filter response in [31] with the minimum cost path technique for defining the centreline of coronary arteries in MRA images. They further developed their work in [35] in order to deal with vessels of varying widths and crossing vessels. In the extended work, rather than searching for the minimum path based on the maximum response of the filter, they propose the calculation of the minimum path energy based on a vector-valued multiscale feature image, where tubular structures are enhanced. By using the scale of the filter as an additional dimension, the performance of the method is improved with respect to the crossing vessel artifacts and the variation in vessel diameters.

Hessian matrix based vessel enhancement filters are based on a single branch vessel model, and may result in false positive responses in the presence of aneurysms, stenoses and bifurcations, where the intensity distribution deviates from the assumption of the underlying model. Under the assumption that the shape of vessels can be approximated as a circular/elliptic disk surrounded by darker rings in the cross sectional view of CT images, Kaftan *et al.*, [36] proposed the use of the 'medialness' measurement, obtained by analysing the local intensity profiles for each pixel/voxel of the image, as the shortest path energy. Compared with Hessian based vesselness metric, the proposed potential energy is more robust to local intensity variations, such as the presence of neighbouring bright structures (see Fig. 2.3). Gulsun and Tek [37] extended this concept for general vascular structures modelling. Instead of computing the 'medialness' map at each vertex of the graph (i.e., each voxel of the image), they propose only calculating the 'medialness' metric for these vertices perpendicular to the orientation of the current path during the searching process, which increases the accuracy and the efficiency of the their algorithm.

(a)   (b)   (c)
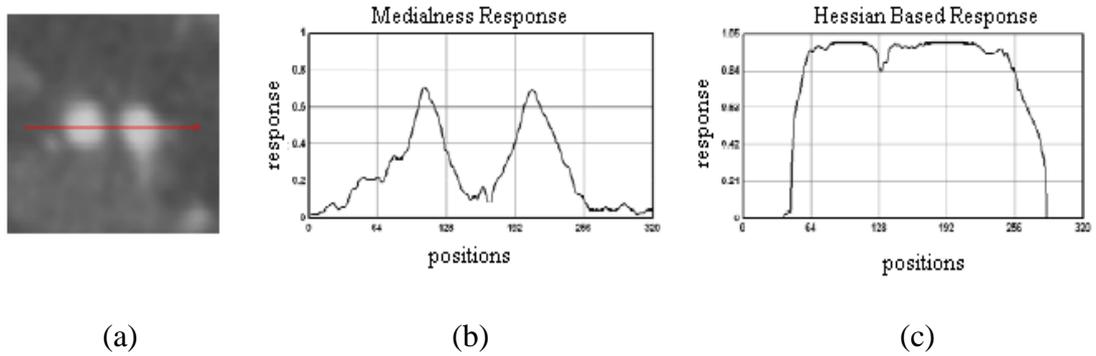
Figure 2.3: Illustration of the filter responses along a ray on an axial CT image. (a) An axial CT image, (b) The medialness filter response obtained using the algorithm reported by Kaftan *et al.*, (c) The Hessian based filter response [37].

The previously discussed methods, merely relying on intensity features derived from the image, may produce erroneous paths in the presence of image artifacts and branching structures, where irregular intensity appearances are usually encountered. To address this problem, the authors in [38] proposed the incorporation of local orientation information into the shortest path energy functional. In their method, as illustrated in Fig. 2.4, the geometry of a vessel segment is modelled as a 1D profile with different orientations and varying widths, which serve as templates for approximating orthogonal vessel portions. The potential of the associated minimum path problem is then defined as the normalised cross correlation between the image and the models. Cetingul *et al.*, [39] proposed a two-step centreline extraction algorithm to deal with vessel bifurcations and nearby spurious branches. In the first stage of the proposed method, the initial centreline is extracted based on the response of the vessel medialness filter [37]. The centrelines are refined in the latter step through the application of a multiscale orientation descriptor, which estimates the local direction of the vessel in the vicinity of bifurcations and crossing vessels.

15
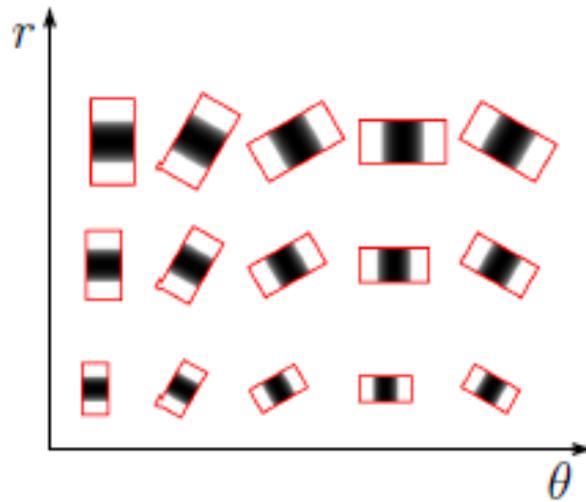
Figure 2.4: Illustration of the local vessel model for different orientations and scales [38].
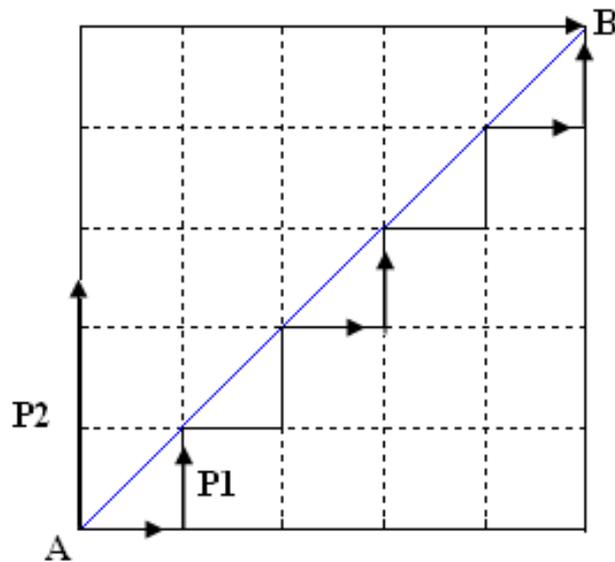
Figure 2.5: Illustration of the metrication errors caused by the Dijkstra graph based minimum path method. The optimal path between points A and B determined by using graph search based methods (either P1 or P2) suffers from metrication errors. The blue line shows the actual minimum path between A and B.

The aforementioned shortest path approaches, solved based on the Dijkstra graph algorithm, generally enjoy the advantage of the high computational efficiency. However, they are not consistent with continuous front propagation rules, when implemented in a discrete rectangular grid, which can result in numerical errors (known as the metrication error [40]) due to the discrete graphical representation of

16

the search space. As depicted in Fig. 2.5, the optimal (shortest) path between points A and B is shown in blue, however, due to the discrete graph representation, the detected optimal path(s) by means of Dijkstra methods can be either P1 or P2, irrespective of the resolution of the grid.

In order to eliminate such metrication errors, numerical solutions consistent with the continuous front propagation rules have been developed [41-43]. Fast marching based algorithms, pioneered by Cohen and Kimmel [15] and further developed by Sethian and his colleagues [20, 21, 44], have received a great deal of attention since their first introduction in solving the minimal path problem in 1990s, due to their low computational costs and consistency with the continuous formulation of the associated minimal path energy. Broadly speaking, fast marching methods share many common features with Dijkstra's approaches, but they approximate the Euclidean ($L2$) cumulative cost, and thus, are capable of producing optimal paths with sub-voxel accuracy. As defined in Eq. (2.3), in fast marching methods, a surface U_0, known as minimal action surface, is firstly constructed to define the arrival time of a front propagating from the manually selected start points to each pixel of the image. The values at each point, p, on this surface correspond to the minimal energy integrated along a path that originates from the user supplied source point p_0 and ends at p:

$$U_0(p) = \inf_{C(L)=p}\left\{\int_C P(C(s))ds\right\} = \inf_{A_{p_0,p}} E(C(s)) \tag{2.3}$$

where P denotes the potential derived from the image data, s is the arc-length parameter and $C(s)$ denotes the path(s) starting at p_0 and ending at p. L represents the length of the path. The surface can be determined by solving the Eikonal equation $|\nabla U| = P$, and then the geodesic (shortest) path connecting point p_0 to p is found by back propagation on U_0 along the gradient descent direction.

Early work of using fast marching methods to solve the vessel extraction problem was reported by Deschamps and Cohen [40, 45], where the potential for the minimum path problem is defined as the similarity between the source voxel and the detected voxel in the image, measured in terms of intensity differences. This

method works well for objects with homogenous intensity distributions and good contrast to the background. However, uneven intensity distribution along the vessels is commonly encountered in angiography images, due to the concentration changes of the contrast agent and the acquisition noise. Distance transform (DT) based methods have also found applications in defining the centreline of vascular structures using fast marching algorithms. In contrast to DT based methods applied on graphs, techniques based on fast marching algorithms are capable of producing continuous and accurate (with sub-voxel precision) centrelines. Cardenes *et al.*, [46] proposed the use of fast marching methods to refine the initial centreline determined by the distance transform, which may contain disconnected and collapsed centreline points due to discretisation effects. Uitert and Bitter [47] proposed the computation of the distance transform from object boundaries using level sets, with sub-voxel accuracy, and then the extraction of the centrelines based on the distance field by fast marching algorithms.

As previously discussed, second-order derivative information (i.e., Hessian matrix) is a popular local descriptor for detection of vascular structures. However, they are sensitive to image noise and local intensity variations. Hence, using such filters for the estimation of the potential function, as in the case of the minimum path problem, may result in erroneous detection of centrelines. To increase the robustness of the detected centreline in the presence of local spurious features, Young *et al.*, [48] proposed the use of the registration error between the local image and an adaptive cylinder model, defined by its orientation and radius, as an additional criterion to Frangi *et al.*, vesselness metric to form the potential function. Similar work is also found in [49], where the generic cylinder model, constrained by an active contour like energy functional [50, 51], is registered to each segment of the vessel to refine the resulting centreline. When combined with cylindrical shape models, the robustness of vessel enhancement filter based methods is significantly improved with respect to local intensity variations and the presence of image artifacts and noise. However, forming such models and registering them to local vascular structures requires significant computational power, which hinders their real-time clinical application.

(a)   (b)
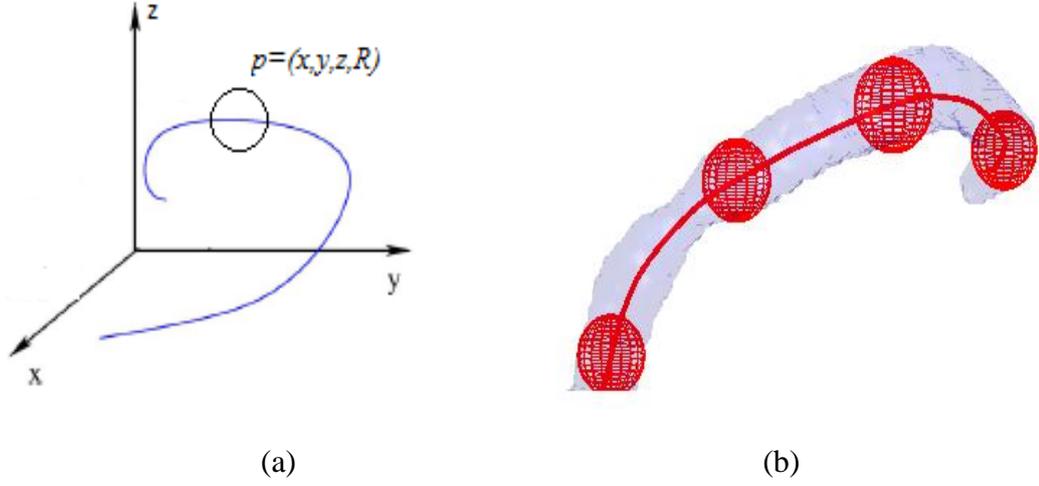
Figure 2.6: Illustration of modelling a 3D vessel surface as a 4D curve. (a) The 4D curve is represented by successive 3D point coordinates and the associated radii of the best fit spheres, (b) An example of using the 4D curve to represent the vessel surface.

As the synthetic images shown in Fig. 2.6, vessels can also be approximated by a succession of circles/spheres with varying centres and radii. Based on this concept, Li and Yezzi [52, 53] proposed modelling vascular structures as 4D curves to simultaneous extract both vessel centreline and boundaries, using the minimum path method in 4D space. In their work, Li and Yezzi proposed the formulation of shortest path energy based a spherical neighbourhood as follows:

$$\tilde{P}(sp) = w + \lambda_1(\mu(sp)/r - \mu(sp_0)/r)^2 + \lambda_2(\sigma(sp)/r - \sigma(sp_0)/r)^2 \qquad (2.4)$$

where $sp = (p, r)$ represents the circle/sphere located at point p with radius r, and $\mu(\cdot)$ and $\sigma(\cdot)$ denote the mean and variance derived from the region inside the circle/sphere defined by sp, respectively. sp_0 is the initial circle/sphere defined by the user. w is a constant controlling the smoothness of the centreline. λ_1 and λ_2 are the weights for the similarity metrics. The minimum of the potential function occurs when the current sphere (sp) is inside the vessel (exhibiting similar intensity statistics as the starting sphere) and is tangential to the vessel boundaries (the radius of the current sphere at that point is maximised). To deal with varying intensity patterns along the vasculature, they further proposed calculating the minimum path energy based on intensity statistics at the surfaces (boundaries) of the sphere:

19

$$\tilde{P}(sp) = w + \frac{\lambda_1}{1+\delta_\mu^2(sp)} + \frac{\lambda_2}{1+\delta_\sigma^2(sp)} \qquad (2.5)$$

where $\delta_\mu(\cdot)$ and $\delta_\sigma(\cdot)$ represent the mean and variance differences at the surfaces between spheres $sp=(p, r)$ and $sp'=(p, r-1)$. Despite this method being able to simultaneously extract the centreline and detect the vessel boundaries, there were also some limitations. Firstly, the potential function designed for extraction of vessels with constant intensity distribution is sensitive to initialisation (in terms of both the position and the radius of the initial circle/sphere). Secondly, the potential, dedicated for segmenting the vessel with spatial varying intensities, uses the intensity statistics at the surface of the sphere. Due to image discretisation, however, the surface of the sphere may contain a small number of voxels, thus making this metric less robust to image noise and artifacts. Furthermore, the selection of an appropriate step size in r poses additional difficulties, and as a matter of fact, it is a compromise between accuracy and efficiency. On one hand, a small step size for r leads to a fine resolution in the fourth dimension, however it also increases the computational cost of the method: the computational complexity of the fast marching is $O(N \log N)$, where N is the number of grid points in the search space [20]. On the other hand, a large step size in radius allows for r taking a limited number of values, which may compromise the accuracy of the algorithm. Moreover, Li and Yezzi's method is based on an isotropic metric, which does not take into account vessel orientation information.

Along the same research line, Antiga *et al.*, [54] proposed the extraction of centrelines by finding the locus of centres of maximal spheres inscribed into the tubular structures based on the Voronoi diagram using the surface points of the object. The proposed method works directly on the continuous surface domain, thus improving the accuracy of the estimated centrelines, when compared to Li and Yezzi's approach. Benmansour *et al.*, [55, 56] proposed using an anisotropic potential for the minimal path problem, where the local metrics (potentials) allow for a higher speed along the orientation of the vessels. In particular, the optimally oriented flux (OOF) based vesselness descriptor [57], which accounts for the magnitude of image gradient flows along a specific direction at the outer surface of

a closed region, is calculated at each voxel of the image to locally measure the vesselness. The oriented flux along the direction v is defined as:

$$f(\boldsymbol{x}, \boldsymbol{v}; r) = \int_{\partial S_r} ((\nabla G * I)(\boldsymbol{x} + \boldsymbol{h}) \cdot \boldsymbol{v}) \boldsymbol{v} \cdot \boldsymbol{n} \, da \tag{2.6}$$

where S_r denotes the local sphere and r represents the radius of the local sphere. ∇G is a gradient of a Gaussian function, G. $\boldsymbol{n}$ represents the outward unit vector of the sphere, and $\boldsymbol{h}=r\boldsymbol{n}$. da denotes a small segment (area) of the outer surface of sphere S_r. $\boldsymbol{v}$ is a vector indicating the projection direction. The symbol, *, denotes the convolution. In their methods, the local metric is designed based on both the eigenvalues and eigenvectors information of the OOF, which enables the proposed method to detect local vessel directions and enforce the front propagating along that direction. In contrast to Hessian matrix based vessel enhancement filters which measure the vesselness of each voxel based on a local region centred at that voxel, the OOF responds for vascular structures relying on the outer surface of the local sphere, and thus, the robustness of the filter is greatly improved with respect to the presence of adjacent vessel-like structures. Since these methods are based on an anisotropic metric, conventional fast marching methods are not suitable for solving such problems [58]. The authors proposed the use of an iterative method in [59] to determine the minimal action surface, however, as discussed in their research [56], the iterative scheme is computationally expensive and requires parallel implementation to speed up the whole process.

In fast marching methods, the front will expand to every voxel in the image as time goes by, which will increase the number of voxels which need to be processed and the probability of extracting undesirable paths. Freezing processes [45, 60], which terminate front evolution at some 'wall voxels' by setting their speed to zero, have been introduced to extract the central path for elongated objects. Mueller and Maeder [61] proposed freezing the evolution of the front when it is out of the vascular regions, i.e., when the vesselness metric is below a threshold. As pointed out by Deschamps [62], the minimum path extracted through the backtracing method with a fixed step size in the gradient descent direction may result in oscillations. To prevent such oscillations, they proposed the use of an adaptive step

size in the backtracing calculation, which is determined in terms of the rate of change of the potential (speed) function.

2.1.2 Stochastic Filters Based Vessel Extraction

Rather than detecting the vascular structures deterministically, the vessel extraction problem can also be solved statistically through the use of Bayesian tracking approaches [63], where the probability density function is computed at each voxel to measure the likelihood of such voxel belonging to vessels. Compared with deterministic methods, these algorithms are not only capable of producing the optimal solution (in a statistical sense) of the vessel extraction problem, but also to provide the statistical properties of the solution (e.g., the variance of the resulting solution). In this section, we consider the vessel as a succession of thin segments, which are characterised by a set of parameters (known as the state-vector) containing all of the necessary information to reconstruct each segment of the vessel, connected in series. If we seek to obtain a complete segmentation of the vessel, then the state vectors are required to be determined optimally at each segment. To this end, we assume these parameters as unknown states of a sequential of stochastic/dynamic process, which can be determined successively through the use of Bayesian tracking algorithms. Mathematically, the Bayesian tracking problem can be modelled using a stochastic process, which is characterised by two equations, namely, the dynamic/system equation (model),

$$\boldsymbol{x}_k = f_k(\boldsymbol{x}_{k-1}, \boldsymbol{u}_{k-1}, \boldsymbol{v}_{k-1})$$

(2.7)

and the measurement/observation equation (model)

$$\boldsymbol{z}_k = h_k(\boldsymbol{x}_k, \boldsymbol{u}_k, \boldsymbol{n}_k)$$

(2.8)

where $f_k(\cdot)$ and $h_k(\cdot)$ are known functions associated with the system and measurement model at the time sequence k, given previous state, input $\boldsymbol{u}_{k-1}$ and the state noise $\boldsymbol{v}_{k-1}$, respectively. $\boldsymbol{x}_k$ and $\boldsymbol{x}_{k-1}$ are the current and previous states. $\boldsymbol{z}_k$ is the measurement based on the current state, the system input and the measurement noise $\boldsymbol{n}_k$. The system model describes how the state of the system changes with

22

time. The measurement equation, on the other hand, models the noisy outputs of the process based on the current state.

   The aim of Bayesian tracking approaches is to estimate the posterior probability density function (PDF) of the state, when a measurement is received. Recursive filters, which sequentially update the previous estimations, are particularly suitable for solving the incremental tracking problem in this case. Such filters, in general, alternate between predictions of the prior PDF of the state and updating the posterior PDF once the current measurement becomes available. In the prediction step, let us assume the prior PDF $p(x_{k-1}|z_{1:k-1})$ is known, according to the Chapman-Kolmogorov equation, the prior PDF of the state at time k can be expanded as:

$$p(x_k \mid z_{1:k-1}) = \int p(x_k \mid x_{k-1}) p(x_{k-1} \mid z_{1:k-1}) dx_{k-1} \qquad (2.9)$$

where the probability of $p(x_k|x_{k-1})$ is defined by the dynamic model defined in Eq. (2.7). For the update stage, when the measurement z_k is available at time sequence k, the posterior PDF of the state is calculated based on Bayes rule:

$$p(x_k \mid z_{1:k}) = \frac{p(z_k \mid x_k) p(x_k \mid z_{1:k-1})}{p(z_k \mid z_{k-1})} = \frac{p(z_k \mid x_k) p(x_k \mid z_{1:k-1})}{\int p(z_k \mid x_k) p(x_k \mid z_{k-1}) dx_k} \qquad (2.10)$$

$p(z_k|x_k)$ is obtained using the measurement model in Eq. (2.8). By recursively implementing the prediction and update stages, the state vector of the process can be determined successively. However, there are no analytical solutions for these probabilities, since the integrals are not tractable. Kalman filters [64-66], based on the assumption that both the prior and posterior PDF of the state are following the Gaussian distribution, are capable of providing an optimal approximation of this Bayesian tracking problem by using simple linear equations. Unfortunately, given the complexity of the vessel geometry (e.g., vessel bifurcations) and appearance (such as the presence of coronary pathologies), the linear and Gaussian distributed state assumption does not hold in the vessel tracking problem in medical images. Particle filters [67-70], a sequel of Monte Carlo techniques, provide a sub-optimal solution to the Bayesian tracking problem, and are particular popular in solving non-linear and multimodal Bayesian state estimation problems. The key idea of the

particle filter is that any given PDF can be approximated by a set of random samples/particles, whose distribution is known a priori. Hence, given all of the measurements z_k, the PDF of the current state can be represented as:

$$p(\boldsymbol{x}_k \mid \boldsymbol{z}_k) = \sum_{i=1}^{Ns} w_k^i \delta(\boldsymbol{x} - \boldsymbol{x}^i) \qquad (2.11)$$

where N_s denotes the number of random samples/particles used to approximate the posterior PDF $p(\boldsymbol{x}_k|\boldsymbol{z}_k)$; when N_s is chosen to significantly large, the approximation defined in Eq. (2.11) converges to the true PDF. $\boldsymbol{x}^i$ represents random samples whose distribution is conditioned by the importance density function $q(\cdot)$, which is defined by the user and can be any distribution. w^i is the weights associated with each particle. According to the principle of sequential importance sampling (SIS) [71], which is the basic framework for most particle filter algorithms, the weight for each sample (particle) is updated as:

$$w_k^i \propto w_{k-1}^i \frac{p(\boldsymbol{z}_k \mid \boldsymbol{x}_k^i) p(\boldsymbol{x}_k^i \mid \boldsymbol{x}_{k-1}^i)}{q(\boldsymbol{x}_k^i \mid \boldsymbol{x}_{k-1}^i, z_k)} \qquad (2.12)$$

In practice, in order to prevent the weights becoming skewed as time goes by, a resampling process is usually applied after a certain number of steps.

The first application of particle filters in vessel extraction was reported by Florin and his co-workers [72], who modelled vessels by a succession of elliptical cross sections. The shape, in terms of the set of parameters defining the ellipse and the local vessel orientation, and the appearance related parameters (i.e., the intensity features of the cross section), are used as the state variables of the stochastic process to characterise the vessel. The shape parameters provide information regarding the position of the ellipse in the image and define the region of interest (i.e., the area within the interior of the ellipse). Appearance related components, on the other hand, are used to model the statistical properties of the region of interest. In order to accommodate the irregular intensity distribution of the vessel caused by pathologies such as calcifications, they propose the approximation of the statistical properties of vessel cross sections using a Gaussian mixture model (GMM), which comprises two components related to the blood and calcified voxels, respectively. The sample

importance distribution $q(\cdot)$, in their method, is chosen as the prior probability of the states, and hence according to Eq. (2.12), the weight for each particle only depends on the measurement model. The symmetric Kullback-Leibler distance [72], measuring the difference between the predicted intensity distribution and the actual measurement derived from the interior of the ellipse, together with a 'ribbon' metric, which provides a measurement of the image contrast to identify bright vessels on dark background, are employed in the update stage to quantify the goodness of the estimation. The metrics reach their extremes when the estimated ellipse is aligned with the boundaries of the vessel of interest. In the extension of their work [73], they proposed the detection of vessel boundaries using the circular shortest path algorithm [74], and the application of the boundary information as an additional metric to evaluate the quality of the prediction. These seminal works, pioneered by Florin and his colleagues, have demonstrated the efficiency and flexibility of particle filter based methods to incorporate multiple hypotheses for solving the tracking problem. Compared with classical deterministic methods, which rely on single assumption for the local features, the robustness of the particle filter based methods with respect to image noise and local image feature variations is significantly improved.

Along the same research direction, Shim *et al*., [75, 76] propose the use of boundary points, taken from a plane perpendicular to the vessel axis, as the observations in the calculation of the posterior PDF of the state in the update stage. In contrast to Florin's methods in [72, 73], which measure the differences between the prediction and the observation based on the appearance information alone, this technique takes both the orientation and appearance properties into account in the update stage. Specifically, vessel boundary points are firstly detected by examining the gradient intensity profiles, collected from a number of rays originating from the centre of the cross section and pointing outwards. Possible outliers, such as sharp gradient changes caused by calcium, bones and nearby veins, are removed by analysing their intensity profile patterns. Next, the orthogonal cross section is determined by finding the minimum cross sectional area defined by the detected border points. The border points located within this perpendicular cross section are

then used in the subsequent stage for calculation of the disparity metric, which is measured by the exponential sum of distances between these boundary points and the estimated ellipse. In a departure to Florin's appearance model, which is based on local regional information, the proposed method defines the observation relying on the boundaries of the vessel cross sections, and thus, the robustness of the method with respect to local intensity variations is improved. In addition, the technique takes the local orientation of the vessel into consideration, thus leading to better tracking performance.

(a)   (b)
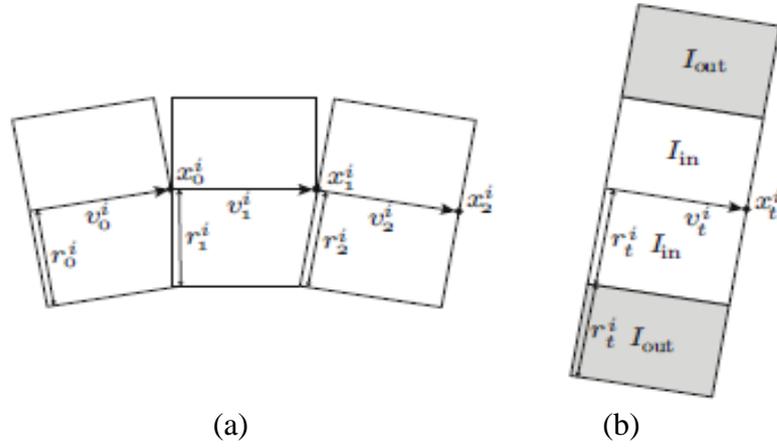
Figure 2.7: Illustration of approximating a vessel by a series of tube segments [77]. (a) Part of the tubular approximation, where r denotes the radius of the tube segment, v is the step length of the tracker (i.e., the width of the tube segment) and x represents the orientation of the tube, (b) The local region of interest defined as the regions inside and outside the tube.

The aforementioned models define vascular structures using the 2D planes perpendicular to the vessel centreline, which is not sufficient in modelling 3D vascular structures, since these approximations do not fully exploit 3D information. Schaap *et al.*, [77] proposed modelling the vessel as a series of short tubes, characterised by its location, orientation, average radius and the mean intensity inside the tube, to more robustly and accurately describe the vessels (see Fig. 2.7). Under the assumptions that vessels are brighter than the background, and the intensity distributions within the vessel and the background are homogenous, they design their observation model in a similar way as the ribbon metric in the Florin *et al.*, method, which maximises the mean intensity differences of the interior and

26

exterior areas of the tube segment. In order to deal with spatially varying intensity distribution, the full histogram information is utilised in modelling the appearance information of the vessel to be segmented in their refinement work [78]. Specifically, the Bhattacharyya metric, measuring the difference between distributions, is applied to measure the local contrast and the difference between the prediction and the observation. Worz *et al.*, [79] propose using a 3D parametric intensity model as the measurement for the particle filter, where the model is defined by using a 3D cylinder with Gaussian distributed profiles along the normal direction of the cylinder. To obtain a closed form representation of the model, the cylinder is constructed using a mixture of the two cylinders with different widths, as described in [80]. The measurement model, in their method, is defined as the least squares fitting error between the predicted model and the image intensities with the region of interest defined by the cylinder.

Rather than using the parametric cylinder/tube model to represent the vessels, Lesage *et al.*, [81] propose an alternative way of delineating 3D vascular structures, where the vessel is modelled as an envelope of spheres with different centres and radii [52, 53]. The reliability of the estimation is evaluated using the gradient flow through the outer surface of the sphere, which infers the degree of alignment of the estimated sphere to the vessel boundaries. In a departure to the conventional particle based methods using a limited number of particles to update the posterior probabilities in the update stage, they propose using a wide range of samples in the prediction stage to accommodate broader hypotheses. Zhao *et al.*, [82] modified the sphere model by extending the region of interest to the space around the original sphere, where the geometric model consists of two layers: the core (i.e., the original sphere) represents the foreground, while the outer layer (sphere) corresponds to the background. Rather than modelling the intensity pattern within the region of interest parametrically, they propose the use of a non-parametric estimation algorithm to adaptively approximate the intensity appearance. In CT angiography, the boundaries of the vessel are usually blurred owing to the partial volume effect. To account for such effects, the appearance of the vessel is modelled as a weighted combination of the vessel lumen and boundary patterns. Based on the assumption

that the contrast agent will not affect the intensity patterns of the vessel wall, the boundary appearance is constructed offline based on training images. For the measurement model, they propose the use of the Earth Mover's distance as the local contrast metric to measure the difference between the background and the vessel.

In particle filter based tracking problems, it is popular to choose the sampling importance density function $q(\cdot)$ as the prior probability density function of the state, which leads to a simplified weights updating scheme, i.e., the weights are solely dependent on the measurement density. However, such a choice is not trivial, as the particles are drawn from this distribution, inappropriate selection of the importance density function may lead to the random particles located far from the optimal solution, thus affecting the accuracy of the approximation of the posterior PDF of the state. One may suggest generating a large population of particles to cover a wider solution space. However, this is at the expense of increasing the computational complexity. Cetingul *et al.*, [83] propose the design of the importance density function based on a nonlinear pivoting filter [84], which is a local orientation descriptor to identify the local direction of vascular structures. This approach was applied in tracking of vascular structures using Dijkstra based method [39], discussed previously in Section 2.1.2. The pivoting filter consists of two components derived from both cross section and tubular intensity properties. Specifically, one metric detects the possible vessel directions by comparing the intensity variation between the boundary of the previous orthogonal cross section and the intensity variation along that orientation. The other one, measures the intensity homogeneity along the detected direction. By modelling the importance density function based on the pivoting filter, the drawn particles have higher probabilities to be located in positions near the final solution.

2.1.3 Active Contour Models Based Vessel Extraction

Active contour models, also known as snakes, are elastic splines fitting to the image contents based on the detected features. Since their introduction as a means of front propagation based segmentation methods, active contour models are receiving a great amount of attention by the medical image processing community.

To the best of our knowledge, the first use of the snakes for solving image segmentation problem was reported by Kass *et al.*, [85], following this seminal work, numerous research effects have been dedicated to design the active contour based energy functionals for various image segmentation tasks. Broadly speaking, image segmentation by means of active contours is performed by iteratively deforming a contour/surface until the user-defined energy functional is minimised. The energy of the active contour often depends on its shape (internal energy) and its position in the image (external energy derived from the image), and can be defined as:

$$E_{Snake} = \int_0^1 E_{Int}(\textbf{\textit{v}}(\textbf{\textit{s}})) + E_{Ext}(\textbf{\textit{v}}(\textbf{\textit{s}})) + E_{Con}(\textbf{\textit{v}}(\textbf{\textit{s}}))d\textbf{\textit{s}} \qquad (2.13)$$

where E_{Ext} gives rise to the external force driven from image features. E_{Con} represents the constraint force defined by the user or prior knowledge. E_{Int} denotes the internal energy of the snake, which is usually defined as a combination of the elasticity ($\textbf{\textit{v}}'(\textbf{\textit{s}})=d\textbf{\textit{v}}(\textbf{\textit{s}})/d\textbf{\textit{s}}$, $v(s)$ is the medial axis and s is the parameterisation variable) and the stiffness of the medial axis ($\textbf{\textit{v}}''(\textbf{\textit{s}})=d^2\textbf{\textit{v}}(\textbf{\textit{s}})/d\textbf{\textit{s}}^2$):

$$E_{Int} = \int_0^1 (\alpha \, | \, \textbf{\textit{v}}'(\textbf{\textit{s}}) \, |^2 + \beta \, | \, \textbf{\textit{v}}''(\textbf{\textit{s}}) \, |^2)d\textbf{\textit{s}} \qquad (2.14)$$

α and β are constants, controlling the contribution of each term to the internal energy. The parametric representation of the snakes cannot directly handle topological changes during contour evolution, unless dedicated processes are applied to deal with the possible split and merge of the contour. Level sets methods [21, 86], implicitly representing the active contours by embedding them into the zero level of a higher dimensional level set function, are capable of accommodating changes in topology in a natural framework. Hence, level sets based active contour models, also known as geometric active contours [50], became one of the most popular methods in vessel segmentation. As illustrated in Fig. 2.8, in level sets method, the contours $C(\textbf{\textit{x}})$ are often represented implicitly as the iso-contours (the interface) of a higher dimensional signed distance function, known as the level set function.

$$C(\boldsymbol{x},t) = \{\boldsymbol{x} | \phi(\boldsymbol{x},t) = 0\} \tag{2.15}$$

where ϕ stands for the signed distance function, $\boldsymbol{x}$ is the spatial parameters describing the contour and t is an artificial evolution time. In this thesis, we assume that $\phi(\boldsymbol{x},t) < 0$ represents the region outside the curve, while $\phi(\boldsymbol{x},t) > 0$ defines the region inside the curve.
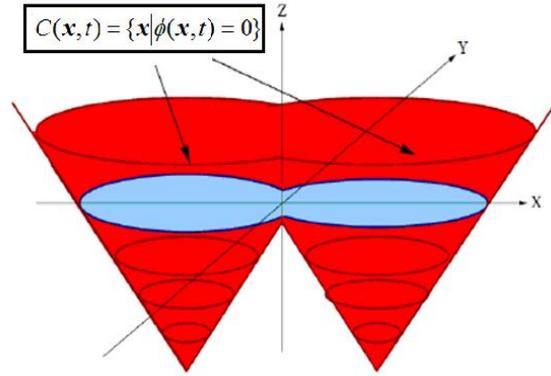
Figure 2.8: Illustration of the implicit contour representation. The contours are represented as iso-contours (interface) of a level set function [86].

The evolution of the surface (the level set) along its normal direction is controlled by the following equation:

$$\phi_t + V \cdot \nabla\phi = 0 \tag{2.16}$$

where the subscript t denotes a temporal partial derivative in the time variable t. The speed function $V(\boldsymbol{x})$ defines the velocity at each point of the surface (level set) and is usually derived from the image content features. Existing algorithms using level set based active contour models can be generally categorized in two groups, in terms of the image based energy, namely, edge based and region based models.

The application of edge based models to image segmentation was pioneered in [50, 87], where active contours are represented using geodesic formulations. The authors have mathematically demonstrated that the energy minimisation problem of the active contour models is equivalent to finding the geodesic curve (i.e., the minimal length curve between two points) in Riemannian space based on the image content features. In these methods, the difference of Gaussians (DoG) is utilised as

the edge detector to derive the image based energy, and thus, the front evolution is terminated when it reaches high image gradient regions. In the initial work, the external energy is defined based on the local edge detectors, which makes the resulting solution sensitive to image noise and contour initialisation. Yang *et al.*, [88] proposed an improved algorithm for segmentation of coronary arteries based on a Bayesian probabilistic framework. In their method, the image driven energy is redefined using posterior probabilities, based on the global histogram distributions, to more accurately terminate the evolution of surfaces at the desired boundaries. Specifically, they assume that the histogram of the coronary CT image consists of three classes, which corresponds to the lungs areas, the soft tissues and the contrast media filled regions (i.e., blood filled regions, including the blood vessels and pools). Three Gaussian functions are used to model the prior probabilities for each voxel belonging to these pre-defined classes. The posterior probabilities, obtained based on the Bayesian rule, are then used to derive the image energy by measuring the differences between the posteriors for each voxel being classified as the blood filled regions and the others. Since the posterior probabilities are obtained from global statistics, the method cannot handle the varying brightness and contrast changes over the entire image. Hence, it is not capable of segmenting small and distal segments of the coronary arteries due to their relatively low intensity and contrast.

The leakage problem, where the contour leaks into adjacent regions during curve propagation, is often encountered in medical image segmentation when using local gradients as the stopping criterion. This occurs in the case where the boundaries between different objects cannot be clearly defined by the gradients. Shape priors [89, 90], usually obtained from a training set, have been incorporated into the active contour framework as hard constraints, which greatly improve the segmentation results when the objects to be extracted have the similar shape to the ones present in the training sets. Leventon *et al.*, [91] propose parameterisation of shape priors using the signed distance function and the correspondence between the samples is roughly established by the Eigenfaces method [92]. The principal shape variations of the given training set are determined through the application of principal

component analysis (PCA) and are fit to the Gaussian distribution, which defines the probability distribution on the shape. In the conventional methods, the pose parameters (i.e., the rotation, translation and scaling factors) need to be optimised in order to align the shapes between the current segmentation and the template by comparing their differences, which introduces additional difficulties in the numerical implementation as these pose parameters cannot be simultaneously optimised using a gradient descent method. Cremers *et al*., [93] propose alleviate solution to this problem by using a translation and scaling invariant shape prior. Instead of evaluating the shape difference using the global coordinates, they propose to align the shape with respect to its centre of gravity and normalise the area of the object to unity, which leads to a shape representation invariant to scaling and translation. In contrast to classical methods modelling the probability of the shape using a Gaussian model, in their method, the probability distribution on the shape of the training set is derived by a non-parametric kernel density estimation method, which allows for more accurate estimation of the probability densities of the shape prior.

(a)   (b)
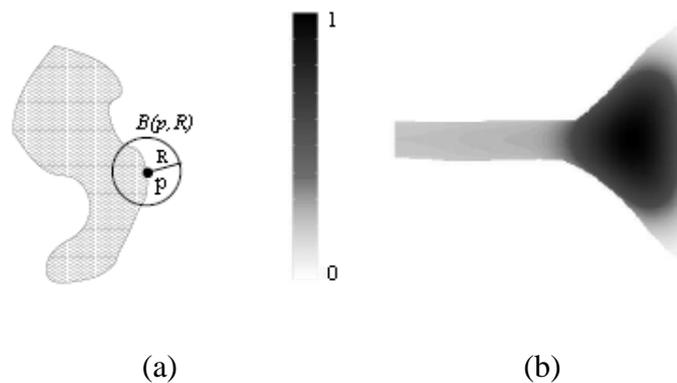
Figure 2.9: A graphical example demonstrating the effect of the shape filter. (a) Illustration of the shape filter centred at *p* and with the radius *R*, (b) The output of the shape filter [94].

However, reliable shape priors are in general difficult to determine in practice due to the high inter-patient variability of the vessel geometries and the limited availability of training datasets. To address these problems, Nain *et al.*, [94] incorporate a soft shape prior into the conventional active contour model. They

propose the application of a shape filter to locally describe the shape of the segmented region. As illustrated in Fig. 2.9, the shape filter is defined as a ball structure centred on each point along the contour with radius r. This measures the percentage of voxels belonging to both the ball and the object (i.e., the regions inside the contour). The output of the shape filter is high when the current point belongs to a region corresponding to leakage. Conversely, lower values of the filter's output indicate that the current point is within the vessel. The filter response then serves as the external energy of the active contour, penalising leakages during the curve evolution. However, the shape filter cannot discriminate vessel bifurcations from leakage areas, and may result in undesired gaps in the vicinity of vessel bifurcations. Gooya *et al.*, [95] proposed the use of an anisotropic regularisation force, which is designed to detect the local front orientation and encourage the surface evolving along the elongated direction, to reduce the risk of leakage when segmenting vascular structures. In the propose method, the correlation matrix of the image gradient [96] is employed as a descriptor to estimate the local surface structure. For each point along the active contour, the correlation matrix is derived from the regions defined by the intersection of a ball structure, centred at each point on the contour with a radius R, and the interior of the contour. The elongated direction of the object can be identified by analysing the eigenvalue patterns of the correlation matrix. Since this method enforces the front propagate along the elongated direction, possible leakages caused by ambiguous edge can thus be limited. Topological properties have also been utilised to address the leakage problem. Manniesing *et al.*, [97] impose a shape constraint on the topology of the segmented vessels, where the skeleton of the front is used to guide the contour evolution.

Contrary to edge based active contour models, which characterise image content based on a small neighbourhood of pixels, region based methods, relying on global information obtained from image regions, are more robust to weak or inhomogeneous gradients at the edge locations as well as insensitive to image noise. Region based segmentation methods generally seek to partition regions in terms of common image features. Early work in region based segmentation using variational

principles was reported by Mumford and Shah [98], where they proposed solving the image segmentation problem by decomposing image *g* into a set of disjoint sub-regions R_i, such that:

$$R_1 \bigcup \cdots \bigcup R_n = R$$

where R_i is associated with the image sub-regions as a partition of the image domain *g*, and they assume that the image content within each region R_i varies smoothly, which is known as the piecewise smooth (PS) or cartoon model. The above segmentation problem can be solved through an energy minimisation process:

$$E(f, \Gamma) = \mu^2 \iint_R (f - g)^2 \, dxdy + \iint_{R-\Gamma} \|\nabla f\|^2 \, dxdy + v|\Gamma| \qquad (2.17)$$

where *f* stands for the function approximating the image content *g*, and Γ denotes the boundaries between the different image regions R_i. μ and *v* are constants controlling the weights of each individual energy term. Based on this concept, Zhu and Yuille [99] proposed the interpretation of the regional intensity variations as a random variable with a probability density which needs to be determined based on regional information. The image segmentation problem is solved by minimising a minimum description length (MDL) criterion based on the Bayesian rule. Later on, Chan and Vese [51] proposed the solution of the Mumford-Shah functional minimisation problem using the level sets based active contour methods, where they developed a reduced form of the PS model by assuming that the image consists of homogenous regions, thus leading to the piecewise constant (PC) model. The associated energy functional is defined as:

$$F(c_1, c_2, C) = \mu \cdot length(C) + \lambda_1 \int_{inside(C)} [I(\boldsymbol{x}) - c_1]^2 \, d\boldsymbol{x} + \lambda_2 \int_{outside(C)} [I(\boldsymbol{x}) - c_2]^2 \, d\boldsymbol{x} \quad (2.18)$$

where *C* is a closed contour(s), which is usually used to delineate the boundaries of the objects to be segmented, *inside*(*C*) are the regions inside the contour *C*, and *outside*(*C*) represents the regions outside of the contour. c_1 and c_2 denote the mean intensity values inside and outside the contour, respectively. *I(**x**)* is the gray level intensity value at pixel **x**. μ, λ_1 and λ_2 are constants, controlling the weights of the

individual energy terms. This work was later extended to multiple phase images, where the image consists of more than two homogeneous regions [100].

Following the seminar work by Chan and Vese, Rousson *et al.*, [101] proposed the use of the two parameters of the Gaussian function (i.e., both the mean and the variance) to more robustly and accurately model the region statistics. Lecellier *et al.*, [102] extended the Gaussian parametric model to the entire family of exponential functions and proposed a general framework for optimisation of the associated energy functional. In their approach, image intensities are treated as random variables whose distributions belong to one of the exponential parametric models, and their parameters are estimated using the Maximum Likelihood (ML) method. The probability density function of image regions, however, cannot always be accurately approximated by parametric models, especially when the prior statistical information about the image regions to be segmented is not available. Non-parametric methods are preferred in this case, for their capability of dealing with complex distributions without assuming any prior knowledge. Michailovich *et al.,* [103] proposed using the full histograms of image regions, obtained by kernel density estimation (KDE) algorithms, as regional descriptors for image segmentation. In their method, the Bhattacharyya distance is employed as the discrepancy metric to measure the similarity between two distributions (histograms), and is to be minimised at the boundaries of the objects to be segmented. Kim *et al.*, [104] proposed the application of information theory to solve the active contour segmentation problem. In their method, region labels, $L(x)$, a Boolean function indicating whether the current pixel x should be classified as belonging to the object, are defined at the location of each pixel of the image. The value of the labels is determined based on Bayes rule, where the prior probability density function of the image regions inside and outside the active contour is estimated using the Parzen window. Hence, image segmentation can be achieved by maximising the mutual information between the region labels and the image intensities.

(a)   (b)   (c)
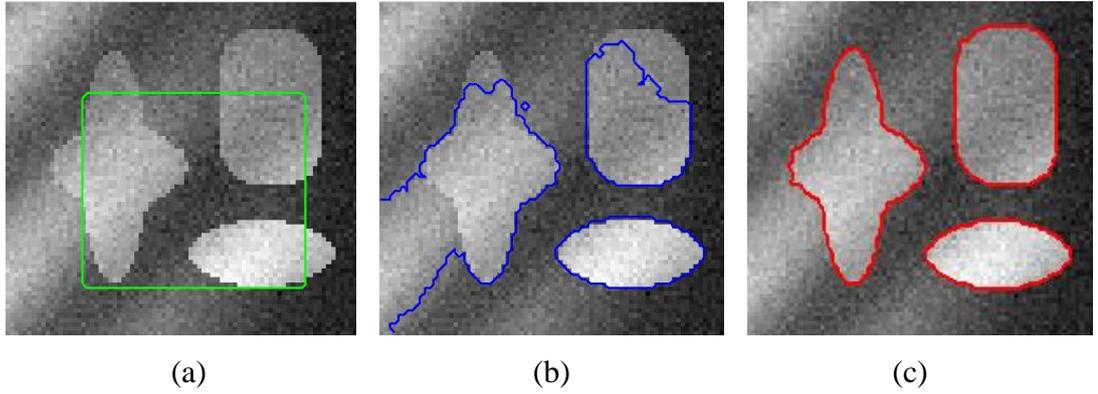
Figure 2.10: A synthetic image illustrating the erroneous segmentation caused by using global statistics in the presence of non-uniform illumination. (a) Contour initialisation, (b) and (c) the final segmentation results obtained using basic/localised Chan and Vese methods, respectively.

As illustrated in Fig. 2.10, the aforementioned methods, based on global intensity statistics, are inefficient when regional statistics is spatially varying across the image. Image intensity inhomogeneity is often encountered in medical images due to the acquisition artifacts and the attenuation of the contrast media. Localised approaches, estimating regional statistics in a neighbourhood of the active contour, have recently emerged to overcome this problem. In these methods, the image based energy functional is generally defined in the following form:

$$E = (\oint_{C(\boldsymbol{x})} \int_{\Omega_{x}} (k(\boldsymbol{x}, \boldsymbol{y}) g(\boldsymbol{x}, \boldsymbol{y}) d\boldsymbol{y}) d\boldsymbol{x} \qquad (2.19)$$

where $C(\boldsymbol{x})$ denotes a closed contour(s) representing boundaries of the objects to be segmented. $k(\boldsymbol{x},\boldsymbol{y})$ is a non-negative localised kernel function returning the weights for each pixel within the neighbourhood centred at $\boldsymbol{x}$, which defines a localised image, Ω_{x}, around $\boldsymbol{x}$, and $g(\cdot)$ is a generic function measuring the overlapping between distributions (derived from the image regions inside and outside of the active contour within the local region Ω_{x}, respectively). For instance, in the localised PC model [105, 106], the localised image-driven energy term $g(\cdot)$ can be written as:

$$g(\boldsymbol{x}, \boldsymbol{y}) = \int_{in(C(\boldsymbol{x}))\cap\Omega_{x}} k(\boldsymbol{x}, \boldsymbol{y})\{[I(\boldsymbol{y}) - c_1]^2 + \int_{out(C(\boldsymbol{x}))\cap\Omega_{x}} [I(\boldsymbol{y}) - c_2]^2\}d\boldsymbol{y} \qquad (2.20)$$

where c_1 and c_2 represent the mean intensity values inside and outside the active contour within the local region Ω_{x}. By introducing the localised kernel $k(\boldsymbol{x},\boldsymbol{y})$, the

active contour evolution is based on local decisions, thus improving the overall performance of the segmentation under changing brightness conditions, as there is less brightness changes in a local image (see Fig. 2.10(c)). In PC active contour models, the overlapping between distributions is measured in terms of the mean intensity values derived from image regions, which cannot separate distributions with similar means but different variances. To more robustly describe local regional statistics, Wang *et al*., [107], propose taking into account the variance of image regions and modelling region statistics by Gaussian distributions. Similarly, Darolti *et al.*, [108] proposed a disparity metric using confidence intervals to locally determine if a voxel should be classified as belonging to the object in terms of the mean and variance derived from local image regions. The authors further proposed using the local Markov Random Field (MRF) model as the disparity metric to deal with largely overlapping probability density distributions. Lankton *et al.*, [109] proposed a general localised region based active contour framework, which allows for the incorporation of any region based energies (such as the Bhattacharyya distance [103]). However, the selection of an appropriate scale for the localised window is an important tuning parameter and can greatly affect the segmentation performance. A small size of localised kernel makes the active contour sensitive to initialisation since only a small group of voxels, i.e., the ones near the contour, are taken into account in contour energy calculation. On the other hand, too large a size for the local window will include more voxels in the decision process, which may introduce possible image artifacts and image inhomogeneity. Piovano and Papadopoulo [110] addressed this difficulty by adaptively varying the width of the local window. In their method, they compute the speed (active contour energy) for each point on the contour over multiple scales, and the smallest scale, which leads to the evolution speed at such point being greater than a given threshold, is chosen as the optimal scale at that point. By doing so, the proposed method favours small neighbourhoods near the locations of edges, while a larger window size is chosen in the case of homogenous regions.

One of the major drawbacks of standard level sets methods is the large amount of computational resources required to solve the evolution equations over the entire

image domain. Narrow band based methods [21, 41, 111], which update the level set function near the curve (zero level set) at every time step, are commonly employed to improve the efficiency of level sets based segmentation algorithms. In conventional approaches, the level set function needs to be periodically re-initialised in order to maintain it as a signed distance function, which impacts on the efficiency of the algorithm. To remedy this issue, Li and his colleagues [112] proposed the introduction of a constraint energy term into the framework of geometric active contours, which penalises the level set when it deviates from a signed distance function. Since their method removes the need for re-initialisation, the efficiency of level sets based active contours has been significantly improved.

2.2 Quantitative Coronary Analysis

Quantification of the resulting segmentation of coronary arteries (e.g., estimation of the degree of luminal narrowing and quantification of the plaque volume), obtained through manual delineation or automated methods, provides important information about the associated risks of developing cardiovascular disease for the patient, and is beneficial for reviewing the results of cardiac interventions.

(a)   (b)
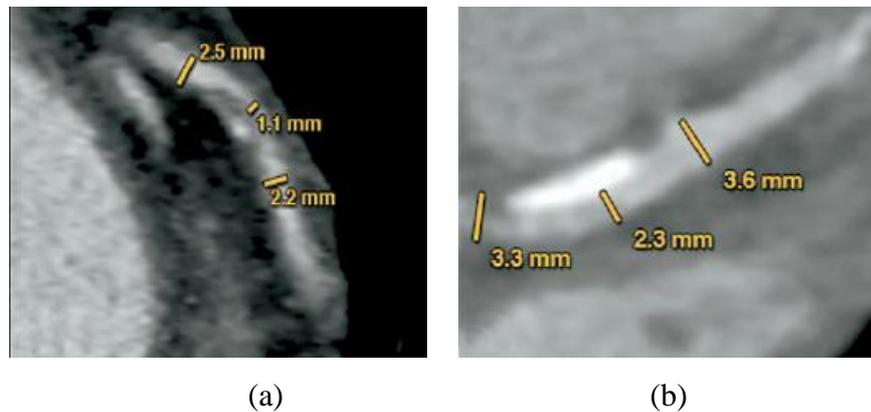
Figure 2.11: Examples of the stenosis quantification scheme. Illustrations of the quantification of the severity of stenosis for (a) soft, and (b) calcified stenotic plaques [113].

The severity of coronary stenosis, determined through visual inspection, is measured using a binary approach with 50% luminal diameter narrowing as a cut-off [114]. However, such binary description of coronary stenoses may usually exclude the 'intermediate' stenosis (which could lead to slightly less than 50%

narrowing) and cannot sufficiently describe clinical information with regards to obstructive lesions. For diagnostic purposes, accurate discrimination between mild, moderate and severe stenotic plaques is required. To this end, Cheng *et al*., [113] proposed a multi-tiered evaluation scheme for grading coronary stenoses based on the longitude image of the arteries. In the proposed method, all of the non-stent coronary segments with a luminal stenosis of >25% are flagged for further examination. As illustrated in Fig. 2.11, for each stenotic plaque, the reference vessel regions located prior and distal to the lesion and the minimal diameter at the site of the stenosis are determined manually, and the corresponding luminal diameters (D_{prox}, D_{dis} and D_{sten}) are quantified using semi-automated software. Then, the reference vessel diameters (i.e., the normal luminal diameters) along the vessel segment between the two reference sites are determined by linear interpolation. Hence, the maximum degree of the stenosis can be calculated as follows:

$$\text{Stenosis} = [1 - (D_{sten})/(D_{prox} - ((X_1/X_2) \cdot (D_{prox} - D_{dis})))] \qquad (2.22)$$

where X_1 and X_2 denotes the distances between the two reference sites, and from the proximal reference site to the maximal degree of stenosis, respectively. Their study has shown that semi-automated quantification has a high degree of agreement with the manual evaluation, however it does not improve the overall accuracy of the measurement. This is partially because the quantification method requires a certain amount of user interaction, including determination of the reference points and the stenotic sites, which introduces significant variability in the resulting analysis.

To improve the objectivity and reproductivity of the assessment regarding the severity of coronary stenosis, semi- or fully automated systems have been developed to reduce the amount of user engagement. Joshi *et al.*, [115] reported the use of a computer-aided system to perform quantitative analysis of coronary stenosis using IVUS as the reference for validation. The semi-automated analysis commences from extraction of the arterial centrelines and detection of the associated lumen areas based on the user-provided endpoints. Then, a refinement process is conducted manually to ensure the correctness of the detected coronary lumen. Next, the physician is required to determine the two reference regions,

located proximal and distal to the lesion, and the associated geometrical parameters (i.e., luminal diameter and cross sectional area) regarding the stenotic plaque are subsequently calculated by the software in an automated fashion. As such semi-automated system significantly reduces the amount of the user interaction; diagnostic results by means of CT angiography have shown an improved correlation with the standalone procedure using intravascular ultrasound (IVUS).

Despite the promising results obtained using semi-automated approaches for quantification of coronary stenosis, such methods still suffer from large variability in terms of diagnostic accuracy and have a low rate of reproductivity due to the manual interfaces, introduced in the evaluation process. Hence, there is a need for development of a dedicated system to perform the quantification in a fully automated manner, which could further improve the accuracy and reproductivity of the evaluation. Boogers *et al.*, [116] applied an automated software (QAngioCT 1.1, Medis Medical Imaging Systems) to quantify the degree of stenosis in CT angiography images. The analysis starts with the extraction of the 3D centreline of the vessel of interest (starting from the root of the artery to its distal segment) through a vessel tracking algorithm. Next, the stretched multiplanar reformation (MPR) method [117] is employed to create the four longitude vascular volumes at 45° intervals, which allow for the visualisation of the curved arteries as straight vessels. Then, the boundaries of the longitudinal multiplanar reformatted images are detected using a model based minimum cost algorithm, which utilises a combination of image derivatives and a circular shape model as the minimum cost energy functional. In the subsequent step, the luminal diameters and the perpendicular cross sectional areas along the course of the vessel segment are determined and these data is further processed to quantify the severity of coronary stenosis.

Coronary bifurcation lesions constitute a challenge for interventional cardiology. Conventional methods, however, are commonly developed for quantitative analysis of the 'straight' segments of vessels and have limitations in precisely defining the location of the centreline and the true reference lumen surface for both the main vessel and the side branch in the vicinity of bifurcations. To address these issues,

Wong and Chung [118] proposed using a deformable model based method to recover the healthy shape of the abnormal vessels in 3D angiography images. In their method, the original shape of a diseased vessel segment is reconstructed by registering a circular cross sectional tube to the vessel boundaries in normal regions. The method was further developed to incorporate the user's guidance to trace the vessel axis in the presence of complex vascular structures, such as multiple branching, kissing vessel artifacts and aneurismal lumens [119]. Despite this approach being able to generate centrelines in complex vascular structures, it still suffers from a number of problems, as follows. Firstly, their method is sensitive to initialisation, since the width along the tube model is determined by linear interpolation between two manually selected ending cross sections. It may result in under- or over-estimation of the area of tubular cross sections due to the non-linear nature of the vessel, and thus, produce erroneous estimations of vessel centrelines and the reference surface. Moreover, the tube deformation process is carried out in the voxel domain, which requires upsampling of the original volume to calculate the image-based energy due to insufficient resolution. Different image upsampling methods could dramatically affect the magnitude of the image-driven energy, which leads to non-unique solutions for the tube registration problem.

Similar work was also reported in Kang *et al*., [120], who proposed the classification of the region of interest (ROI) to one of three types, namely, normal, stenotic and aneurismal (corresponding to bifurcations), prior to model registration. The initial segmentation of the ROI is obtained based on a region growing algorithm, which uses two user-defined points. Then, an active tube model is fitted to the ROI by minimising a snake-like energy functional. In a departure from previous deformable model based methods, calculating cross sections based on the centreline points, they propose the determination of the cross sections by extracting the iso-surface of the complementary geodesic distance field, which allows for the cross sections of the vessel to be determined uniquely and independently of the fitted centrelines. In this method, the classification of the ROI is based on the segmented image, obtained using a region-growing algorithm. The 'leakage problem', which is commonly encountered in region-growing based segmentation,

however, could result in erratic classification of the ROI and subsequently degrade the performance of the method.

Ramcharitar *et al.*, [121] developed a dedicated method for quantitative coronary analysis of bifurcation lesions in 2D X-ray angiography images. Based on the two user-defined points (before and after a vessel bifurcation), a circle fitting algorithm is firstly applied to detect the point of bifurcation and segment the bifurcation area. The reference diameter within the bifurcation region is subsequently determined by a minimum freedom approach. The method was later extended to quantify abnormal vessels in 3D images in order to eliminate foreshortening and out-of-plane magnification effects, which are commonly encountered in 2D angiograms [122]. The 3D artery model, however, is reconstructed from different views of the projection images. The accuracy of the reconstructed model depends on the selection of the projection angles and the assumed vessel model (e.g., a circular cross sectional tube), which impacts on the re-productivity of the results.

In addition to measuring the degree of coronary stenosis, a lot of research efforts have been dedicated to quantify the plaque volume (e.g., measuring the size of the plaque). However, the blooming effect, which is a partial volume artefact, which occurs during high radiation exposure in the case of high attenuation objects (e.g., the calcifications), results to such objects appearing larger, this is commonly encountered in CT angiography due to the limited spatial resolution. Image deconvolution techniques [123] have been proposed to suppress such effect by solving the inverse problem of estimating the true size of the object from the images. Conventional deconvolution methods, however, may amplify image noise and artifacts which are usually associated with the high frequency components of the image spectrum. Hijarrubia *et al.*, [124] proposed a histogram based selective deblurring algorithm to restore the true size of high intensity objects (i.e., calcified plaques) while maintaining the information of the remaining regions in CT images. In the proposed method, the deconvolution is firstly performed using the Wiener filter [125], with a point spread function (PSF), obtained during training, using the information available from the phantoms. Then, the calcified regions, in both original and deconvoluted images, are identified using a region growing method.

Next, the transition regions are determined by finding the difference between the calcification volume in the original and deconvoluted images, and restored through the linear interpolation between the two regions. At last, a smoothing process is applied to the transition regions to generate the final results. However, the point spread function, in their method, is estimated in an *ad hoc* manner, which makes the estimation highly correlated to the image modalities and the configuration during the image acquisition process. Cline *et al.*, [126] presented an automated system for recovering the true size of the calcified plaques in CT angiograms. In the proposed method, the blooming effect of CT images is modelled as the convolution of a noise-free image with a Gaussian distributed PSF, derived from the imaging system. The variance of the PSF is estimated from the intensity profiles across a sharp edge, such as the interface between the lungs and myocardium. The core of the calcified plaques, determined by thresholding, is then convolved with the PSF to obtain the estimated plaque volumes.

2.3 Coronary CT Image Interpretation

Accurate and efficient interpretation of coronary CTA images is an essential and important component in the visual examination of coronary arterial disease, which provides the physician with reliable diagnostic information about the state of the coronaries. In the following subsections, the most commonly used post-processing techniques for the interpretation of coronary CT studies, including transaxial examination, multiplanar reformation (MPR), curved planar reformation (CPR) and volume rendering (VR) will be introduced. The focus of this review is to provide a high-level description of these techniques, rather than their algorithmic details, as they are primarily related to visualisation aspects, which are not within the scope of the current work. However, the terminologies introduced here will assist in understanding the evaluation framework used to validate our contributions, which will be presented in the following two chapters.

(a)   (b)
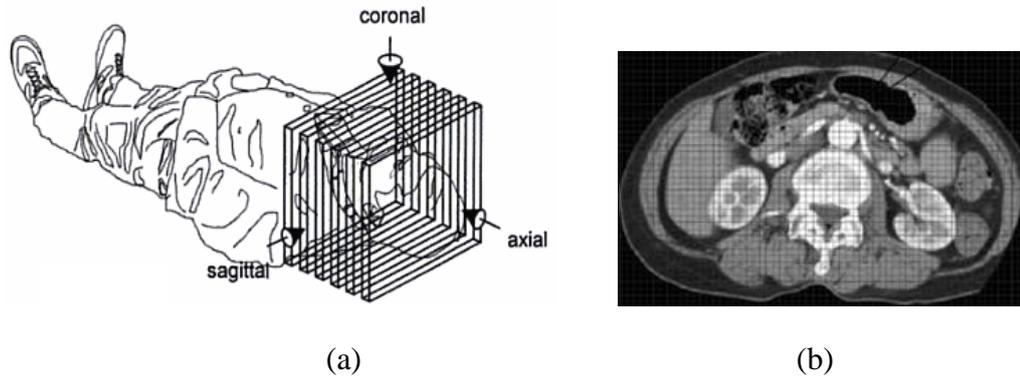
Figure 2.12: Illustration of the axial view of CT images. (a) The definition of the projection planes, (b) A transaxial image examination allows the visualisation of the 2D axial-projection image [127].

2.3.1 Transaxial Examination

Transaxial (axial) examination is a basic yet essential tool for CTA image interpretation. Axial images, reconstructed from the projection data (i.e., the initial result of CT acquisition and cannot be viewed directly) form the basis for generating 3D multiplanar reformatted images. In these images, the heart region is contained in a series of 2D cross sectional slices, stacked together to form the volumetric data (see Fig. 2.12), which provide the most common and meaningful information regarding the arteries. A typical 12-bit CT image contains up to 4096 different intensity levels, which cannot be discriminated by the human eye. *Window-Levelling* [128], an operation controlling the brightness and contrast of the image, is usually carried out during the visual reviewing process, in order to optimally visualise the object of interest. This technique maps the entire range of grey levels to a sub-range, which contains less intensity levels, and can thus be discriminated by the observer. The relationship between image contrast and brightness and the terms window and level are illustrated in Fig. 2.13. Making the window wider will decrease the image contrast, since more grey levels are displayed. The display brightness can be adjusted by moving the level left or right.
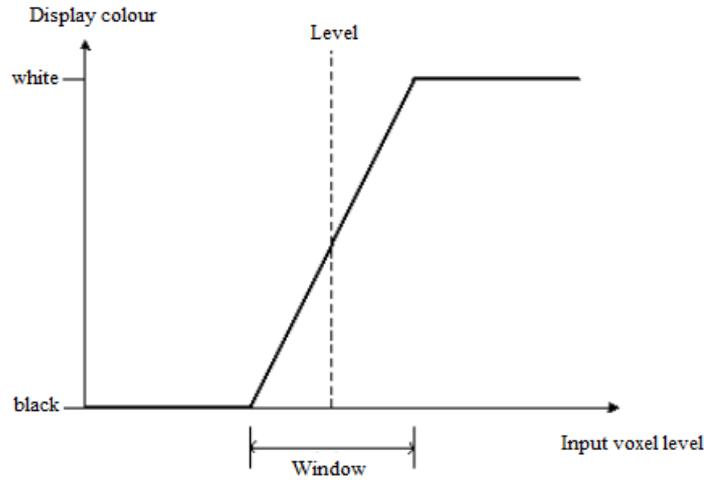
Figure 2.13: A diagram shows the relation between image contrast and brightness and the window-level settings.

2.3.2 Multiplanar Reformation

The routine transaxial images, where the volumetric image is projected onto the axial, sagittal and coronal viewing planes, are only able to provide limited viewing angles for inspection of the artery. Some segments of the coronary arteries, however, cannot be appropriately viewed in these basic transaxial images. Hence, the multiplanar reformation technique [129, 130] was proposed as a suitable solution for the generation of slice images with arbitrary orientations, as shown in Fig. 2.14.

(a)   (b)
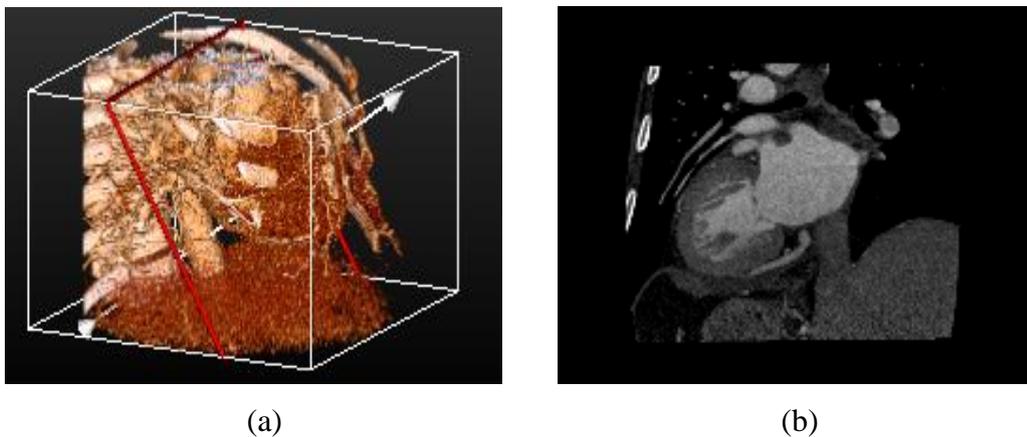
Figure 2.14: The images illustrate the multiplanar reformatted image reconstructed from the volumetric CT dataset. (a) 3D visualisation showing the volume rendered image of the thorax, (b) Image reconstructed from an off-axial plane, defined by the red rectangle shown in (a).

The multiplanar reformation problem can be solved by interpolating the original CT volume data along an arbitrary plane, where the intensity values of each voxel within the newly generated plane are determined from its neighbours. For visualisation purposes, the tri-linear interpolation algorithm is commonly employed to determine the intensities of the new viewing plane.

2.3.3 Curved Planar Reformation

Coronary arteries are tubular structures with relatively small luminal diameters and complex topologies. Hence, the aforementioned visualisation techniques, which display a cross section or a small fragment of the vessels, are not sufficient to exploit the 'global' properties of the entire vessel, such as the minimum and maximum luminal diameters and average X-ray attenuation. Curved planar reformation [11, 12] is a popular post-processing technique to visualise the entire vessel along its centreline within a single 2D image, where both the lumen and the surrounding tissue can be clearly displayed. In Fig. 2.15, we illustrate the CPR images of the left and right coronary arteries, respectively. It can be seen from these angiogram-like images that, the calcium (hyper-density components shown in Fig. 2.15(a)) deposited in the luminal area can be intuitively viewed.

(a)   (b)
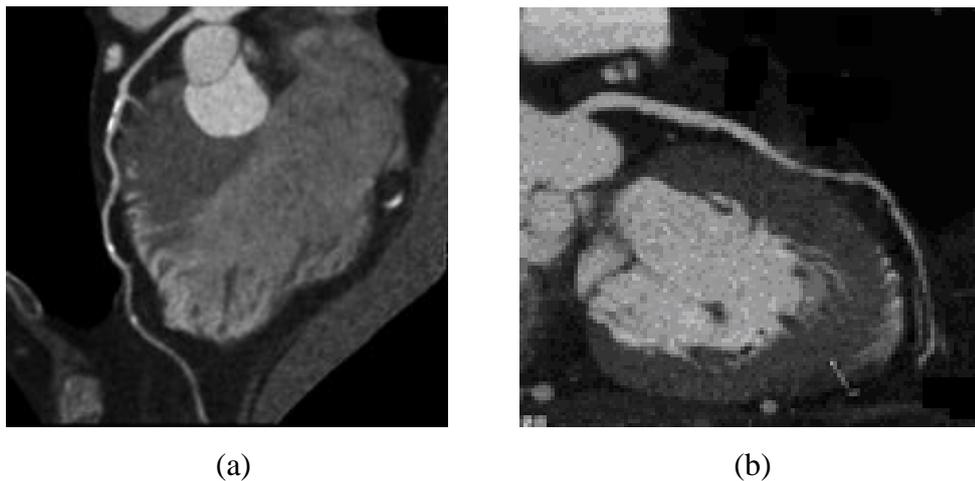
Figure 2.15: Visualisation of CPR images of the (a) left and (b) right coronary arteries.

2.3.4 Volume Rendering

The commonly used 2D CT image interpretation techniques are sufficient for the radiologists to get a 3D understanding about the pathology and anatomy of the patient. However, they may require a full 3D interpretation of the anatomical structures under examination for the preparation of the diagnostic report. Volume rendering, a technique which constructs a pseudo 3D interpretation of an object, generally assigns each element (voxel) of the image volume with a transparency measurement (known as the alpha map), which defines the opacity levels of that voxel, and maps the voxel intensities onto a pseudo colour map. The assignment of opacity and colour maps to the voxels is defined in terms of the imaging protocols and anatomical structures [131-133]. In Fig. 2.16, we illustrate the different settings for visualisation of the vessels and bones in 3D volume rendered images.
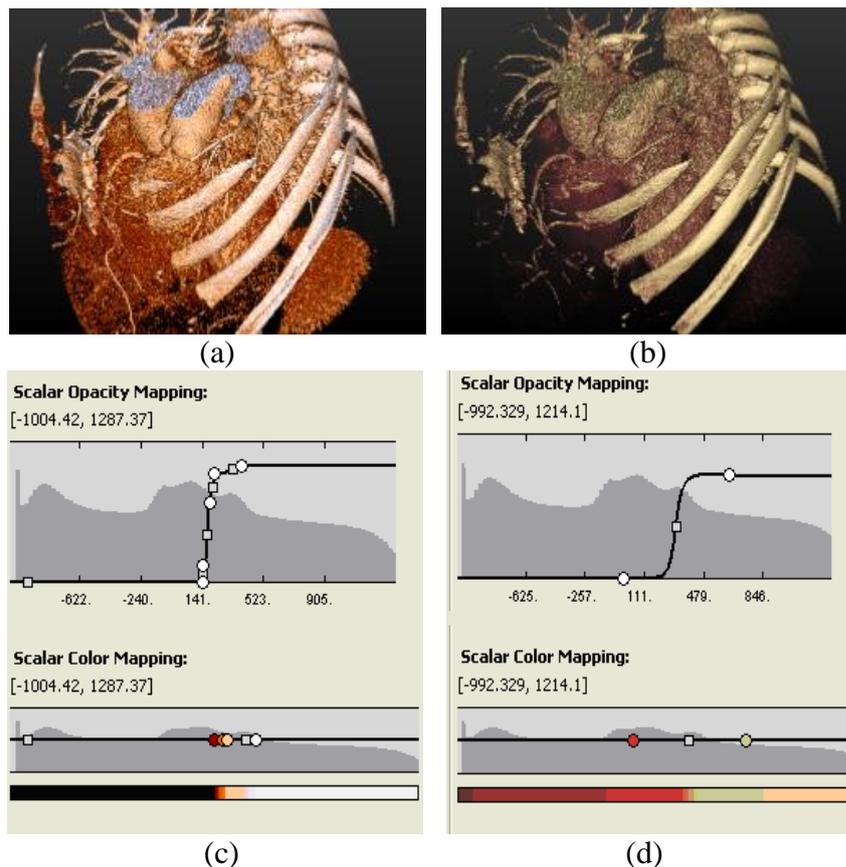
Figure 2.16: Examples of volume rendered views constructed from coronary CT angiography. (a) and (b) illustrate the volume rendered images with the alpha and colour map configurations, as depicted in (c) and (d), for visualising the vasculature and bones, respectively.

2.4 Conclusions

In summary, this chapter presented an overview of the state-of-the-art techniques in coronary image processing. We commenced our discussion by exploring the existing literature regarding vascular structures extraction algorithms. For each of the techniques described in the review section, the basic ideas, principles, developments as well as their limitations were discussed. This was followed by a brief introduction of quantitative coronary analysis methods in the assessment of the severity of luminal stenosis. Finally, we described commonly used post-processing techniques for interpretation of coronary CTA images, which are useful in illustrating the results of this research, reported in Chapters 3 and 4.

Numerous commercial and laboratory-based systems for quantification of coronary arteries have been developed based on various algorithms in recent years. However, there is no system that allows for the construction of the geometric model of a coronary artery with a single click, and often, manual interaction is required by trained staff, which may result in large intra- and inter-observer variability. Reproducible and accurate modelling of the geometries of the coronary is a key step towards quantitative coronary shape analysis (such as stenosis grading) and patient-specific haemodynamic studies. Thus, there is an immense need for the development of a fully automated system for the construction of patient-specific geometric model of the coronary arteries, with minimum user interaction. In the following chapter, we will present a novel framework for the segmentation of the coronary artery from cardiac CT images in a fully automated fashion, which facilitates the construction of the patient-specific models of the arteries.

Chapter 3

Segmentation of Coronary Arteries in 3D CTA Images

This chapter presents an innovative framework for segmentation of coronary arteries in 3D CTA images. It commences with the description of a series of image pre-processing techniques to define the region of interest and roughly identify the arteries in Section 3.2. This is followed by the presentation of the proposed two-step active contours model based segmentation algorithm in Section 3.3. In this method, both global and local intensity information are utilised in the active contours energy calculation. The global term is defined as a normalised cumulative distribution function (CDF), which contributes to the overall active contour energy in an adaptive fashion based on image histograms, to deform the contour out of local stationary points. Possible outliers, such as kissing vessel artifacts, are removed in a post-processing stage of the segmentation by a slice-by-slice correction scheme based on multiple regions competition, where both arteries and kissing vascular structures are identified and tracked through the slices. Section 3.4 demonstrates the efficiency and accuracy of the proposed technique on synthetic and real datasets and presents extensive performance evaluation results. Section 3.5 concludes this chapter.

3.1 Outline of the Proposed Algorithm

The flow chart of the proposed approach is shown in Fig. 3.1. It begins with a series of algorithms towards to the development of an automated pre-processing framework (Section 3.2), which defines the region of interest and generates the initial segmentation of the coronary arteries for the subsequent processing. Then, the coronaries are refined by using the proposed vessel segmentation technique, based on a generalised active contours model. Kissing vessel artifacts, which cannot

49

be identified in the first stage of the segmentation, are removed in the following step by using a slice-by-slice correction algorithm.
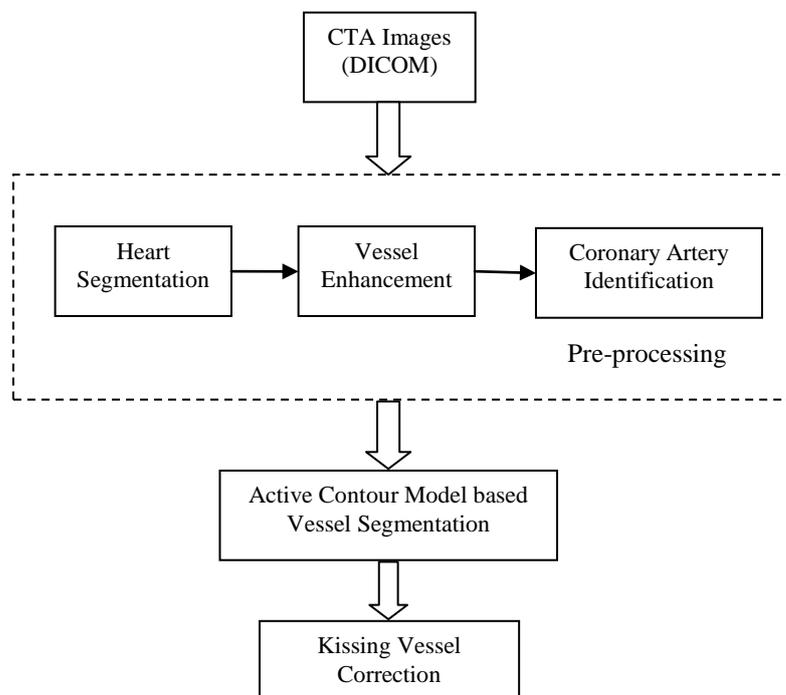
Figure 3.1: Flow chart of the proposed segmentation algorithm.

3.2 Coronary CT Image Pre-Processing

It is not efficient or necessary to process the entire volume image of a coronary CT study, since coronaries usually occupy only a small number of voxels. Hence, defining the region of interest and suppressing the irrelevant information is an important and essential step prior to the actual segmentation. In this section, we present an automated method to define the region of interest (i.e., the heart region) and roughly extract the arteries in 3D contrast enhanced CT angiography images. Specifically, Section 3.2.1 presents a fast yet efficient heart segmentation algorithm to extract the entire heart from the thoracic organs, which facilitates subsequent processing and allows for the coronaries, located at the outer surface of the heart, to become easily visible. In Section 3.2.2, we present a modification to the vessel enhancement filter in [33] to detect the vascular geometries within the heart region. Section 3.2.3 details the procedure for automated identification of the arteries from

the filtered image and the construction of the initial surface for the active contour based segmentation, discussed in the following section.

3.2.1 Fast Heart Segmentation

Fast and efficient heart segmentation (isolating the heart from nearby organs such as lungs, liver and ribs) is an important pre-processing step for segmentation of the entire arterial tree and facilitates the visualisation of coronary arteries in 3D. The purpose of this stage is not to establish an accurate segmentation of the heart, but rather to define the region of interest for subsequent processing. In this section, we propose a fast mathematical morphology based method to segment the entire heart from its surrounding organs. The transaxial CT images shown in Figs. 3.2 (a)-(h) are used as an example to provide the details of the proposed algorithm. The same procedure will be applied to other axial slices along the z-direction of the CT volume data to construct a complete 3D heart mask. Fig. 3.2(a) shows an axial image randomly taken from a CT study, and its associated histogram is shown in Fig. 3.2(b). The proposed method starts by detecting the lung regions using an optimal thresholding algorithm, where the threshold value is determined by finding the first peak of the axial image histogram. Next, a 'hole filling' algorithm [125] is employed to eliminate pulmonary vessels within the lungs, as illustrated in Fig. 3.2(c). Consecutively, by making use of prior anatomical information about the heart position with respect to the lungs, i.e., the heart is completely surrounded by the left and right lungs, the heart region is determined as the interior area of the lungs. Specifically, we firstly determine four critical points (or landmarks) on the lungs, corresponding to the rightmost and the leftmost points of the left and right lung, respectively. These points are then connected using the Bresenham line drawing algorithm [134] to enclose the area between the anterior and posterior mediastinum (see Fig. 3.2(d)). Then, the heart area can be defined by tracing the interior boundary of the previously obtained binary mask, as illustrated in Fig. 3.2(e). However, closing the anterior mediastinum using line segments may cut through the coronary arteries, located on the surface of the heart chambers, leading

(a)

(b)

(c)

(d)

(e)

(f)

(g)

(h)

(i)

(j)
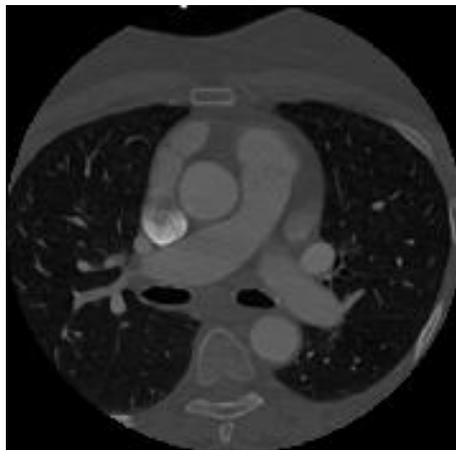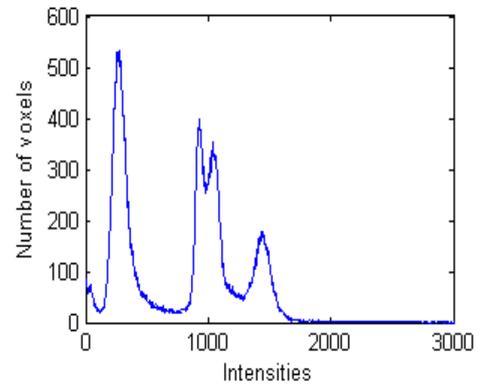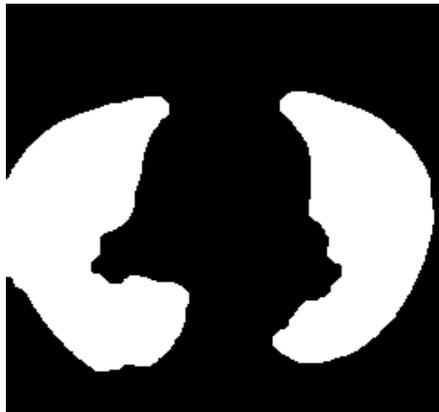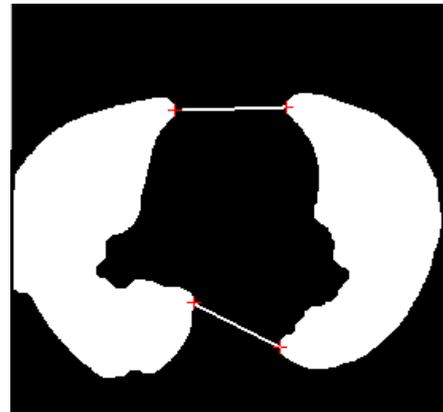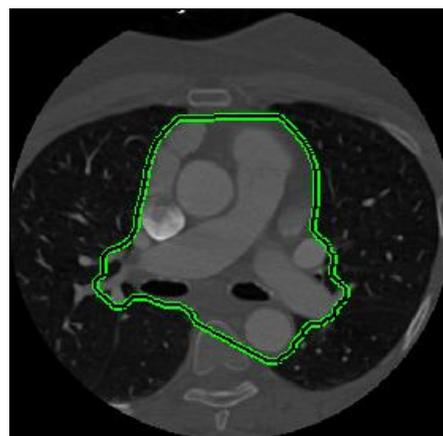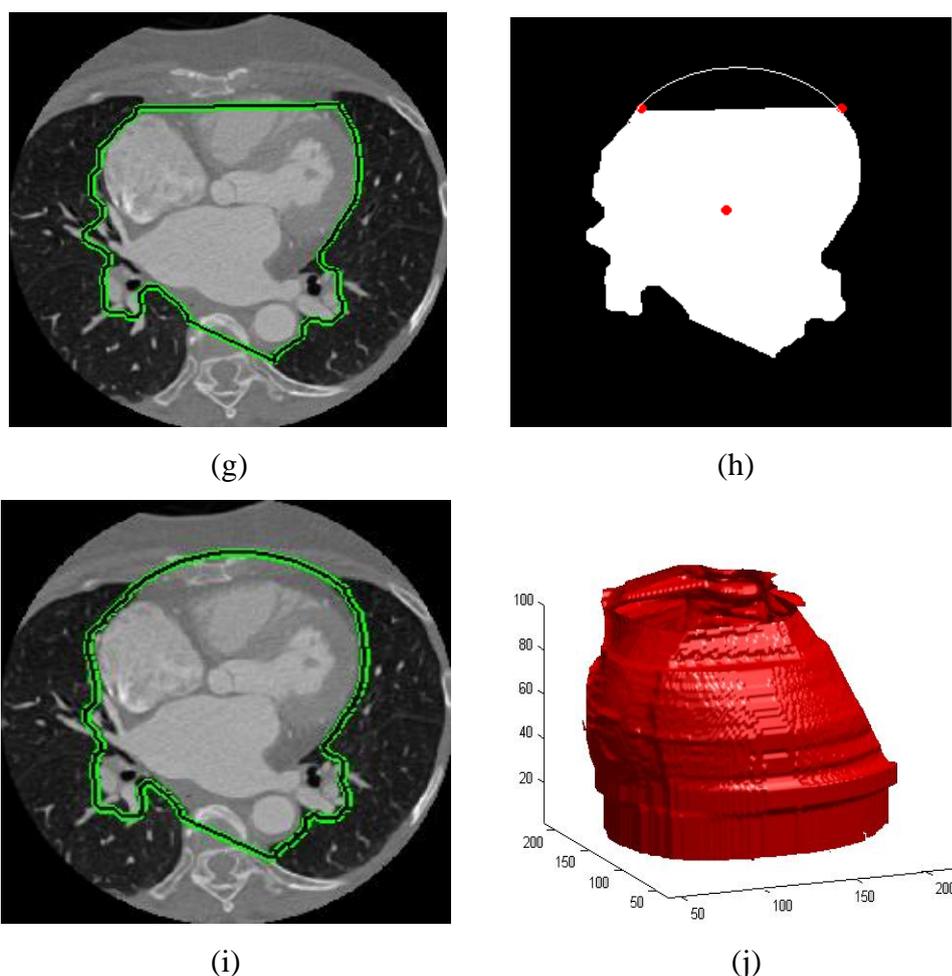
Figure 3.2: Illustration of the heart segmentation scheme: (a) An axial CT image randomly taken from the CT volume data, (b) The histogram of the image in (a), (c) The lungs extracted by thresholding, (d) Connecting the critical points, defined by red crosses, using the Bresenham line drawing algorithm, (e) The heart region, (f) The border of the heart superimposed on the original image, (g) Example of the erroneous segmentation, when using a straight line segment to enclose the anterior mediastinum, (h) The arc connecting the two top critical points and the centre of the initial estimation of the heart, shown by red dots, (i) The border of the heart region superimposed on the original image using an arc segment to enclose the anterior mediastinum, (j) 3D example of the outer surface of the heart obtained by using the proposed heart segmentation algorithm.

to incomplete segmentation of the arterial tree. To alleviate this problem, we propose using an arc, which is defined as a of portion of the circumference of a circle, determined by the two upper critical points and the centre of the initial estimation of the heart region, to enclose the anterior mediastinum (see Fig. 3.2(h)). The same procedure is repeated for every axial image of the CT volume data, which

(a)   (b)
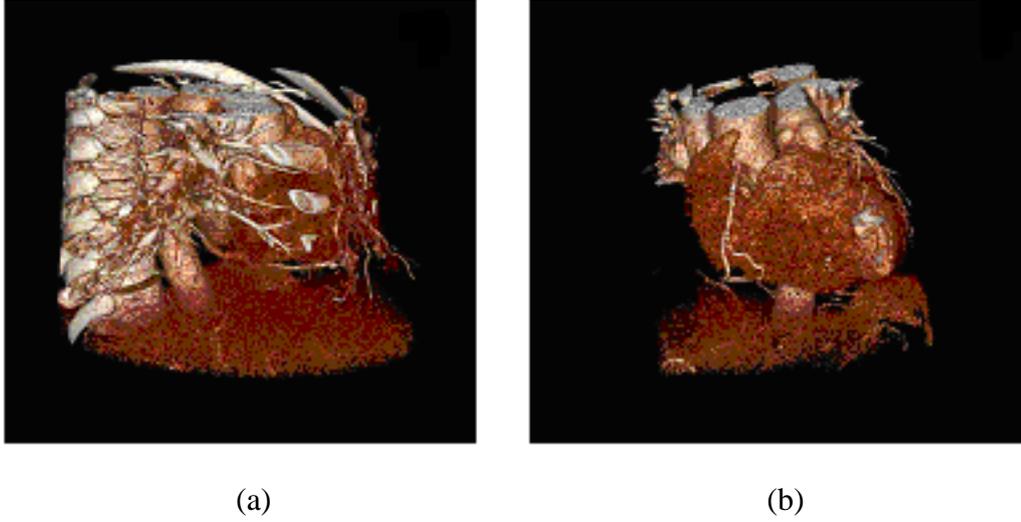
Figure 3.3: 3D volume rendered image illustrating the coronary CT data, (a) before, and (b) after the application of heart segmentation.

leads to the final heart segmentation, as depicted in Fig. 3.2(j). Fig. 3.2 shows the effect of heart segmentation by comparing the surface rendered images obtained before and after segmentation, in Figs. 3.3(a) and (b), respectively.

3.2.2 Vessel enhancement

Frangi *et al.*, filter [33] is a popular method to detect vascular structures in medical images. In this method, the norm of the Hessian matrix is used to measure the local contrast of the image. False positives, originated from bronchi and calcified regions, usually have a high local image contrast to the background, and are thus more likely to be classified as belonging to vessels. In order to eliminate these false positives, we propose a modification to the technique proposed by Frangi and his co-workers [33], where the intensity information of the voxels is taken into consideration. Specifically, we utilise a window function to select the intensity region that we are interested in (i.e., blood filled regions). To this end, we define the window function, $W(\boldsymbol{x})$, as the product of two hyperbolic tangent-sigmoid transfer functions as:

$$W(\boldsymbol{x}) = 0.5 \cdot [\tan sig(b_1 \cdot (I(\boldsymbol{x}) - T_L)) + 1] + 0.5 \cdot [1 - (\tan sig(b_2 \cdot (I(\boldsymbol{x}) - T_H)) + 1)] \quad (3.1)$$

where T_L and T_H are the low and high thresholds, determined using prior knowledge about the intensity characteristics of the blood regions, and $I(x)$ denotes the intensity level at voxel x. b_1 and b_2 are constants controlling the slope of the window. $sig(\cdot)$ is the sigmoid function. The vesselness function can be then defined as:

$$V_0(x) = \begin{cases} 0, & \text{if } \lambda_2 \text{ or } \lambda_3 > 0 \\ (1 - \exp(-\dfrac{R_A^2}{2\alpha^2}))\exp(-\dfrac{R_B^2}{2\beta^2}))(1 - \exp(-\dfrac{S^2}{2c^2}))\, W(x), & \text{otherwise} \end{cases} \quad (3.2)$$

where

$$R_A = \frac{(\text{Largest Cross Section Area})/\pi}{(\text{Largest Axis SemiLength})^2} = \frac{\lambda_1}{\sqrt{|\lambda_2 \lambda_3|}} \quad (3.3)$$

$$R_B = \frac{\text{Volume}/4\pi/3}{(\text{Largest CrossSection Area}/\pi)^{3/2}} = \frac{|\lambda_2|}{|\lambda_3|} \quad (3.4)$$

$$S = \sqrt{\lambda_1^2 + \lambda_2^2 + \lambda_3^2} \quad (3.5)$$

$V_0(x)$ denotes the vesselness measurement, obtained at pixel x. $|\lambda_1|<|\lambda_2|<|\lambda_3|$, are eigenvalues of the Hessian matrix, calculated at each pixel of the volumetric data. The term R_A is used for distinguishing between plate-like and tubular structures. It approaches zero when tubular structures are present in the image. R_B is able to discriminate blob-like structures from others, and the Hessian norm S serves as a penalty term to suppress the background noise. α, β and c are constants controlling the weights of each individual metric. Fig. 3.4 demonstrates the efficiency of the proposed vessel enhancement filter in 2D axial images, where all of the non-vascular structures are eliminated in the filtered image (see Figs. 3.4(b) and (d)). Note that, we only apply the vessel enhancement filter within the heart area defined in the previous step. We refer the reader to [31-33] and the references therein for details about Hessian based vessel enhancement techniques.

(a)   (b)

(c)   (d)
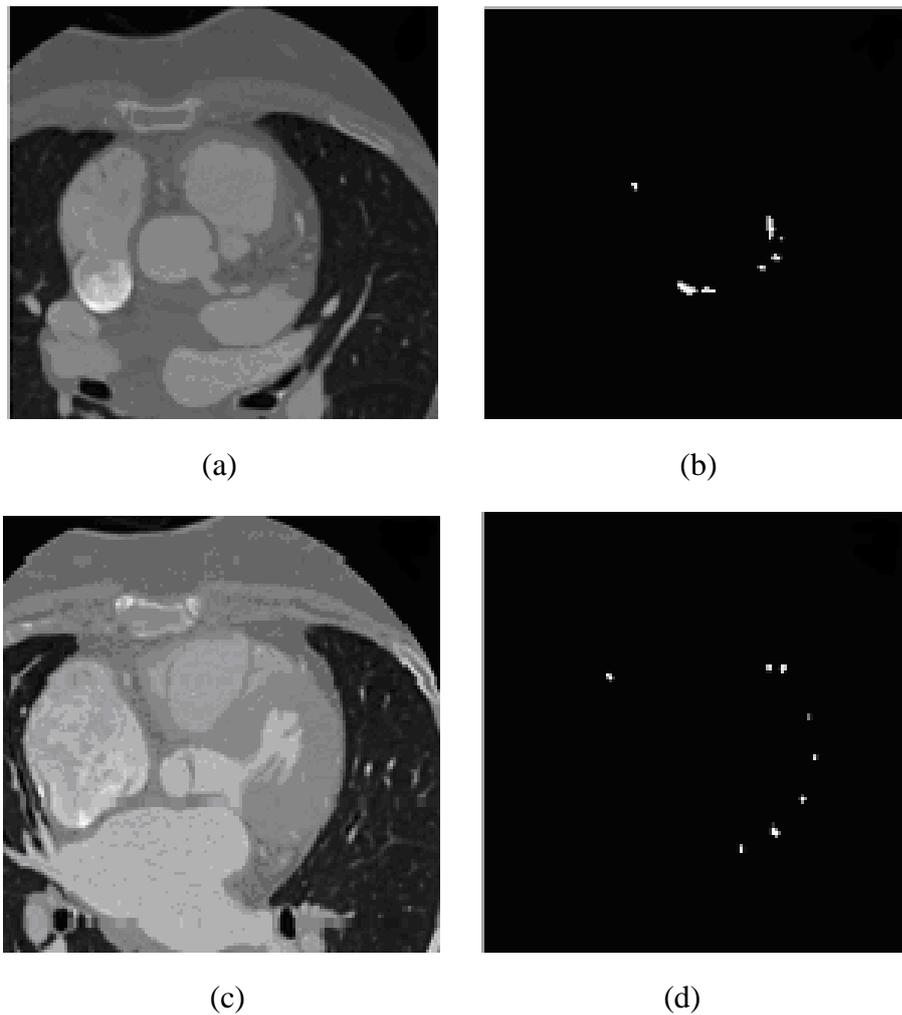
Figure 3.4: Axial images illustrate the efficiency of the vessel enhancement filter: (a) and (c) are original axial CT images randomly taken from the volume data, (c) and (d) are the corresponding filter responses.

3.2.3 Identification of the Coronary Arteries

The filter responds to each voxel of the CT image, and assigns a vesselness measurement, indicating the likelihood that such voxel belongs to the vascular structure. To create a binary representation of the coronary arteries, an adaptive thresholding algorithm is applied on the outputs of the enhancement filter. The binary image is obtained by finding the voxels with a filter response greater than 90% of the median value of its neighbourhood. To eliminate the unwanted filter responses caused by false positives such as pulmonary arteries, we only consider the filter response within the heart mask, defined in the previous section. The

resulting binary image, however, may still contain some small disconnected fragments, which do not belong to the arteries, as shown in Fig. 3.5(a). To discriminate the coronaries from these fragments, we propose the use of prior anatomical knowledge, i.e., coronaries originate from the descending aorta, to identify the coronary arteries in an automated fashion. This is achieved by finding the largest two components connecting to the aorta in the binary image. Based on the observation that the shape of the aorta is almost circular in the upper axial images through the heart (see Fig. 3.6), we firstly extract the descending aorta using the Hough transform for circle detection [135], by finding the best fitting circle within the heart region. To ensure the correct generalisation of the aorta, for each slice, the top three best fitting circles, based on their Hough transform scores, are considered as the candidates. The current segmentation of the aorta is then chosen as the candidate circle with more than 85% overlapping to the aorta, detected in the previous slice, and with the minimum distance between the centres of the circles in the current and previous slices. Once the descending aorta is segmented, the coronary arteries can be subsequently identified by finding the largest two components connecting to the aorta, as illustrated in Fig. 3.5(b).

(a) (b)
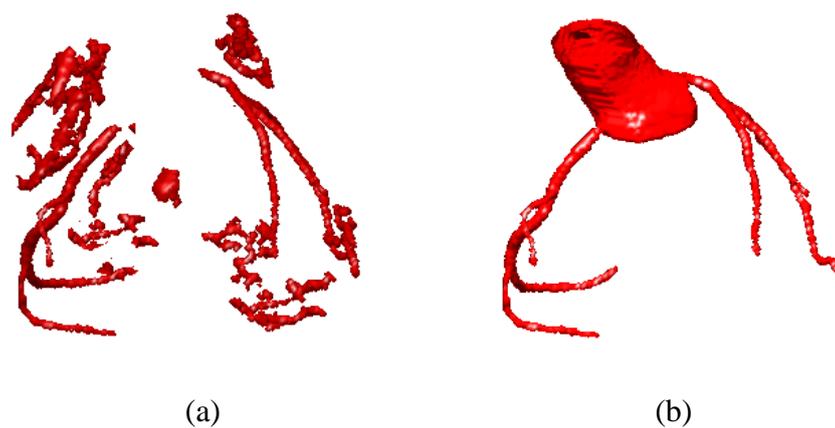
Figure 3.5: Identification of coronaries based on the response of the vessel enhancement filter: (a) The binary image of the coronaries obtained by thresholding the filter response, (b) 3D reconstructed image of the coronary arteries and part of the aorta.

(a)   (b)

(c)   (d)
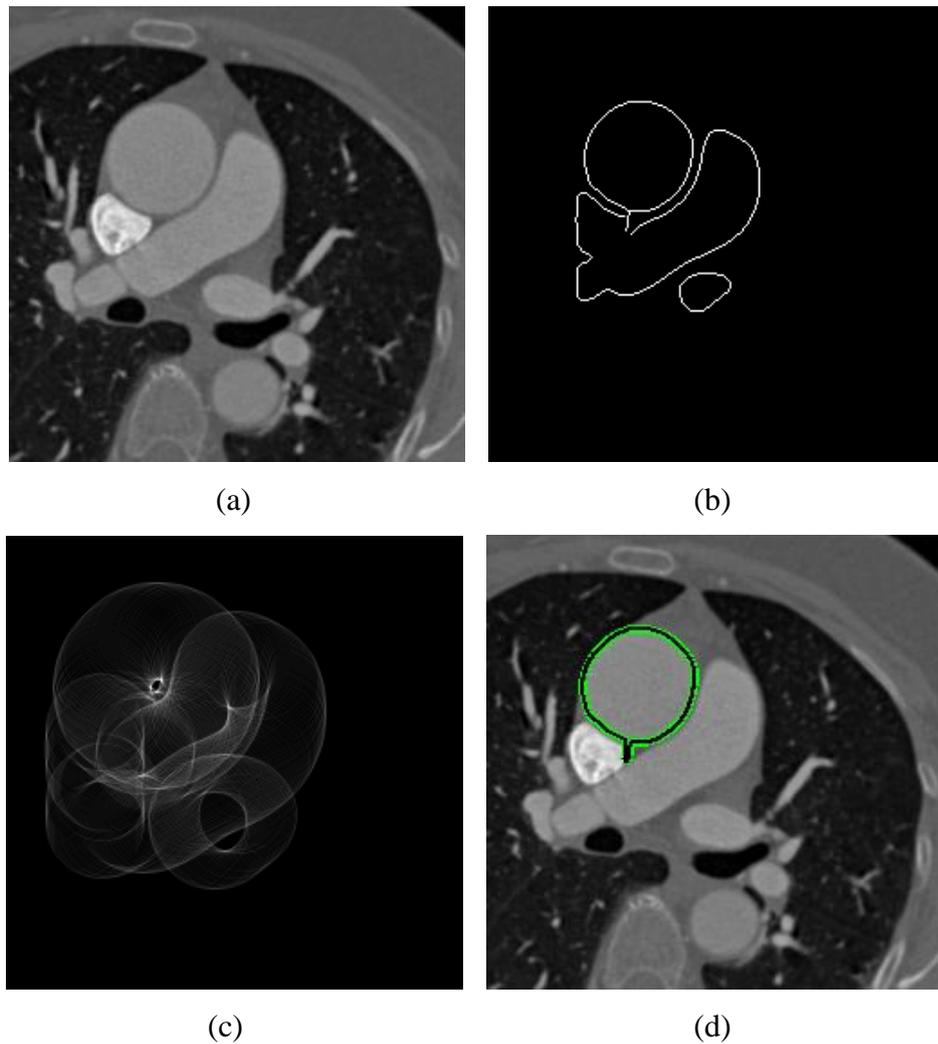
Figure 3.6: Segmentation of the aorta: (a) The original axial image randomly taken from the volume, (b) The edge map of the heart regions, (c) The accumulator space of the Hough transform for circular object detection, (d) The segmented descending aorta.

3.3 Segmentation of Coronary Arteries

In this section, we present an active contour based method for segmentation of the coronary arteries in 3D CTA images, where both global and local grey level intensity information are utilised in the energy calculation. We compute the regional statistics locally, in the neighbourhood of the active contour, to deal with varying image brightness. The global intensity information, on the other hand, is utilised to evolve the contour to the desired boundaries without being trapped in local minima. The proposed algorithm is implemented using a Bayesian probabilistic framework

to incorporate these two homogeneity constraints. Possible outliers, such as kissing vessel artifacts, are removed in the subsequent stage through a novel slice-by-slice correction scheme based on multiregion competition, where both arteries and kissing vessels are identified and tracked through the transaxial slices.

3.3.1 Modelling Global Intensities

We commence our analysis by modelling the histogram of coronary CT images using a Gaussian Mixture Model, where three Gaussian functions are used to approximate the intensity distribution of the background (i.e., air in the lungs), soft tissues and blood filled regions, respectively. The parameters for each class (i.e., the mean and variance) are determined using the Expectation Maximisation (EM) method [136] (see Fig. 3.7(a)). By utilising prior anatomical knowledge, i.e., coronaries are located on the outer surface of the heart, we neglect the class corresponding to the air to obtain a bi-modal histogram, as shown in Fig. 3.7(b). The first peak (T_1) in the fitted histogram corresponds to the soft tissues in the heart. We therefore assume that voxels with intensity values less than T_1 belong to the background, while voxels with intensity values greater than this threshold are considered as potential objects of interest (i.e., blood-filled regions).

(a)	(b)
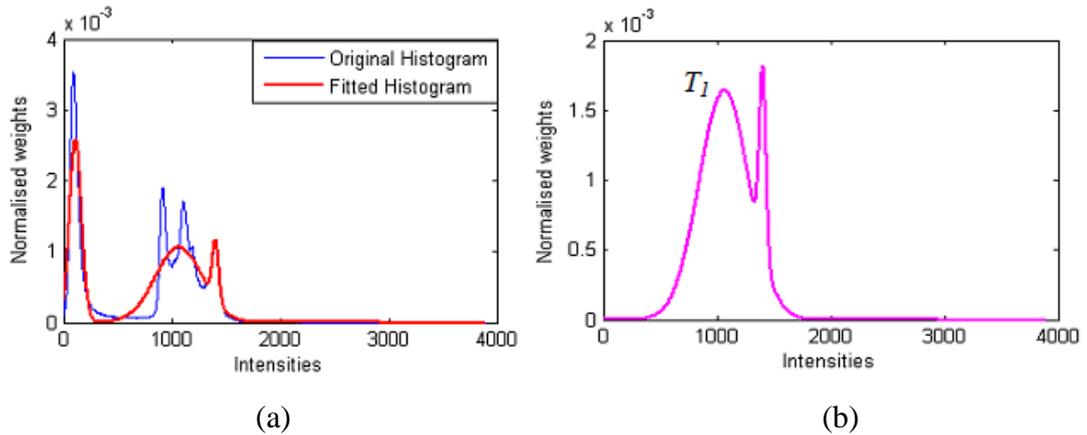
Figure 3.7: The histograms of the CTA image. (a) The histogram (blue) and the fitted mixture model (red) of the CTA image, (b) The fitted histogram within the heart region.

Based on the fitted histogram, we assign each voxel of the image with a fuzzy label, measuring the probability of the voxel belonging to the object, through the

application of a labelling function. In this research, we formulate the labelling function as a normalised cumulative density function (CDF) of the fitted histogram. The labelling function is normalised between -1 and 0 for voxels with intensity values between 0 to T_1, and we bound the output of the function between 0 and 1 for the input voxels with intensity values greater than T_1. Hence, the labelling function is defined as follows:

$$L(\boldsymbol{x}) = \begin{cases} [-1,0], & \text{if } I(\boldsymbol{x}) \leq T_1 \text{ (background)} \\ (0,1], & \text{otherwise (potential 'object')} \end{cases} \tag{3.6}$$

Fig. 3.8 illustrates the labelling result obtained through the application of the labelling function to the coronary CT image. The anisotropic diffusion filter [137] is subsequently applied to the resulting image in order to the reduce noise introduced during image acquisition.

(a)   (b)
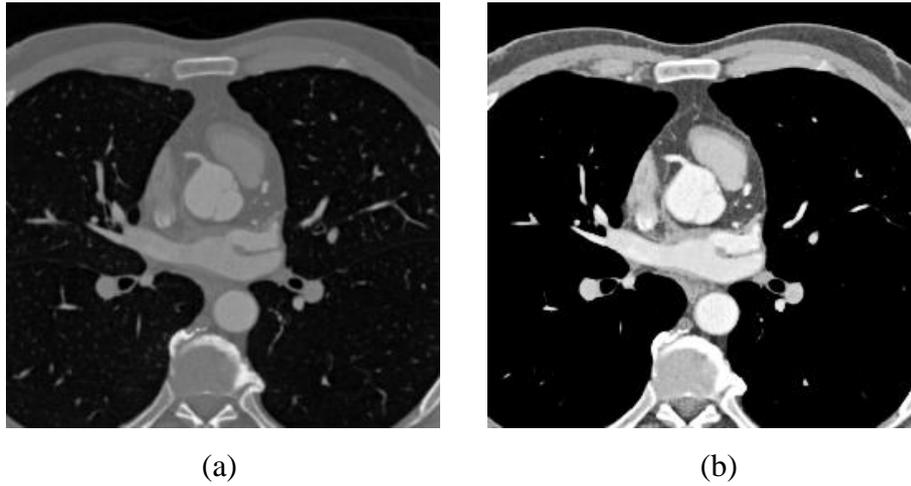
Figure 3.8: The labelling function applied to an axial CT image randomly taken from volumetric dataset. (a) The original transaxial CT image, (b) The resulting image after the application of the labelling function.

3.3.2 Modelling Local Intensities

Let $\Omega_{\boldsymbol{x}}$ denote a neighbourhood with a radius r centred at $\boldsymbol{x}$ on the active contour $C(\boldsymbol{x})$. As illustrated in Fig. 3.9, the localised image, $\Omega_{\boldsymbol{x}}$, can be partitioned into two sub-regions by the active contour, i.e., the regions inside and outside the active contour, respectively. Hence, we define the probability of a voxel being classified as belonging to the region Ω_i as follows

$$P_i = P(I(y) \mid y \in \Omega_i \cap \Omega_x) = \frac{1}{\sqrt{2\pi}\sigma_i} \exp(-\frac{(\mu_i - I(y))^2}{2\sigma_i^2}) \tag{3.7}$$

where $\{\Omega_i \mid i = 1,2\}$ denote the regions inside and outside the contour. $I(y)$ is the image intensity at y, μ_i and σ_i represent the mean and the variance derived from region Ω_i, respectively. Note that, we use x and y as two independent spatial variables to represent a single point in the image domain.

(a) (b)
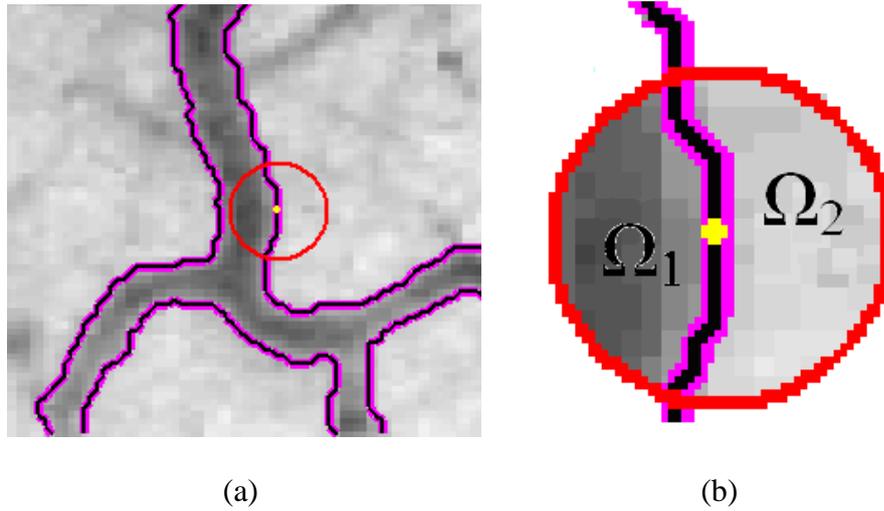
Figure 3.9: Synthetic image illustrates the localised image regions of the active contour model. (a) A point randomly chosen from the active contour. The red circle shows the circular neighbourhood around the centre point (shown in yellow), which is located in the active contour, (b) The zoomed-in image within the circle defined in (a). Note that the pixels outside of the circle are ignored.

As previously discussed in Chapter 2, global statistics are robust to local spurious features, while localised information enables dealing with varying brightness in the image. In order to incorporate their advantages, the labelling function is designed to be a normalised CDF of the fitted histogram, rather than the PDF as defined in the work of Yang *et al.*, [88]. By doing so, the distal segments of the arteries, usually exhibiting relatively lower intensities and with less contrast to the background, would be assigned with labels which are close to zero (i.e., $|L(x)| \to 0$). In these regions, the global term will contribute less to the overall energy functional, and thus, the contour will evolve mainly based on the local energy information. On the other hand, when the contour is located in the homogenous regions or unwanted

local minima, the global energy is able to provide additional force to drive the front to evolve away from these stationary points.

3.3.3 Active Contour Energy and Level Set Formulation

In this section, we incorporate the two aforementioned energy terms using a probabilistic framework. Consider a contour, $C(x)$, representing the boundary of the object to be segmented. For each point along the contour, given its local image Ω_x and the labelling function $L(y)$, the posterior probability of a voxel y being classified as belonging to the sub-region $\Omega_i \cap \Omega_x$ can be defined as:

$$P(y \in \Omega_i \cap \Omega_x \mid I(y), L(y)) = \frac{P(I(y), L(y) \mid y \in \Omega_i \cap \Omega_x) P(y \in \Omega_i \cap \Omega_x)}{P(I(y), L(y))} \tag{3.8}$$

where $P(y \in \Omega_i \cap \Omega_x)$ is the prior probability of the current voxel being assigned to region Ω_i among all the possible partitions within the local image Ω_x. This term can be ignored, if equal probabilities are assumed for all partitions of the image. $P(I(y), L(y))$ denotes the joint probability density distribution of the grey level value $I(y)$ and the labelling function $L(y)$, which is independent of the segmentation of the image and can therefore be neglected. We assume that the voxel labels and the grey level intensity distribution are independent. The posterior probability for each voxel can thus be computed as:

$$P(I(y), L(y) \mid y \in \Omega_i \cap \Omega_x) = P(I(y) \mid y \in \Omega_i \cap \Omega_x) P(L(y) \mid y \in \Omega_i \cap \Omega_x) \tag{3.9}$$

The prior probability of $P(I(y) \mid y \in \Omega_i \cap \Omega_x)$ has been already defined in Eq. (3.7). In order to compute the posterior probabilities in Eq. (3.8), the prior probability of the labelling function should be known. In this research, we model the prior probability distribution of the labels as:

$$P(L(y) \mid y \in \Omega_i \cap \Omega_x) \propto \exp(\frac{v}{2} L(y) R(x) k_\sigma(x, y)) \tag{3.10}$$

where

$$k_\sigma(x, y) = \frac{1}{\sqrt{2\pi}\sigma} \exp(-\frac{(x-y))^2}{2\sigma^2}) \tag{3.11}$$

represents the weighting kernel, which is a decaying function of the distance between x and y. v is the overall weight, which determines the influence of the labels on the segmentation, $R(x)$ is a normalised Boolean function indicating whether the current voxel x is located inside the contour $C(x)$ within the local image Ω_x.

$$R(x) = \begin{cases} -1, & \text{if } x \in \Omega_2 \text{ (outside the contour)} \\ +1, & \text{if } x \in \Omega_1 \text{ (inside the contour)} \end{cases} \tag{3.12}$$

According to Eq. (3.10), when a voxel, located at position x, is classified as belonging to the object, i.e., $R(x) = 1$, then a point y in its vicinity has a higher probability of being marked as belonging to the object (i.e., $L(y) \to 1$) and is less likely to be considered as the background ($L(y) \to -1$).

Maximising the posterior probability in Eq. (3.8) is equivalent to minimising its negative logarithm. Hence, for each given point x belonging to the contour $C(x)$, the image-based energy can be defined as:

$$
\begin{aligned}
E_x &= -\sum_{i=1}^{2} \int_{\Omega_i \cap \Omega_x} \log P(y \in \Omega_i \cap \Omega_x \mid I(y), L(y)) dy \\
&= -\sum_{i=1}^{2} \int_{\Omega_i \cap \Omega_x} \log P(I(y), L(y) \mid y \in \Omega_i \cap \Omega_x) dy \\
&= -\sum_{i=1}^{2} \left(\int_{\Omega_i \cap \Omega_x} \log P(I(y) \mid y \in \Omega_i \cap \Omega_x) dy + \int_{\Omega_i \cap \Omega_x} \log P(L(y) \mid y \in \Omega_i \cap \Omega_x) dy \right)
\end{aligned}
\tag{3.13}
$$

The prior probabilities, i.e., $P(I(y)|y \in \Omega_i \cap \Omega_x)$ and $P(L(y)|y \in \Omega_i \cap \Omega_x)$, were defined in Eqs. (3.7) and (3.10), respectively.

To achieve the active contour segmentation, we need to define a contour $C(x)$ that minimises the energy E_x along the contour over the image domain, which is equivalent to finding the minimum energy of the integral of E_x in the image. In level sets methods [86], a contour is usually represented as the embedding zero level set of a higher dimensional signed distance function ϕ (known as the level set function). We assume that the function takes positive values in the interior of the

contour, and is negative for regions outside of the zero level set. We denote $H(\cdot)$ to be the Heaviside function, and then the active contour energy can be formulated as:

$$
\begin{aligned}
E = -\int H'(\phi(\boldsymbol{x})) \sum_{i=1}^{2} \{ & \int_{\Omega_i \cap \Omega_x} [\log P(I(\boldsymbol{y}) \mid \boldsymbol{y} \in \Omega_i \cap \Omega_x) \\
& + \log P(L(\boldsymbol{y}) \mid \boldsymbol{y} \in \Omega_i \cap \Omega_x) d\boldsymbol{y}] M_i(\phi(\boldsymbol{y})) \} dx \\
& + \mu \int |\nabla H(\phi(\boldsymbol{x}))| dx
\end{aligned}
\tag{3.14}
$$

where $M_1(\phi(\boldsymbol{y}))=H(\phi)$ and $M_2(\phi(\boldsymbol{y}))=1-H(\phi)$, and $H'(\cdot)$ denotes the derivative of Heaviside function. The first term in the right hand side of Eq. (3.14) is the negative logarithm posterior probability defined in Eq. (3.8), which is minimised when the active contour is located at the desired boundaries. The second term estimates the length of the zero level contour of the level set function, which enforces smoothness in the resulting contour. The constant μ controls the contribution of this smoothness term in the entire active contour functional. The associated Euler-Lagrange equation is defined as:

$$
\frac{\partial \phi}{\partial t} = \delta(\phi)(\mu \, div(\frac{\nabla \phi}{|\nabla \phi|}) + \log \frac{p_1}{p_2} + v \int L(\boldsymbol{x}) k_\sigma(\boldsymbol{x}, \boldsymbol{y}) d\boldsymbol{y})
\tag{3.15}
$$

where

$$
\begin{aligned}
p_1 &= \int_{\Omega_1 \cap \Omega_x} \frac{1}{\sqrt{2\pi}\sigma_1} \exp(-\frac{(\mu_1(\boldsymbol{x})-I(\boldsymbol{y}))^2}{2\sigma_1^2(\boldsymbol{x})}) d\boldsymbol{y} \\
p_2 &= \int_{\Omega_2 \cap \Omega_x} \frac{1}{\sqrt{2\pi}\sigma_2} \exp(-\frac{(\mu_2(\boldsymbol{x})-I(\boldsymbol{y}))^2}{2\sigma_2^2(\boldsymbol{x})}) d\boldsymbol{y}
\end{aligned}
\tag{3.16}
$$

p_1 and p_2 represent the prior probability density distribution of the object and background, respectively. $\delta(\cdot)$ denotes the Dirac delta function, which is defined as the derivative of Heaviside function $H(\cdot)$. The evolution equation defined in Eq. (3.15) can be solved numerically using the gradient descent algorithm as:

$$\phi^{(n+1)}(\boldsymbol{x}) = \phi^{(n)}(\boldsymbol{x}) + \Delta t[\mu \cdot \kappa + \log \frac{\sum\limits_{y \in \Omega_1 \cap \Omega_x} \frac{1}{\sqrt{2\pi}\sigma_1} \exp(-\frac{(\mu_1(\boldsymbol{x}) - I(\boldsymbol{y}))^2}{2\sigma_1^2(\boldsymbol{x})}}{\sum\limits_{y \in \Omega_2 \cap \Omega_x} \frac{1}{\sqrt{2\pi}\sigma_2} \exp(-\frac{(\mu_2(\boldsymbol{x}) - I(\boldsymbol{y}))^2}{2\sigma_2^2(\boldsymbol{x})}} \tag{3.17}$$

$$+ \nu \sum_{y \in \Omega_x} L(\boldsymbol{y}) k(\boldsymbol{x}, \boldsymbol{y})]$$

where κ denotes the curvature of the level set function at position $\boldsymbol{x}$ and given as follows:

$$\kappa = \frac{\sqrt{(z''y' - y''z')^2 + (x''z' - z''x')^2 + (y''x' - x''y')^2}}{(x'^2 + y'^2 + z'^2)^{3/2}} \tag{3.18}$$

x', y' and z' represent the first order partial derivatives of the level set function, ϕ, along x, y and z direction, respectively, while x'', y'' and z'' denote the second order partial derivatives along the three orthogonal axes. The partial derivatives at each point of the level set function are approximated using central differences. To keep the computational cost at an appropriate level, we only update the level set function near the zero level set within a narrow band [138]. The level set function was periodically re-initialised in order to maintain it as the signed distance function [86]. The step size, Δt, in the evolution equation, defined in Eq. (3.17) is constrained by the Courant-Fridreiches-Lewy (CFL) condition to ensure the numerical stability of the solution [86].

3.3.4 Kissing Vessel artifacts Suppression

The segmentation results obtained in the first stage of processing are nearly optimal. However, due to the complexity of medical images and the associated artifacts, the resulting images may contain some outliers, such as kissing vessels (see Fig. 3.10). In order to remove these erroneous segments, a slice-by-slice correction scheme is applied to the resulting images obtained in the first stage of the segmentation. As it can be observed in the zoomed image in Fig. 3.10(b), the non-arterial vessel appears darker than the coronary artery, and thus, it can be potentially segmented through a multiregion competition based method. As reported by Brox

(a)   (b)
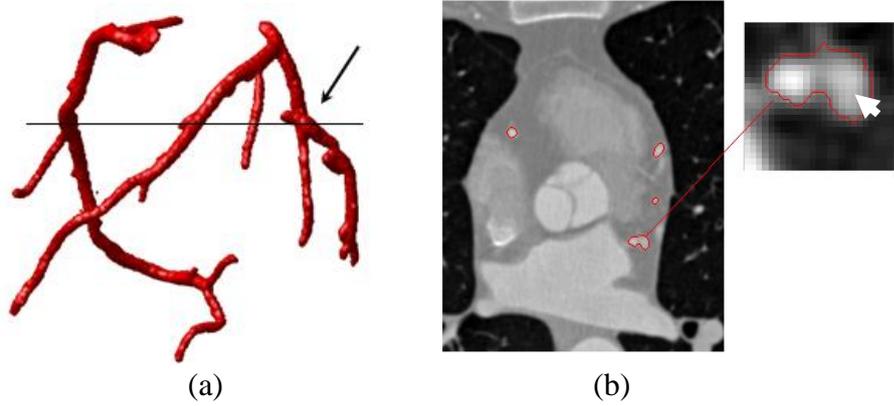
Figure 3.10: Illustration of 'kissing vessel' artifacts present in coronary CT images. (a) 3D surface reconstruction of the coronary arteries with a touching non-arterial vessel (shown by the arrow), (b) The cross sectional image taken from the volume, and the close up image of the outlier vessel. The cross sectional segment of the non-arterial vessel (shown by the arrow) appears darker than the artery.

and his co-worker [139], for a fixed number of objects to be segmented, the evolution equations of multiple region level sets for image segmentation can be represented as:

$$\frac{\partial E(\phi_i)}{\partial t} = H'(\phi_i)(e_i - \max_{\substack{H'(\phi_j)>0 \\ j \neq i}}(e_j, e_i - 1))$$

$$e_k = \log p_k + \frac{\mu}{2} div(\frac{\nabla \phi_k}{|\nabla \phi_k|})$$

(3.19)

where ϕ_i is associated with the *i*-th level set function defining the object, and e_k denotes the internal energy derived from the image regions described by ϕ_k. The probability density function, p_k, is defined based on regions within the interior of *k*-th level sets function, and μ is a constant controlling the smoothness of the contour. The term $(e_i - 1)$ in the maximum operator ensures that the contour expands outwards with a constant speed, when there is no competition around the zero level set of the current embedding function, making the contour move far away from its initial position and often approaching undesired boundaries. To address this issue, we propose a modification to Brox and Weickert's evolution scheme [139], where the active contour moves according to the following:

$$\frac{\partial \phi_i(x)}{\partial t} = \delta \phi_i(x) \{ \max_{\substack{H'(\phi_i)>0 \\ i \neq j}} (e_{i,1}, e_{j,2}) - \max_{\substack{H'(\phi_i)>0 \\ i \neq j}} (e_{i,2}, e_{j,1}) \}$$

$$e_{k,1} = \log p_{k,1} + \frac{\mu}{2} div(\frac{\nabla \phi_k}{|\nabla \phi_k|})$$

$$e_{k,2} = \log p_{k,1} + \frac{\mu}{2} div(\frac{\nabla \phi_k}{|\nabla \phi_k|})$$

(3.20)

where $e_{k,1}$ and $e_{k,2}$ represent the energy derived from the regions within the interior and exterior of k-th level set, respectively. $P_{k,i}$ denotes the posterior probability of a voxel, **x**, being classified as belonging to image region $\Omega_i \cap \Omega_\mathbf{x}$ by the **k**-th level set function, defined previously in Eq. (3.8). In terms of Eq. (3.20), the active contour will evolve according to two-phase energy, when there is no competition nearby. When multiple contours are presented in an interface, the points in the interface would move together, subject to the strongest force across all the regions.
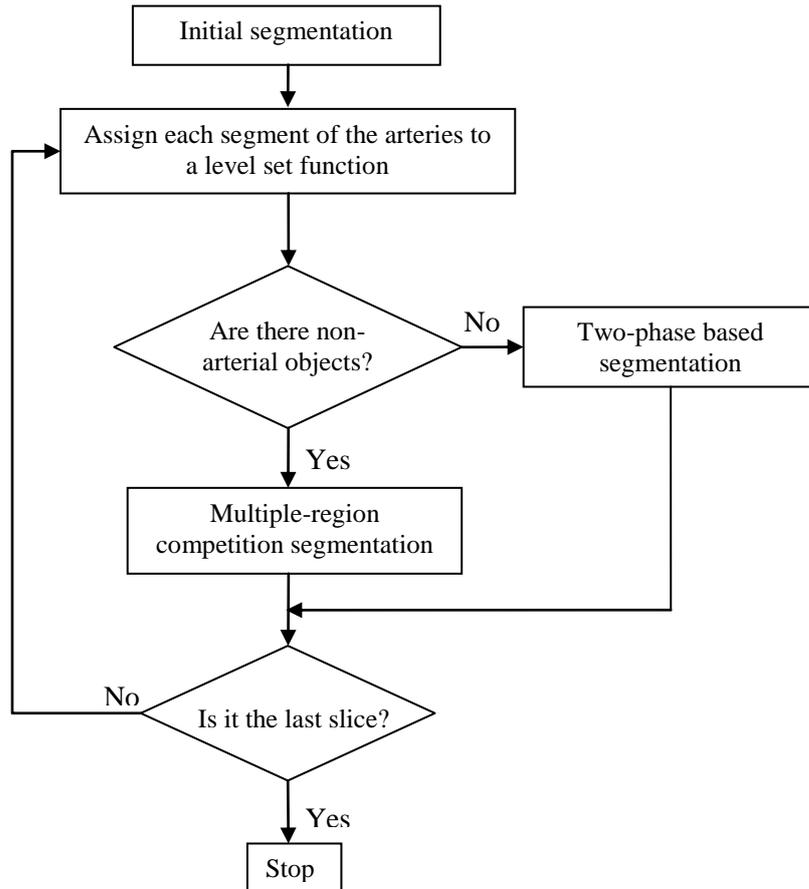
Figure 3.11: Flow-chart of the proposed slice-by-slice correction scheme for suppression of kissing vessel artifacts.

To identify kissing vessels and remove them from the first stage segmentation, we assume that the coronary arteries can be modelled as a tree structure, and the transaxial cross sectional segments of the artery taken from the top to the bottom can only split but not merge over the transaxial images. The flow chart of the proposed kissing vessels correction algorithm is shown in Fig. 3.11. The procedure begins by finding the first slice that contains the coronary artery. Next, the axial segment of the artery is extracted, which is then tracked through the slices. For each new slice, we compare the segmentation obtained in the first stage against the tracked artery. If there is a component that does not touch any known segments of the tracked artery, then the object is considered as a kissing vessel structure, and a level set is assigned to it. In the following step, both of these two vessels are evolved and tracked. We repeat this process until the last slice containing the artery is reached.

3.4 Experiments and Discussion

In this section, we apply the proposed method to various 2D and 3D synthetic and real images and analyse its efficiency. In section 3.3.1, we firstly compare the proposed method with active contour models based on using global (Yang *et al.*, [88]) and local (localised Chan-Vese (CV) model [105]) information alone, to demonstrate the benefits offered by using both local and global statistics based on 2D synthetic images. Then, we validate the proposed method in 3D CTA images and compare our method with the active contour model proposed by Yang *et al.*, in Section 3.3.2. The tuning parameters of the proposed technique were empirically determined and fixed throughout this experiment. In particular, we chose the smoothness weight μ at 0.2, and the global energy factor v was set to 0.4. The radius of the localised image r was selected based on prior information regarding the size of the vessels to be segmented, which equals the maximum radius of the vessel of interest.

3.4.1 Experiments on Synthetic Images

To quantify the performance of the resulting segmentation, four metrics were used to validate the results, specifically:

$$TP = \frac{N_B \cap N_R}{N_R}, \quad FN = \frac{N_R - N_B \cap N_R}{N_R}$$
$$FP = \frac{N_B - N_B \cap N_R}{N_R}, OM = 2 \cdot \frac{N_B \cap N_R}{N_B + N_R} \tag{3.21}$$

where the ground truth N_R is a binary image with voxels labelled to one for the object and zero for others, N_B indicates the pixels/voxels, which are segmented as the object by the aforementioned algorithms. TP, FN and FP denote the true positive, false negative and false positive metrics, respectively. OM represents the overlapping metric defined in [140], which is close to 1, when the segmentation is well matched to the reference ground truth and approaches zero when the results have no similarity to the reference.

We commence our analysis with a simple binary image, which is distorted by additive Gaussian noise as shown in Fig. 3.12(a). The size of the synthetic image is 181×125 pixels. In Fig. 3.12 and Table 3.1, we present the segmentation results obtained through the application of the previously reported methods and the proposed technique to this synthetic image. Contour initialisation is shown in Fig. 3.12(a). The result obtained using the active contour model reported by Yang *et al.*, is depicted in Fig. 3.12(b). In Figs. 3.12(c) and (d), we illustrate the results obtained through the use of the localised CV model and the proposed algorithm, respectively. By and large, all of the techniques enable the correct segmentation of the vascular structure in this synthetic image, although the performance of the Yang *et al.*, algorithm, in terms of the TP rate and OM metric (see Table 3.1), is slightly inferior to others. This is because the image-driven energy in their method is smoothed by anisotropic diffusion, which blurs the boundaries of the object to be segmented, thus leading to erroneous classifications along the borders of the vessel.

Table 3.1: Comparison of the 2D synthetic image segmentation results for various methods (For Fig. 3.12).

Rate (%)	Yang *et al.*, Method	Localised CV	Proposed Method
TP	93.6	96.7	97.6
FN	6.43	3.30	2.43
FP	4.41	0.170	0.100
OM	94.5	98.2	98.7
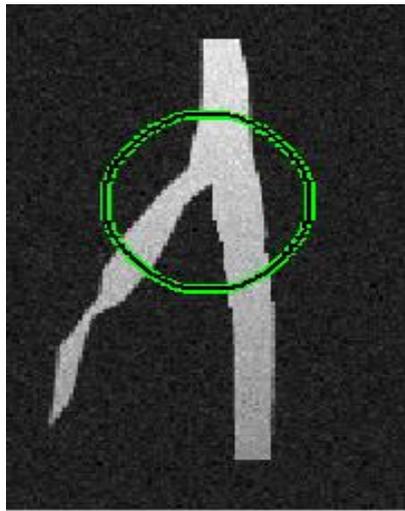
(a)
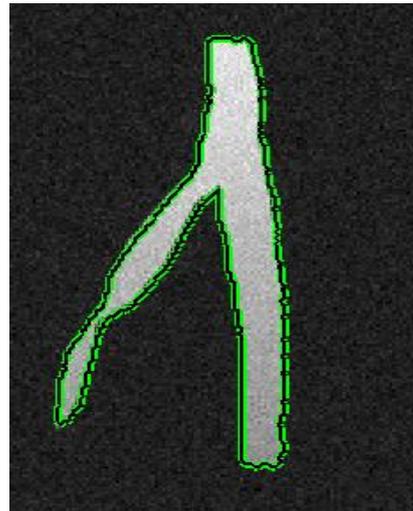
(b)
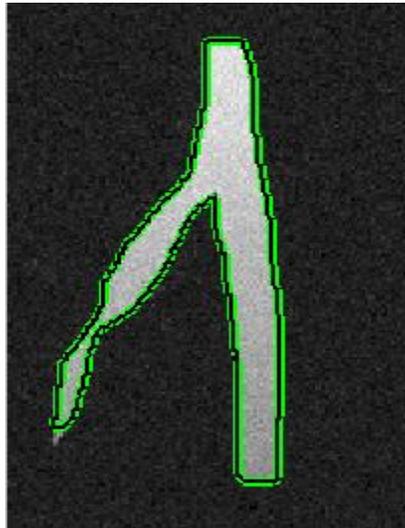
(c)
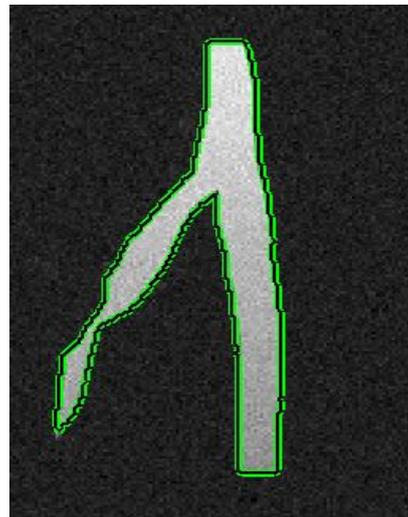
(d)

Figure 3.12: Segmentation results on 2D binary synthetic image. (a) Contour Initialisation, (b) Results obtained using Yang *et al.*, method, (c) and (d) Illustration of the segmentation results from the localised CV model and the proposed algorithm, respectively.

Table 3.2: Comparison of the 2D synthetic image segmentation results for various methods (For Fig. 3.13).

Rate	Yang *et al.*, Method	Localised CV	Proposed Method
TP (%)	76.0	95.8	97.6
FN (%)	24.0	4.21	2.40
FP (%)	3.86	0.14	0.100
OM	0.845	0.978	0.987

(a)　　　　　　　　　　　　　(b)

(c)　　　　　　　　　　　　　(d)
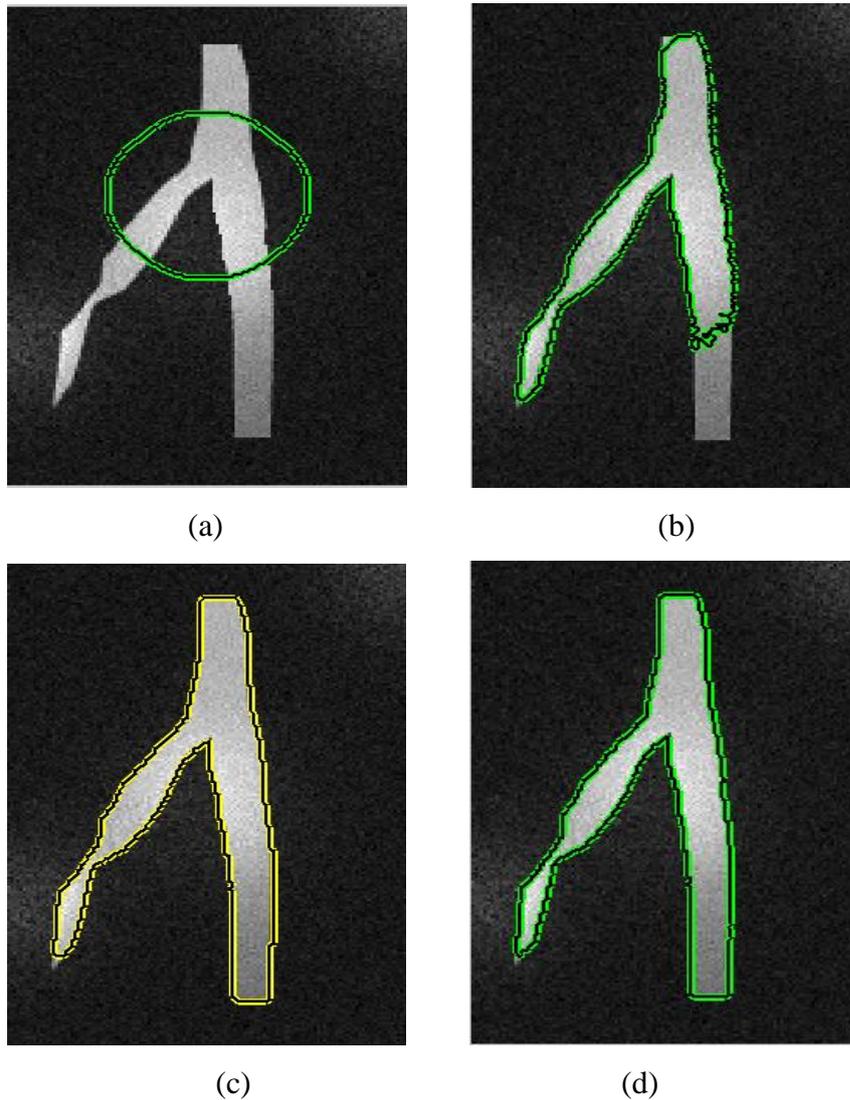
Figure 3.13: Segmentation results on 2D synthetic images under uneven brightness conditions. (a) Initialisation, (b) Results of Yang *et al.*, method, (c) Localised CV model results, (d) Proposed algorithm results.

In Fig. 3.13, we present the comparison of the segmentation results obtained from aforementioned methods with respect to the ground true data, under changing brightness conditions. Contour initialisation is shown in Fig. 3.13 (a). Fig. 3.13 (b) shows the resulting segmentation obtained by the method of Yang *et al*., Figs. 3.13(c) and (d) depict the results obtained using the localised CV model and the proposed technique, respectively. In the presence of uneven brightness conditions, Yang *et al*., approach performs less well than the other two methods, which utilise local intensity information in the energy calculation. It fails to extract the entire vasculature even when the initial contour is placed close to the final solution. The quantitative validation of these results can be found in Table 3.2, the TP rate and OM metric of Yang *et al*., algorithm are found to be 76.0% and 0.845, respectively, indicating that their model under-segments the object. On the contrary, both the localised CV model and the proposed technique are able to achieve satisfactory segmentations.

Fig. 3.14 shows another synthetic image consisting of two elongated objects with distinct intensity distributions, at close proximity to each other. Similarly, Gaussian noise was added to the image for a simplified approximation of the noise model in CT images [141]. In this experiment, we will use this image as an example to demonstrate the benefits offered by considering both local and global intensity features. The proposed method begins with the analysis of the histogram for the entire image. As it is shown in Fig. 3.14(b), the highest peak in the histogram corresponds to the background pixels, which are associated with high intensity values. Since these pixels can be discriminated by simple thresholding, we therefore neglect them in order to more precisely approximate the intensity distribution of the remaining objects, using the Gaussian mixture model (see Fig. 3.15(a)). In this experiment, the number of Gaussian functions used to model the histogram is automatically determined by increasing the number of Gaussians until the fitting error is minimised.

(a)   (b)
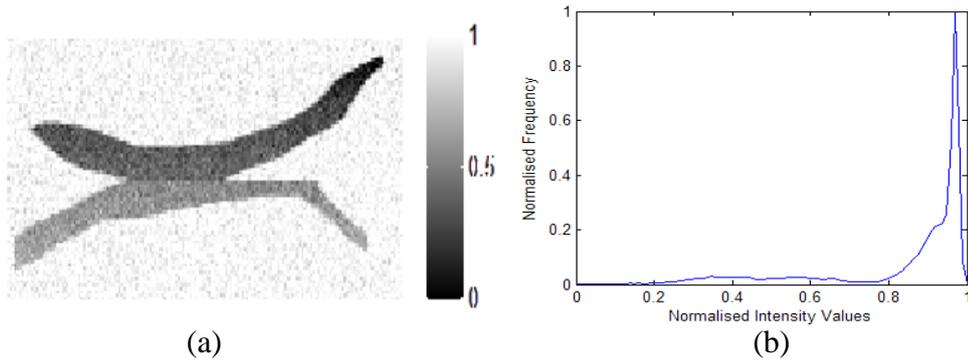
Figure 3.14: A synthetic image to evaluate the efficiency of the proposed method. (a) Illustration of the synthetic image, and (b) Normalised histogram distribution.

(a)   (b)
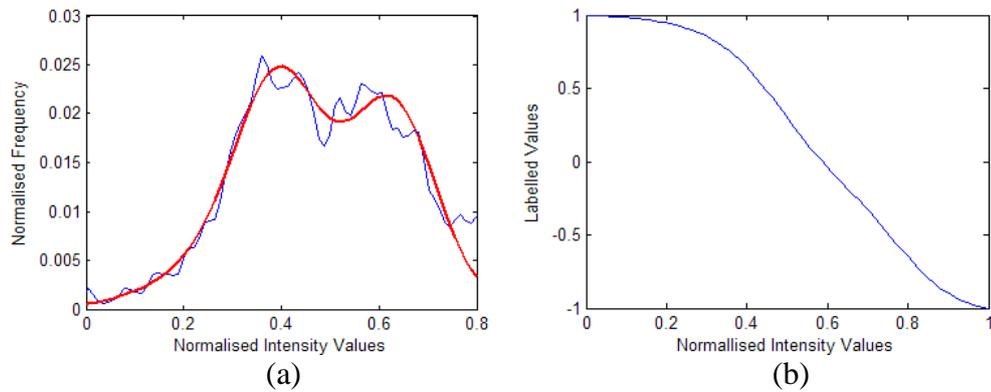
Figure 3.15: An example of fitting the histogram of Fig. 3.14(b) and defining the labelling function. (a) The histogram of the potential objects (shown in blue) and the fitted histogram (depicted in red), and (b) The labelling function obtained based on the fitted histogram.

(a)   (b)
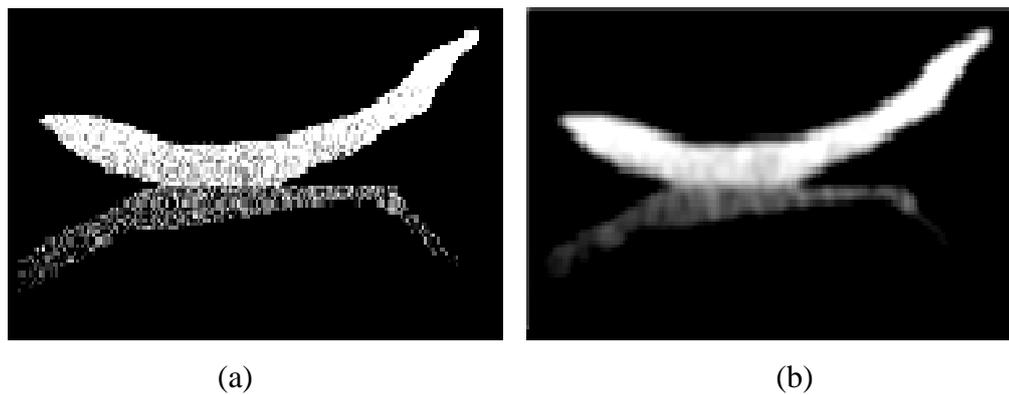
Figure 3.16: Illustration of the global energy map. (a) The labelled image, (b) The smoothed labelled map following anisotropic diffusion.

As depicted in Fig. 3.15(a), the fitted histogram has two peaks, which reflect the intensity distribution of the two objects. If we seek to extract the darker object, i.e., the one with the lower intensities, the labelling function should be formulated as a monotonically decreasing function based on the fitted histogram and normalised in the range between -1 and 1, which is shown in Fig. 3.15(b). The resulting labelled image is shown in Fig. 3.16(a), and we employ an anisotropic diffusion filter to further reduce noise, as illustrated in Fig. 3.16(b).

Table 3.3: Comparison of the 2D synthetic image segmentation results for various methods (For Fig. 3.17).

Rate	Yang *et al.*,	Localised CV	Proposed Method
TP (%)	95.0	95.9	94.6
FN (%)	5.04	4.59	5.39
FP (%)	103	27.9	4.43
OM	0.636	0.857	0.951

(a)

(b)

(c)

(d)
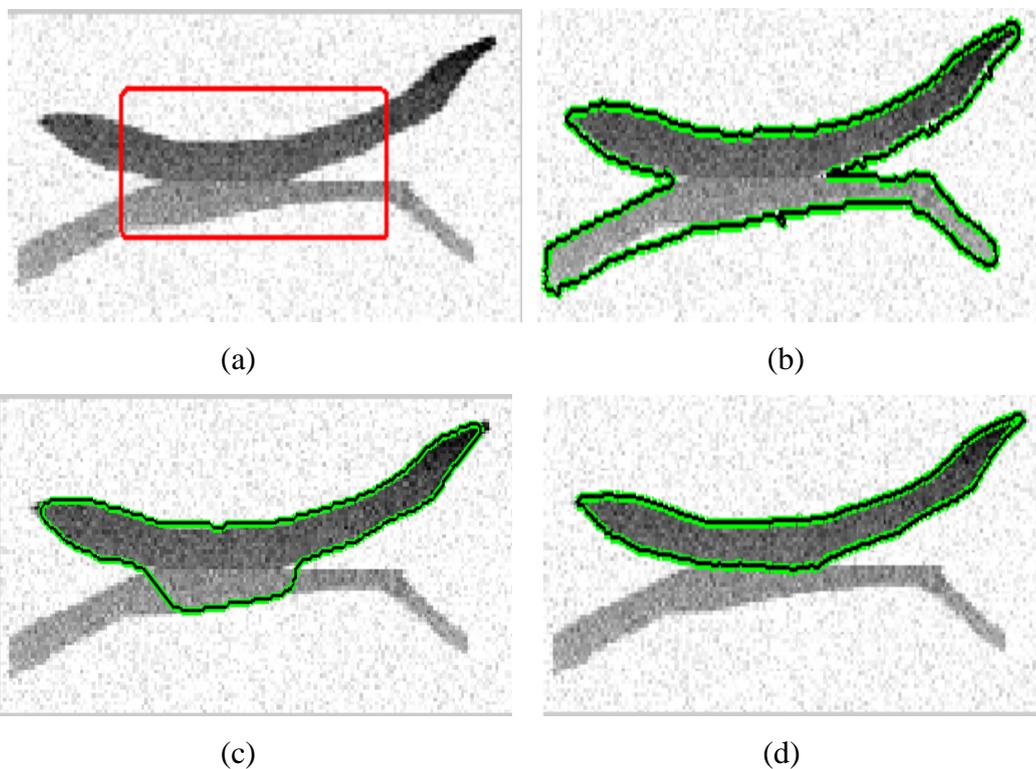
Figure 3.17: Comparison of the segmentation results obtained using the Yang *et al.*, model, the localised CV method and the proposed algorithm. (a) Initialisation, (b) Yang *et al.*, model results, (c) Localised CV method results, (d) Results of the proposed algorithm.

In Fig. 3.17, we present the segmentation results obtained using the previously reported algorithms and the proposed method for this 2D synthetic image. Contour initialisation is shown in Fig. 3.17(a). Fig. 3.17(b) shows that the Yang *et al.*, model, based on global intensity information alone, segments the two objects as a whole. The localised CV method achieves a better segmentation result. However, as illustrated in Fig. 3.17(c), there are regions that have been incorrectly segmented. By contrast, the proposed technique, using both global and local intensity information, achieves satisfactory results, which is shown in Fig 3.17(d). The quantitative validation of these results is shown in Table 3.3. It can be seen that the TP rate of the proposed method is slightly lower than the other two models. This is due to the fact that both of these methods over-segment the object, where more pixels are classified as belonging to the object, thus resulting in a higher TP rate. However, in terms of the FP and OM metrics, the overall performance of the proposed technique is superior.

3.4.2 Experiments on Real Clinical Images

Twelve coronary CT volumes were acquired from St Thomas' and Guys' Hospitals, London, UK. Two of them were obtained with a 16-slice CT scanner (Brilliance, Philips), and the remaining volumes were acquired with a Philips ICT-256 workstation. The mean size of the images is $512 \times 512 \times 286$ with an average in-plane resolution of 0.40 mm $\times$ 0.40 mm, and the mean voxel size in the z-axis is 0.42 mm.

The ground truth data were obtained through manual delineation with the assistance of interactive software, developed in our centre. To construct the ground truth data, the CT volume was firstly resampled as a successive cross sections, which is perpendicular to the course of the arteries, as shown in Fig. 3.18. Then, the luminal area was manually annotated by trained biomedical engineering research students (see Fig. 3.19(a)). The software will fit the manually delineated curve to a circle by solving the associated least squares problem (see Fig. 3.19(b)). The software then records the coordinates of the centre and the associated radius. In order to ensure the correct generation of the ground truth data, the luminal area of

the artery is required to be specified by the observer at least every 3mm. By doing so, the ground truth data for each major branch of the arterial tree contains on average 48 central axis points and the associated radii, which takes approximately half an hour to complete. Next, the centreline points were uniformly resampled with a distance at 0.05mm (roughly 0.1 voxel), and the associated radii were determined via linear interpolation. To construct a closed surface of the ground truth data, we firstly generate the boundary points of the artery based on the centreline and radius information, which is depicted in Fig. 3.20(a). Then, the outer surface of the artery can be reconstructed using the ball pivoting algorithm, as illustrated in Fig. 3.20(b).

(a)   (b)
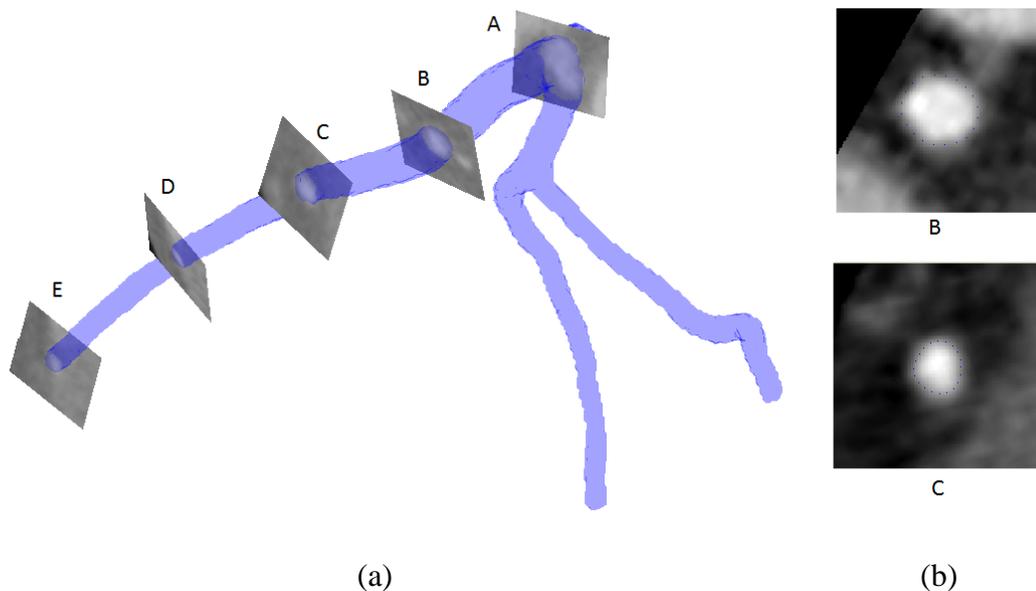
Figure 3.18: Illustration of the re-sampled cross sectional images of the CTA data for the construction of the ground truth data. (a) The segmented coronary artery is represented as 3D surface (semi transparent structure), (b) Cross sectional images of the artery, obtained by slicing the volume data using the planes perpendicular to the orientation of the vessel.

(a)	(b)
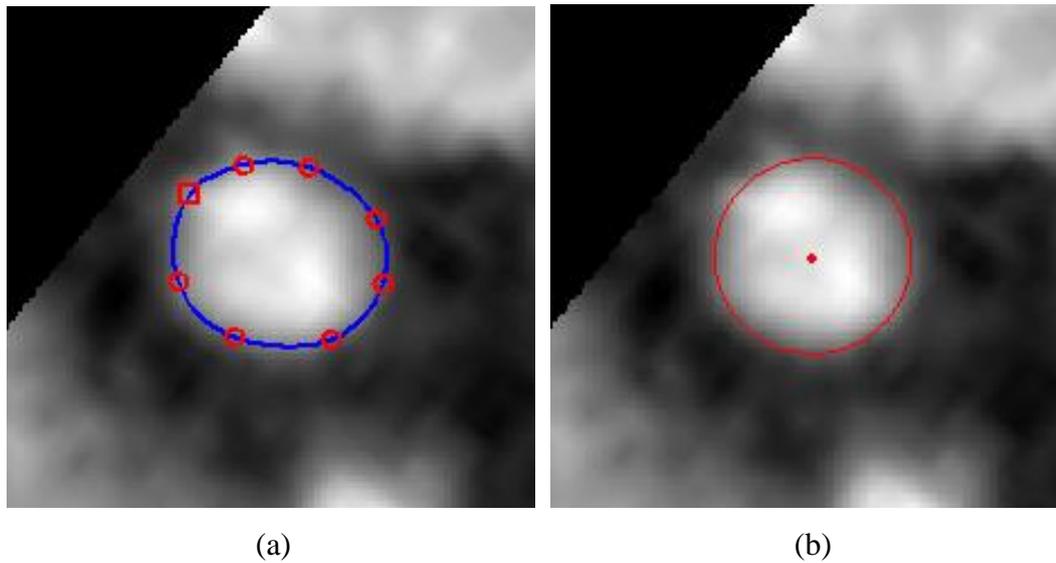
Figure 3.19: Determination of the ground truth data based on the successive cross sections. (a) An example of the annotation of the observer (show in blue), the red circles are the control points determined by the observer (the square denotes the starting control point), (b) The resulting ground truth data determined by the software in red. The red dot indicates the centre and the circle represents the radius of the artery at this cross section.

(a)	(b)
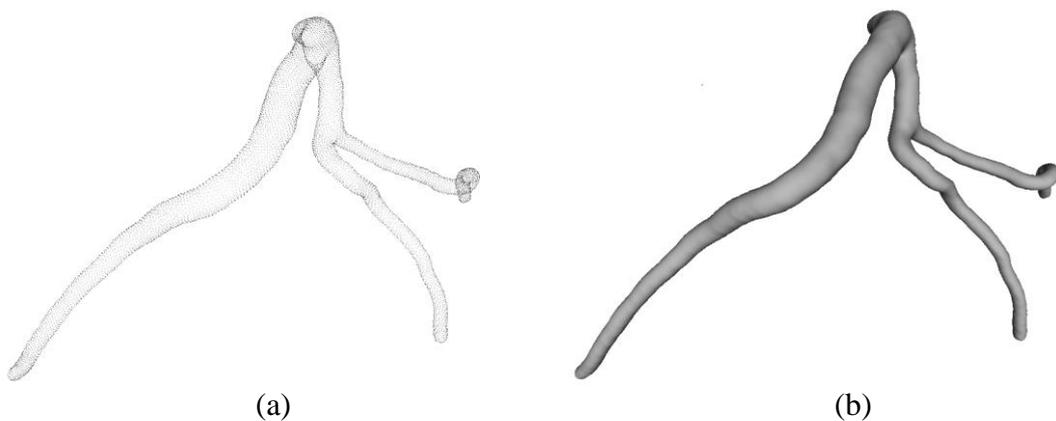
Figure 3.20: Construction of the ground truth surface from manually delineated vessel boundaries. (a) The boundary points of the left coronary artery constructed using the centreline and the corresponding radius information obtained via manual annotation, (b) The outer surface of the artery reconstructed based on the boundary points shown in (a).

Since the manual segmentation procedure is very time consuming, only four major branches, i.e., right coronary artery (RCA), left anterior descending artery (LAD), left circumflex artery (LCX), and one large side branch of the coronaries, were chosen for evaluation. In addition to the metrics defined in Eq. (3.22), the Hausdorff distance [142] was also applied to measure the difference between the

77

segmented vessel surface and the manually delineated ground truth data. The Hausdorff distance is defined as:

$$d_H(\mathbf{X},\mathbf{Y}) = \max\{\sup_{x\in X}\inf_{y\in Y} d(x,y), \sup_{y\in Y}\inf_{x\in X} d(x,y)\} \tag{3.23}$$

where *X*,*Y* are the vertices of the mesh surfaces of the arteries corresponding to the segmentation results and the ground truth, respectively, and *d(x,y)* measures the Euclidean distance between points *x* and *y* belonging to vertices **X** and **Y**. The mesh surface of the arteries was obtained by extracting the isosurface of the binary volume obtained from the segmentation/manual delineation, using the marching cube algorithm [143].

In Figs. 3.21-3.22 and Tables 3.4 and 3.5, we present the comparison of the resulting segmentation obtained using the proposed technique and Yang *et al.*, method with respect to the ground truth data. The initial surface for the active contour models was obtained through the application of a Hessian-based vessel enhancement filter described previously in Section 3.1. The tuning parameters of both of the two techniques were empirically determined from a training set, which consisted of three CT studies randomly selected from the available datasets. Specifically, for the proposed approach, we set $u = 0.2$, $v = 0.1$ and the radius of localised kernel was set to 7 voxels. The proposed approach was implemented in MATLAB (R2010b) on a standard specification PC (Dell Precision T3500, Inter(R) Xeon(R) CPU at 2.67GHz), and the average execution time was found to be 80 seconds for extraction of the entire coronary trees. Yang *et al*., on the other hand, requires roughly 45 seconds to carry out the same process.
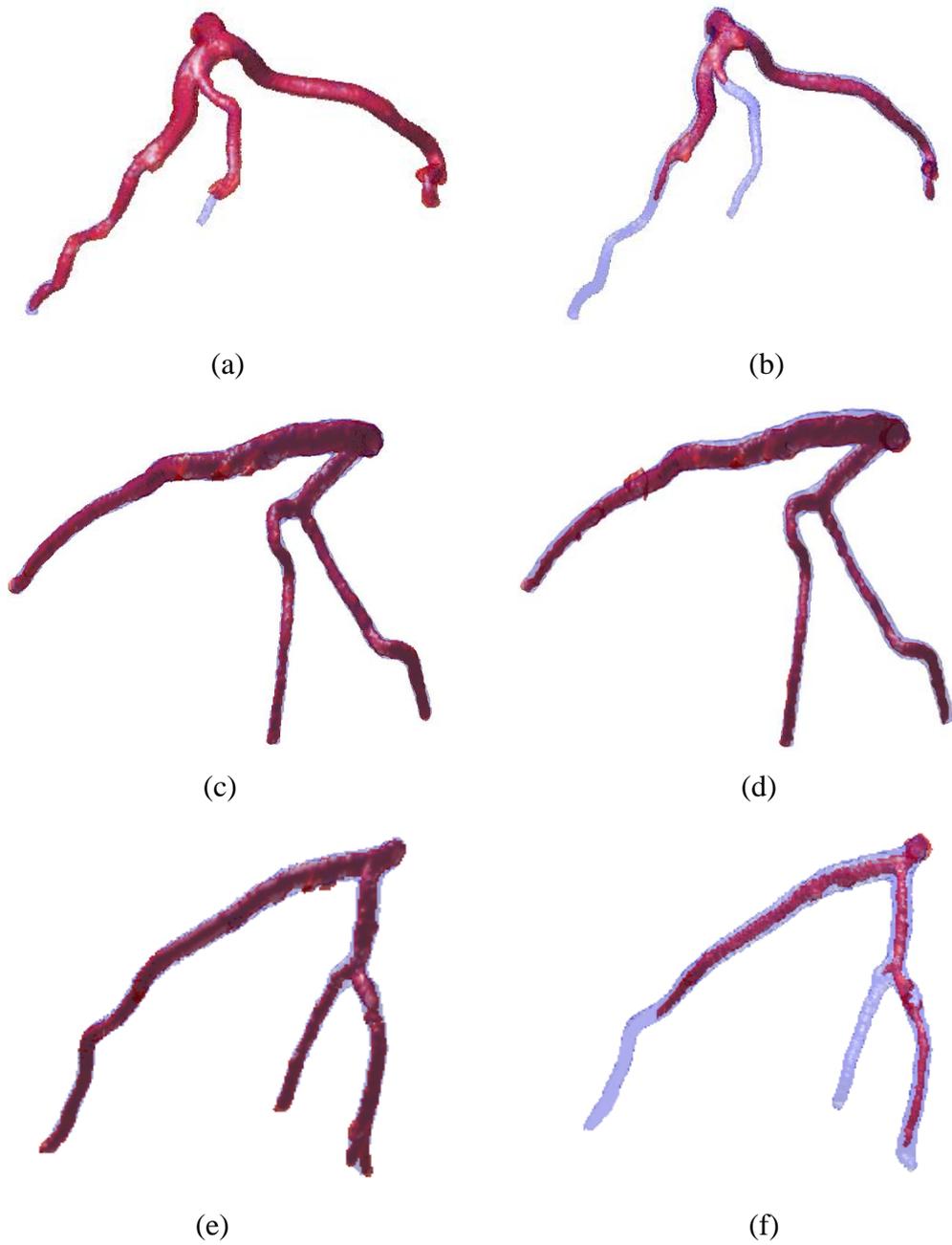
Figure 3.21: Comparison of the resulting segmentation for datasets #3, #5 and #11 obtained using the proposed model (a), (c) and (e), and Yang *et al.,* technique (b), (d) and (f), with respect to the ground truth data. The semi-transparent surface denotes the outer surface of the ground truth data, and the resulting segmentation is depicted in red.
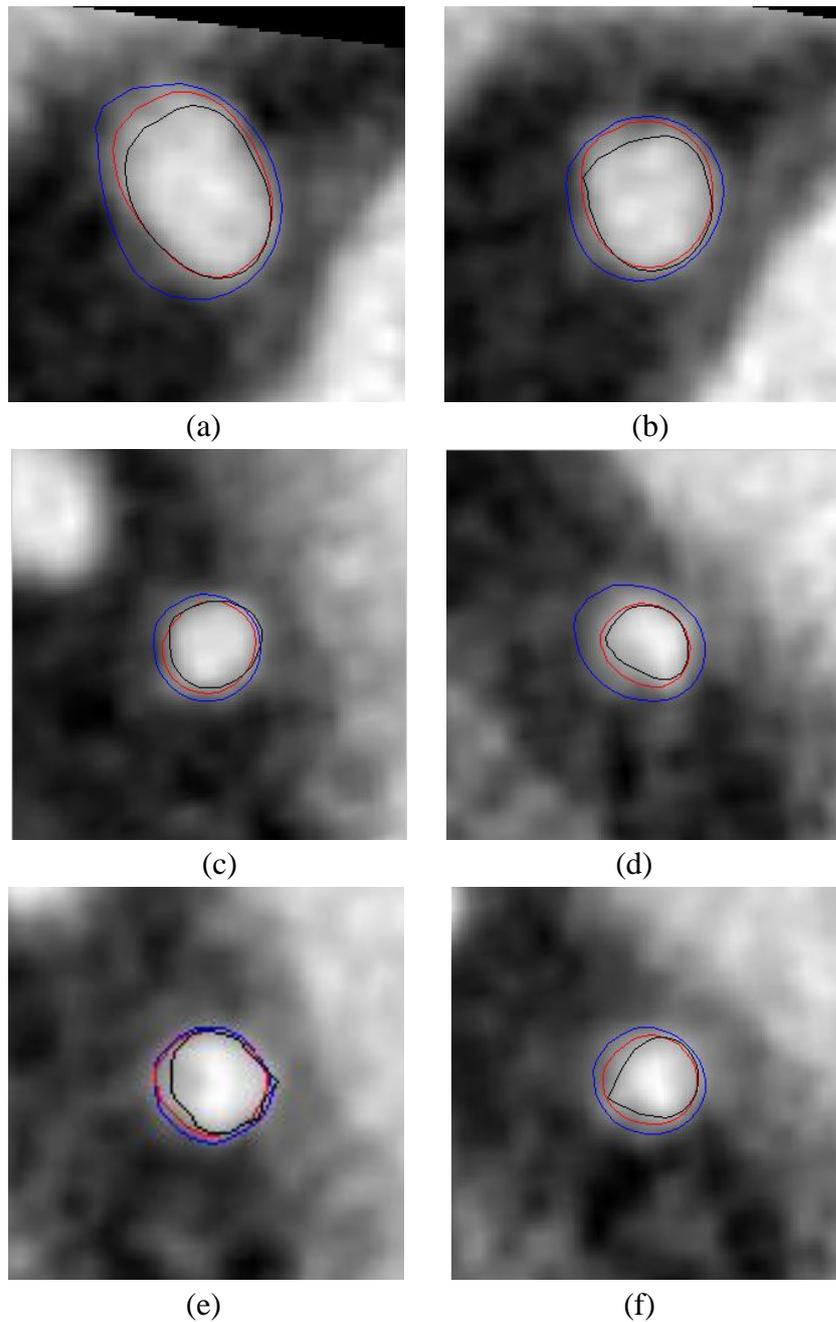
Figure 3.22: 2D transaxial images illustrating the segmentation results. (a) and (b) depict the resulting segmentation on 2D cross sectional images randomly taken from dataset #3, (c) and (d) depict the resulting segmentation on 2D axial image from dataset #5, The examples of the segmentation results on data #11 are illustrated in (e) and (f). The red contour represents the manually delineated ground truth, while the segmentation obtained from the proposed method and Yang *et al.*, method are shown in blue and black contours, respectively. Note that, the cross sectional images were up-sampled by a factor of five using linear interpolation to increase the resolution.

Table 3.4-A: Comparison of the 3D CTA segmentation results between the proposed method and Yang *et al.*, technique: Datasets #1-6

Metrics	Methods	3D CTA Images					
		1	2	3	4	5	6
TP (%)	Proposed	**94.1**	**93.9**	**93.1**	**92.8**	**97.0**	**93.2**
	Yang *et al.*,	47.6	50.3	52.1	25.6	89.9	87.9
FN (%)	Proposed	**5.90**	**6.10**	**6.90**	**7.20**	**3.00**	**6.80**
	Yang *et al.*,	52.4	49.7	47.9	74.4	10.1	12.1
FP (%)	Proposed	**32.4**	**28.4**	**43.1**	**38.3**	**45.5**	**29.4**
	Yang *et al.*,	1.31	8.39	13.6	3.16	6.07	6.89
OM	Proposed	**0.831**	**0.731**	**0.791**	**0.803**	**0.800**	**0.837**
	Yang *et al.*,	0.639	0.634	0.629	0.397	0.717	0.685
Mean(d_H)	Proposed	**0.623**	**1.02**	**0.670**	**0.833**	**0.623**	**0.782**
	Yang *et al.*,	0.865	1.35	1.00	1.09	0.767	0.891

Table 3.4-B: Comparison of the 3D CTA segmentation results between the proposed method and Yang *et al.*, technique: Datasets # 7-12

Metrics	Methods	3D CTA Images					
		7	8	9	10	11	12
TP (%)	Proposed	**90.1**	**89.0**	**95.3**	**80.5**	**86.5**	**87.8**
	Yang *et al.*,	51.2	49.2	88.4	53.6	23.4	26.7
FN (%)	Proposed	**8.90**	**11.0**	**4.70**	**19.5**	**13.5**	**12.2**
	Yang et al.,	48.8	50.8	11.6	46.4	76.6	73.3
FP (%)	Proposed	**41.6**	**38.6**	**51.8**	**35.2**	**42.2**	**44.7**
	Yang *et al.*,	3.16	1.57	16.3	10.0	9.55	6.18
OM	Proposed	**0.778**	**0.782**	**0.713**	**0.744**	**0.756**	**0.755**
	Yang *et al.*,	0.663	0.318	0.580	0.655	0.353	0.402
Mean(d_H)	Proposed	**0.759**	**0.719**	**0.620**	**0.561**	**0.769**	**0.783**
	Yang *et al.*,	1.07	1.63	0.976	1.15	1.24	0.861

Table 3.5: Comparison of the 3D CTA segmentation results between the proposed method and Yang *et al.*, technique (overall)

Rate	Methods	
	Proposed Method Mean	Yang *et al.*, Method Mean
TP (%)	91.1	53.8
FN(%)	8.90	46.2
FP (%)	39.2	16.9
OM	0.776	0.556
Mean(d_H)	0.730	1.07

As shown in Table 3.5, the mean TP rate and OM metric for the proposed method were found to be 91.1% and 0.776, respectively, which indicate that the proposed method is able to correctly extract the major branches of the coronary arteries (see Figs. 3.21 (a), (b) and (c)). Meanwhile, the high values of the FP rate (39.2% on average) mean that the proposed method over-segments the arteries, as illustrated in Fig. 3.22, where the segmentation results were shown on the 2D axial image as contours. In these axial images, the red contours represent the ground truth boundary, and the blue and black curves represent the segmentation obtained using the proposed method and Yang *et al*., algorithm, respectively. Since the ground truth data were modelled as circular cross sectional tubes, this would lead to the resulting ground truth data under-estimating the true vessel surfaces. However, in terms of the voxel-wise measurements, the average value of the Hausdorff distance metric was found to be 0.73 voxels, which implies that the proposed method is capable of extracting the luminal surfaces of the arteries with sub-voxel accuracy.

In terms of the FP rate, the Yang *et al.*, method outperforms the proposed approach, with the average value found to be 16.9%. However, we note that the TP and OM metrics of their segmentation results are significantly lower than those of the proposed technique, with the average values being 53.8% and 0.556, respectively. In addition, by observing the statistics presented in Table 3.4, we note that both the TP rate and the OM metric vary significantly, with the TP rate ranging from 23.4% to 89.9%, while the minimum and maximum values of the OM metric were found to be 0.318 and 0.717, respectively. These observations imply that Yang *et al.*, model under-segments the coronary arteries and is only able to extract partial branches of the arterial tree, which is illustrated in Figs. 3.21(b), (d) and (e). The reason for this is that the Yang *et al.*, technique, solely relying on global intensity statistics, is sensitive to image contrast and brightness changes. The method is able to correctly extract the arteries when the intensity densities are evenly distributed along the vessel. However, uneven intensity distribution is commonly encountered in coronary CTA, because of the concentration attenuation of the contrast agent and acquisition noise. In this case, the Yang *et al.*, approach can only extract the proximal segments of the arteries, since distal segments have relatively lower

intensity values and lack image contrast. In addition, we also found that the TP and OM rates of the proposed method tend to decrease when approaching the distal and small segments of the arteries. However, clinically significant coronary lesions are usually identified in the main and proximal branches of the arteries, which can be well defined by the proposed method. Nevertheless, we can conclude that our technique is able to delineate the vessel boundaries in clinically important coronary segments with a level of variability similar to those obtained through manual segmentation.

Two CTA studies were affected by the presence of kissing vessels (i.e., datasets #7 and #11). The slice-by-slice correction scheme was subsequently applied after the first step of the segmentation. Fig. 3.23 illustrates the 3D surface reconstruction image before and after applying the slice-by-slice correction algorithm. Fig. 3.24(a) shows the first slice, which contains the cross sectional segments of the coronary arteries. The false positives, i.e., the kissing vessel artifacts, were identified and then tracked in Figs. 3.24(b)–(e). The boundaries of the coronary arteries are shown in red, and the green curve represents the kissing vessel structures. In Fig. 3.24(f), we illustrate the initial segmentation of the axial image shown in Fig. 3.24(e) prior to the correction.

(a)   (b)
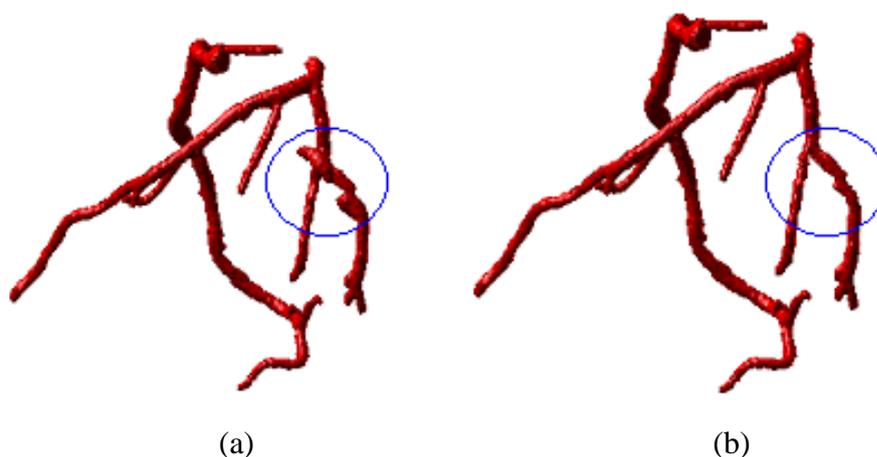
Figure 3.23: The comparison (a) before and (b) after the correction process (datasets #7). The touching non-arterial vessel (within the blue circle) has been removed.
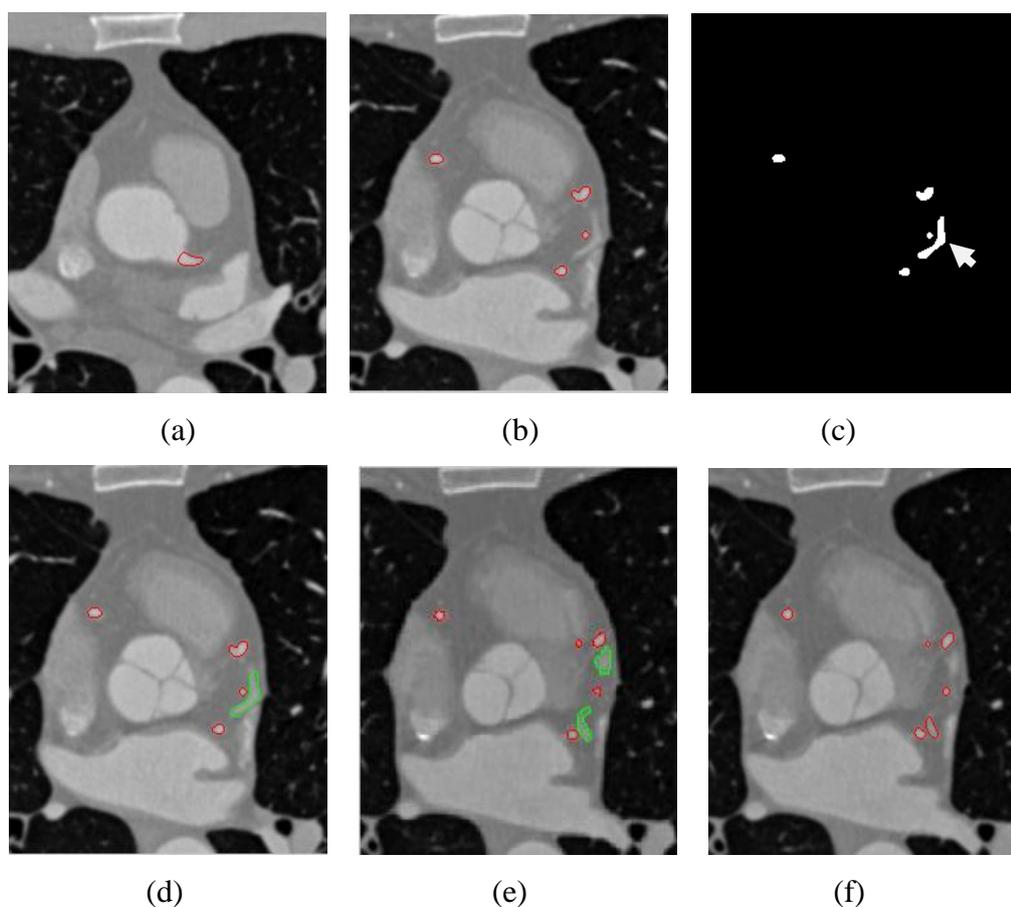
Figure 3.24: Transaxial slices illustrate the slice-by-slice correction algorithm. (a) The first slice contains the artery (delineated in red), (b) The artery is tracked through slices, (c) The binary image obtained from the first stage segmentation, this is the first slice that contains the kissing vessel (arrowed), (d) and (e) Kissing vessel is identified and tracked over slices (depicted in green contours), (f) The original segmentation in same transaxial slice as shown in (e).

Instead of using the entire volume to quantify the performance of the slice-by-slice correction, we conduct the assessment on a 2D axial image basis. The resulting segmentation with and without the slice-by-slice correction is illustrated in Fig. 3.25, where the boundaries of the artery before and after correction are depicted in black and blue respectively, and the manual segmentation is shown in red. The four metrics, defined in Eq. (3.21), were used to quantify the performance and the results are shown in Table 3.6. It can be observed from the table that the FP rate, which is primarily caused by the kissing vessels, is dramatically reduced after the application of the slice-by-slice correction algorithm (reduced from 294% to 22.8% for arterial

segments containing kissing vessels, e.g., the vessel segment shown in Fig. 3.23(a), within the circle).

(a)   (b)
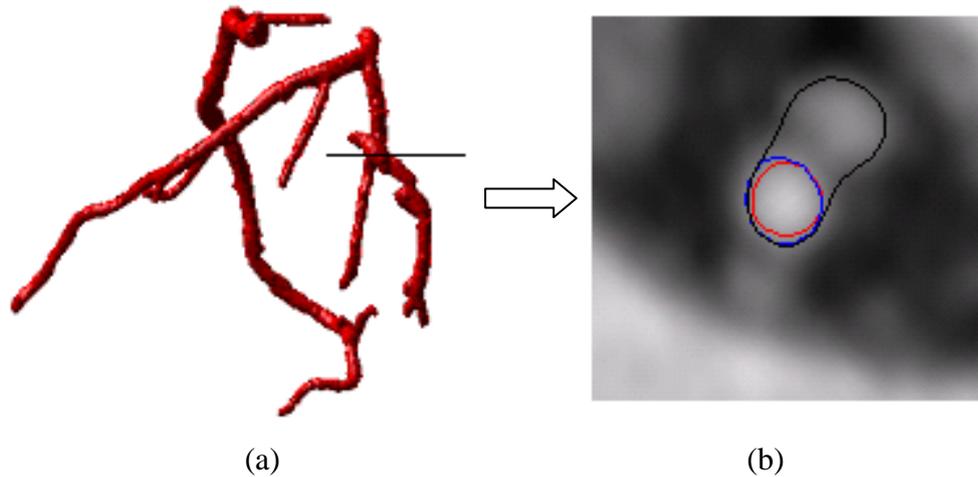
Figure 3.25: The efficiency of the proposed slice-by-slice correction algorithm demonstrated by cross sectional view image. (a) 3D volume data, and (b) Cross sectional view image randomly taken from the 3D volume data, illustrating the resulting segmentations with and without the correction step are shown in blue and black, respectively. The red contour represents the reference boundaries of the vessel obtained through manual delineation.

Table 3.6: Comparison of the segmentation results before and after the application of the correction scheme

Rate	Before	After
TP (%)	82.4	85.3
FN (%)	17.6	14.7
FP (%)	294	22.8
OM	0.380	0.820

3.5 Conclusions

Accurate segmentation of vascular structures is an essential and fundamental step for various clinical tasks, such as stenosis grading and surgical planning. In this chapter, we presented a computer vision system which contributes towards the development of the proposed framework for segmentation of coronary arteries in 3D CTA images. In particular, a novel two-step algorithm was proposed to

efficiently segment coronary arteries from CT images by making use of both global and local intensity statistics. The global energy was designed as a normalised CDF based on the histogram of the input image data, which adapts its contribution to the overall active contour energy by considering the spatially varying properties of the artery. The kissing vessels were identified and tracked throughout the axial slices in the second stage of the segmentation based on a multiregion competition algorithm. Experimental results show that the proposed approach is able to correctly segment the major branches of the arterial tree, with an average voxelwise distance of 0.73 voxels to the manually delineated ground truth. Furthermore, in the presence of kissing vessel artifacts, the overall performance of the segmentation can be significantly improved by the slice-by-slice correction scheme. The FP rate from these cross sections containing kissing vessels was reduced from 294% to 22.8%.

In Chapter 4, we will present a quantitative vascular shape analysis framework for coronary arteries, based on the segmentation results obtained from this chapter, aiming at characterising the geometric parameters of the coronary arteries. This will provide the cardiologist with meaningful information in the assessment of the severity of the luminal stenosis caused by atherosclerotic plaques, and potentially the means for evaluation of the functional significance of coronary stenoses by carrying out image-based haemodynamic analysis of the blood flow in the arteries

.

Chapter 4

3D Quantitative Vascular Shape Analysis for Coronary CT Images

In this chapter, we present an automated framework for quantitative vascular shape analysis in coronary CT angiographies. The segmented coronary arteries obtained from the previous chapter are used to construct the luminal surface for analysis. These two chapters naturally provide a complete toolkit for quantitative coronary analysis in CTA images, which are the key components in developing computer-aided diagnostic systems for the assessment of the severity of coronary stenosis. Followed by this introduction, the outline of the proposed framework is firstly presented in Section 4.1. Next, we describe the proposed method in detail in Sections 4.2-4.4. This is followed by the presentation and analysis of experimental results obtained from both synthetic and clinical datasets, demonstrating the efficiency and accuracy of our approach in Section 4.5. The chapter ends with the conclusions of the presented work in Section 4.6.

4.1 Algorithm Outline

Fig. 4.1 shows the block diagram of the proposed approach. It commences with the segmentation of the arteries in coronary CT images, which has been previously discussed in Chapter 3. Then, the binary volumetric image data is converted to its equivalent mesh domain representation by extracting the zero isosurface using marching cube algorithm [143]. Next, we apply the mesh contraction algorithm [144], to define the initial location centreline locations of the arterial trees. The resulting centreline data, C_0, are represented by two separate arrays, holding the coordinates of the centreline points (nodes) and the sets of indices, which define the adjacent points for each node, respectively. Based on the initial centreline (C_0), bifurcation points are automatically detected by finding the centreline nodes with

more than two connected neighbours. Next, for each constituent vessel of the bifurcation, two endpoints located prior and distal to that bifurcation are selected and the associated cross sections are determined, respectively. In the following step, an initial tube model is constructed by using the original centreline and the associated cross sections, where the remaining cross sections along the centreline of the tube are obtained through linear interpolation between the two endpoints. In the following step, the algorithm alternates between registering the tube on the vessel surface and estimating the cross sectional shape of the tube, based on the current model. Once the fitting process is completed, the central axis of the tube model is considered as the resulting centreline for each of the constituent vessel segments of the bifurcation, and the tube surface can be used as the reference vessel.
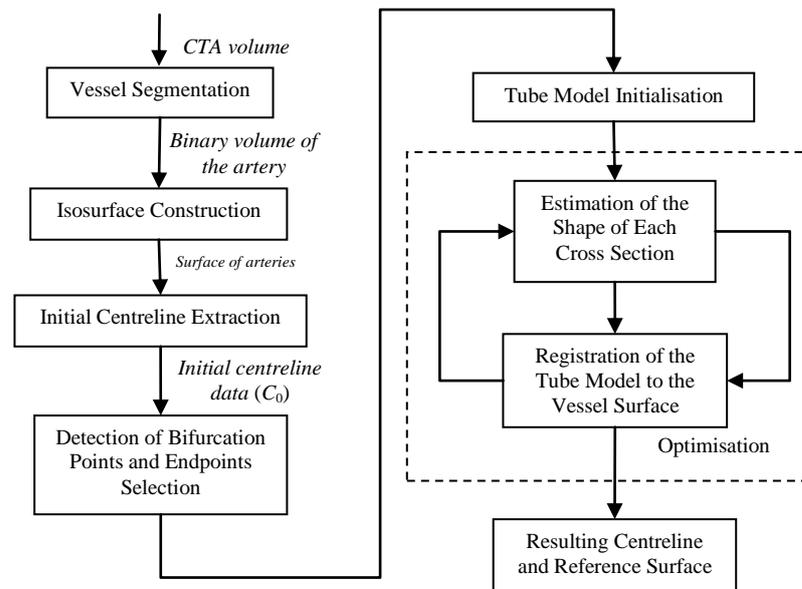
Figure 4.1: Flow chart of the proposed framework.

4.2 Model Initialisation

In the first step of the proposed method, each constituent branch of the bifurcation requires the determination of two endpoints for the initialisation of the tube model. The endpoints should be located within the 'normal' regions of the vessel of interest to ensure the correct generalisation of the model and speed up the convergence of the tube registration process. Subject to the assumption that healthy vessel cross

88

sections are approximately circular, we employ the normalised circularity metric to rule out abnormal segments of the vessels, such as those containing bifurcations and aneurysms. To initialise the tube centreline, two endpoints are initially selected one node ahead and distal to the bifurcation point on the original centreline, respectively. When the selected points are located within abnormal regions, a rectification procedure automatically determines their appropriate location by moving them (backwards or forwards) along the initial centreline until the circularity criterion is met. Once the end points are determined, we initialise the central axis of the tube model using the initial centreline and determine the cross sections through linear interpolation between the two ends. The green planes shown in Fig. 4.2 are potential ending cross sections determined by the proposed scheme in the 'normal' segments of the artery.
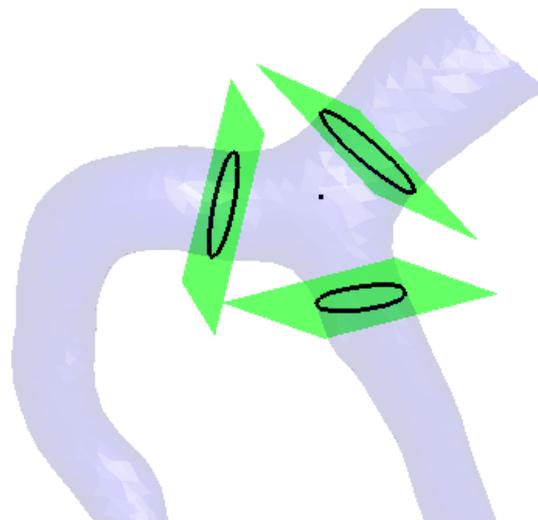
Figure 4.2: The 3D diagram illustrates the possible locations of the ending cross sections for construction of the tube model at an arterial bifurcation. The semi-transparent structure represents the vessel surface, while the possible ending cross sections are depicted in green. The black curves are associated with the intersections between the vessel surface and the ending cross sections. The bifurcation point is represented by black dot.

4.3 Construction of the Deformable Tube Model

To characterise the morphology of the bifurcation and explore the full 3D information of the reference surface, a closed surface representing the reference vessel's boundaries is required. In this research, we define the tube model, $R(v,\theta)$,

in terms of its central axis and the corresponding cross sections. The points $v=\{v_i, i=1,...,N\}$ represent the path of the N control points (moving nodes), where N is adaptively chosen to ensure the distance between adjacent moving nodes is less than 0.5 voxels, and $\theta=\{\theta_i, i=1,...,N\}$ is an array consisting of the parameters of the associated cross sections. In this research, the cross section of the tube model is approximated as the best fitting ellipse. Hence, at the i-th moving node v_i, the parameter vector is defined as $\theta_i=\{a_i,b_i,u_{1i},u_{2i},\varphi_i\}$, where a_i and b_i represent the semi diameters of the axes of the ellipse, u_{1i} and u_{2i} denote the origin of the ellipse, and φ_i is the tilt angle. The central axis of the tube is defined using a B-spline curve with N moving nodes, and the surface of the tube can be reconstructed from its circumferences (i.e., the cross sections along its centreline) by using the ball pivoting algorithm.

The tube registration problem is solved by minimising a generic active contour energy functional, defined as follows:

$$E = E_{Int} + \eta E_{Ext} + \gamma E_{Con} \tag{4.1}$$

where η and γ are constants, controlling the influence of each energy term on the total tube energy. The internal energy, E_{Int}, is comprised of the elasticity ($v'(s)=dv/ds$, where $v(s)$ represents the medial axis and s is the parameterisation variable) and the stiffness of medial axis ($v''(s)=d^2v/ds^2$):

$$E_{Int} = \int_s (\alpha \, | \, v'(s)|^2 + \beta \, | \, v''(s)|^2)ds \tag{4.2}$$

where the constants α and β are the weights for the elasticity and stiffness, respectively.

The external energy functional, E_{Ext}, is derived from the fitting error between the tube model and the desired vessel segment. This poses a strong constraint on the tube based on its position with respect to the vessel surface, making the tube deform and follow the course of the vessel of interest. In this research, we define the external energy of the tube as follows:

$$E_{Ext} = \int_s F(v(s),\theta)ds \tag{4.3}$$

where $F(\mathbf{v}(s),\boldsymbol{\theta})$ is a scalar function, returning the similarity score between the tube model and the desired branch. The metric is defined as the weighted directional distance between the fitting tube and the vessel surface, which will be discussed later on in Section 4.4.2.

The elastic force defined in the internal energy favours small distances between adjacent centreline points, which will eventually shrink the curve to a single point. To prevent shrinking, an additional constraint, which encourages equal spacing between the centreline points, is defined as follows:

$$E_{Con} = \left| d(\mathbf{v}(s)) - d \right|^2 \qquad (4.4)$$

where $d(\mathbf{v}(s))$ denotes the distance between the control point $\mathbf{v}(s)$ and its successive neighbour along the centreline, and d is the average distance between centreline points.

4.4 Optimisation Procedures for Tube Registration

In this research, the reference surface for each constituent branch of a bifurcation is constructed through the registration of a deformable tube model to the desired branch. In contrast to conventional tubular models using fixed cross sections, the proposed approach adaptively updates the shape of the tube model, thus resulting in a more robust and accurate estimation. To this end, the method alternates between updating the cross sectional shape of the tube and registering the tube model to the desired branch.

4.4.1 Estimation of the shape of each Cross Section

The circular cross sectional tube is the most popular model to approximate vascular structures in the literature [118, 120, 145-148]. Vessels, however, are elastic bodies, which can accommodate local deformations of the lumen due to changes in blood flow and intraluminal pressure within the artery. Such deformations cannot be accurately represented using circular cross sections. Hence, we use an elliptical cross sectional tube model to approximate the vessel surface, which provides sufficient degrees of freedom to accommodate the potential

deformations and facilitates accurate estimation of the vessel cross sections. An ellipse can be defined in parametric form as:

$$x = u + Q(\varphi)x'$$ (4.5)

where,

$$u = (u_1, u_2)^T, x' = \begin{pmatrix} a\cos t \\ b\sin t \end{pmatrix}, Q(\varphi) = \begin{pmatrix} \cos\varphi & -\sin\varphi \\ \sin\varphi & \cos\varphi \end{pmatrix}$$

where x denotes a point located on the circumference of the ellipse, u is the centre of the ellipse, a and b represent the semi-lengths of its axes, φ denotes the tilt angle, i.e., the angle between the x-axis of the local coordinate system and the major axis of the ellipse, and t is an angular parameter varying between 0 to 2π. The minimum distance of an arbitrary point, $p = [p_1, p_2]^T$, to the circumference of the ellipse can be found by:

$$dist = \min_t |p - x|^2 = \left\| \begin{pmatrix} p_1 \\ p_2 \end{pmatrix} - \begin{pmatrix} u_1 \\ u_2 \end{pmatrix} - Q(\varphi)\begin{pmatrix} a\cos t \\ b\sin t \end{pmatrix} \right\|^2$$ (4.6)

Let $\mathbf{P_i} = [(p_{11}, p_{12}), (p_{21}, p_{22}), ..., (p_{m1}, p_{m2})]^T$, ($m > U$, where $U \geq 5$ with the lower value representing the number of free parameters of the ellipse) to be the intersection points, found by slicing the vessel surface using a perpendicular plane at the location of each moving node. The best fit ellipse, for which the sum of the squares of the distances to the given points is minimum, can be found by solving the following nonlinear least squares problem [149]:

$$\sum_{j=1}^{m} \left\| \begin{pmatrix} p_{j1} \\ p_{j2} \end{pmatrix} - \begin{pmatrix} u_1 \\ u_2 \end{pmatrix} - Q(\varphi)\begin{pmatrix} a\cos t_j \\ b\sin t_j \end{pmatrix} \right\|^2 = \min$$ (4.7)

In order to produce a smooth and anatomically correct generalisation of the tube model, we further constrain the area of the fitting ellipse, by limiting the lengths of its axes, based on its neighbouring slices. Specifically, we restrict the length of the axes of the ellipse to lie in the range of $[1-c, 1+c]$ with respect to its adjacent cross sections. The constant c (fixed to 0.2 in this thesis) is determined based on the

viscoelastic properties of the vessel in [150], where the authors conducted a series of *in vitro* experiments to validate the ability of their computational fluid dynamic (CFD) model in simulating blood flow within the vessel by considering the deformation of the vessel wall.

Let $\boldsymbol{\tau} = [t_1,\ldots, t_m, a, b, u_1, u_2, \varphi]^T$ denote the unknown parameters, which need to be determined. By taking into consideration the constraints imposed on the axes of the ellipse, we set up the constrained nonlinear least squares problem as follows:

$$\min_{\boldsymbol{\tau}} \sum_j \left\| \begin{pmatrix} p_{j1} \\ p_{j2} \end{pmatrix} - \begin{pmatrix} u_1 \\ u_2 \end{pmatrix} - Q(\varphi) \begin{pmatrix} a\cos t_j \\ b\sin t_j \end{pmatrix} \right\|^2 \tag{4.8}$$

$$subject \ \ to \ \ A\boldsymbol{\tau} \leq W$$

where

$$A = \begin{bmatrix} \overbrace{0 \ldots 0}^{m} & 1 & 0 & 0 & 0 & 0 \\ 0 \ldots 0 & -1 & 0 & 0 & 0 & 0 \\ 0 \ldots 0 & 0 & 1 & 0 & 0 & 0 \\ 0 \ldots 0 & 0 & -1 & 0 & 0 & 0 \end{bmatrix} \quad W = \begin{bmatrix} 0.8a_{i-1} \\ 1.2a_{i-1} \\ 0.8b_{i-1} \\ 1.2b_{i-1} \end{bmatrix}$$

The subscript i denotes the i-th moving node along the central axis of the tube model. The solution of the constrained nonlinear least squares problem in Eq. (4.8) can be obtained using a subspace trust regions method [151] and the interior reflective Newton method [152].

4.4.2 Calculation of the Tube Energy

By discretising the energy functional defined in Eq. (4.1), the tube energy can be rewritten as:

$$E_{Total}(\boldsymbol{v}_1,\ldots,\boldsymbol{v}_N) = \sum_{i=1}^{N} E_{Int}(\boldsymbol{v}_i) + \eta E_{Ext}(\boldsymbol{v}_i) + \gamma E_{Con}(\boldsymbol{v}_i) \tag{4.9}$$

where

$$E_{Int} = \alpha \mid \mathbf{v}_i - \mathbf{v}_{i-1} \mid^2 + \beta \mid \mathbf{v}_{i+1} - 2\mathbf{v}_i + \mathbf{v}_{i-1} \mid^2$$
$$E_{Ext} = F(\mathbf{v}_i, \boldsymbol{\theta}_i) \qquad (4.10)$$
$$E_{Con} = \mid (\mid \mathbf{v}_i - \mathbf{v}_{i-1} \mid)^2 - d \mid^2$$

and

$$d = \frac{1}{N-1} \sum_{i=2}^{N} \mid \mathbf{v}_i - \mathbf{v}_{i-1} \mid^2$$

Here, $\mathbf{v}_i$ denotes the moving node of the tube centreline, and the external energy is calculated by $F(\mathbf{v}_i, \boldsymbol{\theta}_i)$, which returns the weighted sum of squared errors between the estimated cross sections $\boldsymbol{\theta}_i$ and the vessel boundaries intersected by the cross section at the location of the moving node $\mathbf{v}_i$. Due to the irregular geometry of the vessel cross sections at the location of the bifurcation, as shown in Fig. 4.3, not all of the intersection points belong to the desired branch, rather a subset of the intersection points may belong to another vessel branch. Hence, modelling the tube cross sections using all of the intersection points may introduce inaccuracies in defining the reference vessel surface. To address this issue, we make use of directional information to measure the difference between the model and the vessel boundaries, where the intersection points belonging to the desired vessel surface are assigned higher weights.

(a)   (b)
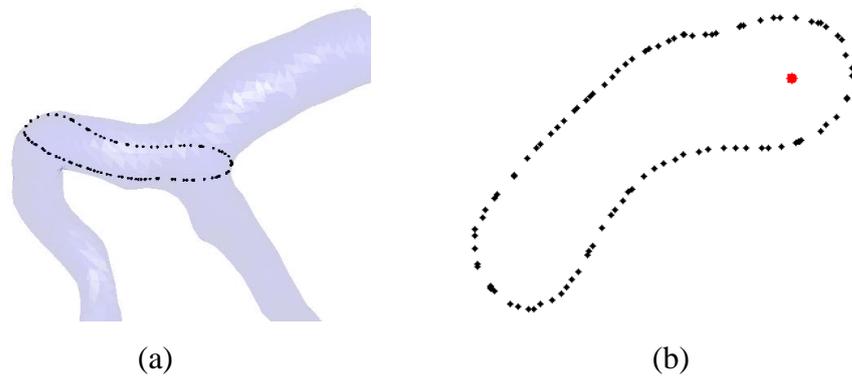
Figure 4.3: Illustration of the intersection points taken from the vessel bifurcation. (a) The 3D view shows the intersection points in the vicinity of the vessel bifurcation, (b) The intersected points of (a) shown in a 2D projection image. The black dots are the vessel boundary points, while the red dot is the position of the centreline point at the cross section. Points on the right side of the centreline location belong to the right vessel surface, and exhibit normal shape. Their left hand side counterparts belong to the side branch of the bifurcation, and are characterised by an irregular shape.

A vessel bifurcation is defined as the subdivision of a vessel into two branches. As depicted in Fig. 4.4(a), it can be considered as a single object delineated by the left, middle and right contours, respectively [153]. In Fig. 4.4(b), we extend this concept to 3D images, where a bifurcation comprises three surfaces, namely the left, middle and right surfaces, respectively. As an example, let us consider the vessel segments shown in Fig. 4.3(a), the objective being to fit the tube model to the distal main branch (the right branch) over the bifurcation. To this end, the tube surface needs to be accurately registered onto the right surface of the vessel, as its left counterpart belongs to another constituent vessel of the bifurcation. However, it should be noted that the terms 'left' and 'right' surface are ambiguous in 3D space, as the definitions of 'left' and 'right' are relative to the viewpoint. In order to correctly register the tube model onto the desired surface, we propose a viewpoint-independent procedure to determine the surface of interest in an automated fashion.

(a)   (b)
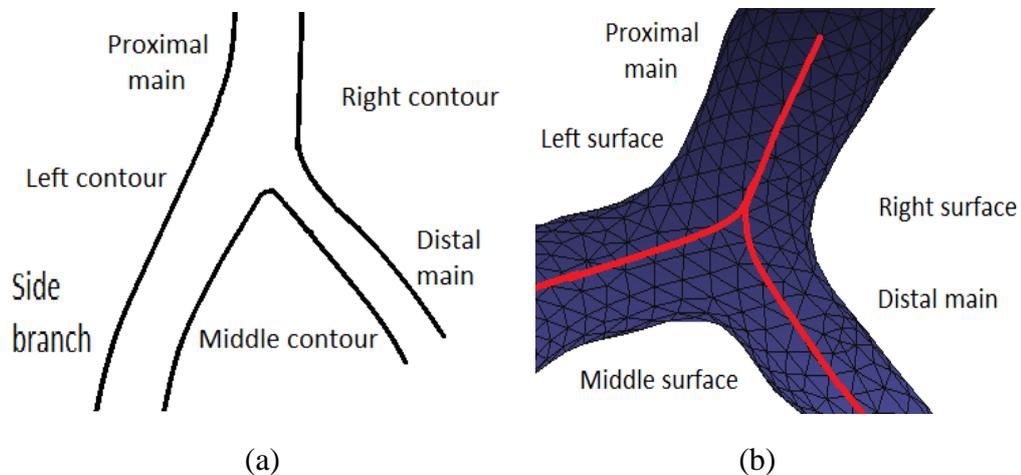
Figure 4.4: Representation of the vessel bifurcation in (a) 2D, and (b) 3D images, respectively. The vessel bifurcation is treated as a single segment delineated by three contours/surfaces.
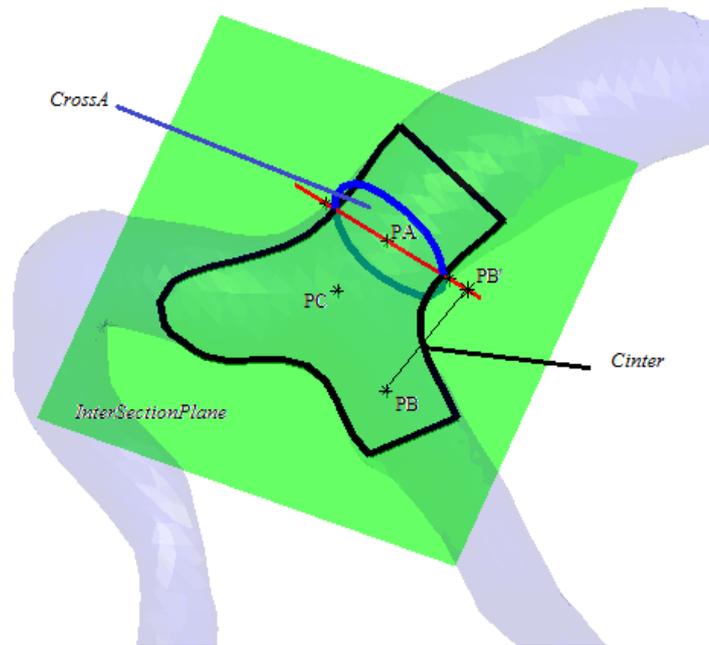
Figure 4.5: Illustration of the proposed scheme for the determination of the desired surface. The semi-transparent structure represents the vessel surface. The intersection plane, defined by the endpoints PA and PB together with the bifurcation point PC, is shown in green. The black curve depicts the intersection curve between the plane and the vessel surface near the bifurcation. The cross section taken at endpoint PA, denoted by CrossA, is delineated by the blue contour, and the red line shows the x-axis direction of the cross section at PA.

As illustrated in Fig. 4.5, we firstly find the intersection curve (C_{inter}, shown in black) between the vessel surface and the intersection plane (i.e., the green plane), defined by the two endpoints (PA and PB) together with the bifurcation point (PC), in the vicinity of the bifurcation area. Then, the orientation of the *x*-axis of the cross section at PA (denoted by *CrossA*) coincides with the direction of the line segment (shown in red), defined as the intersection between the plane *CrossA* and the curve C_{inter}. Next, we project the endpoint PB onto the plane *CrossA* (denoted by PB´), and the weight distribution is subsequently determined based on the sign of the *x* coordinate of the projection point PB´. Specifically, when PB´ is located on the left-hand side of plane *CrossA*, the 'left' constituent branch is considered as the desired branch, where it is assumed that the positive direction of the *x*-axis of a plane points to the 'right'. Consequently, the intersection points located on the left half plane of the cross section are assigned higher weights, and vice versa. In order to deal with the torsion of 3D vessels, the technique of rotation minimising frames [154] is

employed to determine the local reference frame for each point of the centreline axis of the tube. Based on the local frame, we define the directional weights as:

$$w = \frac{1}{\sqrt{2\pi\sigma^2}} \exp\left(\frac{-(\varphi-\vartheta)^2}{2\sigma^2}\right) \qquad (4.11)$$

where ϑ is an angular parameter as illustrated in Fig. 4.6(a), φ is the tilt angle of the estimated ellipse at the current cross section, and σ indicates the variance of the normal distribution, which is chosen to be equal to 60 degrees (see Fig. 4.6(b)). The weights assigned for fitting the left and right surfaces are shown in Figs. 4.6(c) and (d), respectively.

(a) (b)

(c) (d)
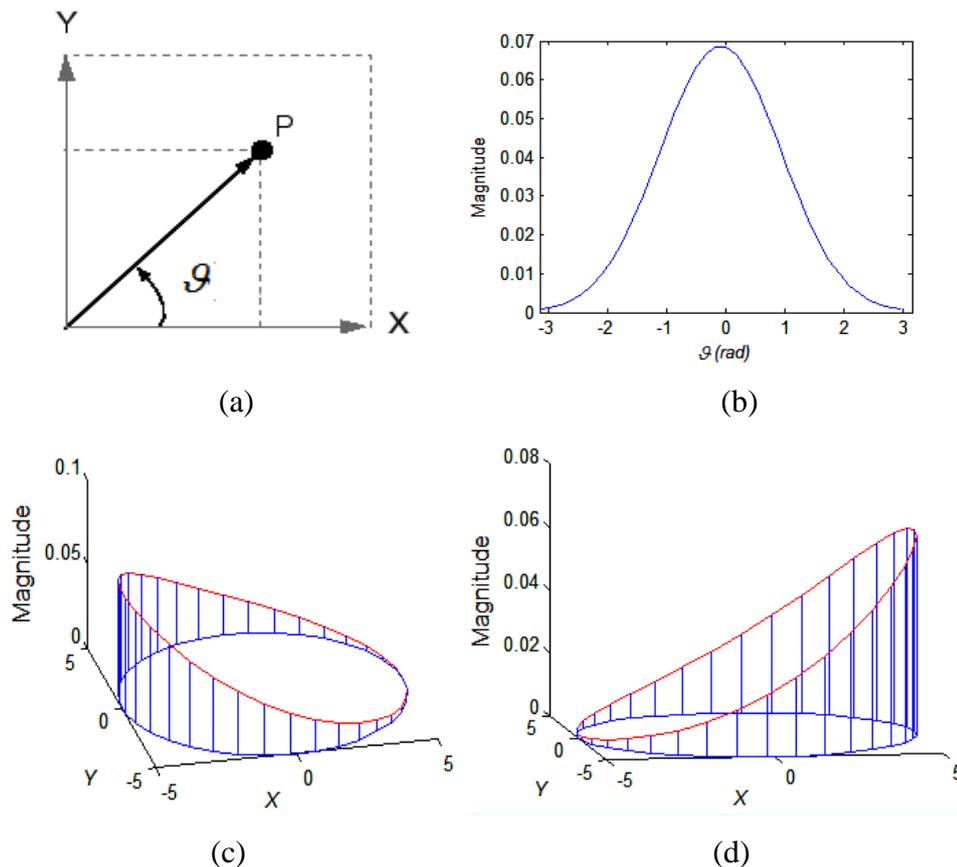
Figure 4.6: The directional weights scheme used in the registration of the tube to the desired surface in the bifurcation. (a) The definition of the angular coordinate system, (b) The weight distribution as a function of the angle, when fitting the right hand side surface, (c) and (d) 3D plots of the distribution of weights for the left and right surfaces, respectively. The estimated cross section is shown in blue and the height of the plot at each point indicates the relative magnitude of the weights.

97

Given the parameter vector of the cross sectional model $\theta_i=\{a_i,b_i,u_{1i,}u_{2i},\varphi_i\}$, i.e., the best fit ellipse approximating the cross sectional shape of the vessel at the i-th moving node, and the directional weights, the goodness of the fit for each cross section at the moving node $\boldsymbol{v}_i$ can be expressed as:

$$F(\boldsymbol{v}_i,\boldsymbol{\theta}_i)=\sum_{j=1}^{g}\min_{t_j}\{w_j\left\|\begin{pmatrix}p_{j1}\\p_{j2}\end{pmatrix}-\begin{pmatrix}u_{1i}\\u_{2i}\end{pmatrix}-Q(\varphi)\begin{pmatrix}a\cos t_j\\b\sin t_j\end{pmatrix}\right\|^2\}\qquad(4.12)$$

where $\mathbf{P}=\{(p_{j1},\ p_{j2}),\ j=1,...,g\}$, denote the intersection points as defined in the previous section, w_j is the weight associated with the direction t_j, and g denotes the number of points on the intersection.

4.4.3 Minimisation of the Tube Energy Functional

Rather than minimising the overall energy functional defined in Eq. (4.1), it is possible to examine the effect of the moving nodes within the model, by minimising the energy functional at each node in turn, and allowing the model to move as a whole to fit the vessel surface through an iterative process. One way of doing so is through the use of an exhaustive search algorithm [155]. Exhaustive search, or known as Brute-force search, is one of the simplest ways to solve computationally hard optimisation problems. It is a greedy search, scanning each possible solution in the space of candidate solutions (known as the search space), and terminates when a local optimum is reached. However, the optimal locations of the centreline obtained by means of the conventional greedy algorithm take place at each moving node, without considering the effect of the current node on the total energy of the solution.

Dynamic programming (DP), on the other hand, is a serial multistage decision process connected in series, which ensures the global optimality of the solution [155]. DP firstly decomposes the problem to be solved as a number of single stage processes, and then combines these single stage (suboptimal) solutions to reach an overall solution. By doing so, it translates a complex problem as a series of sub-problems, which is easier to solve. This principle is illustrated in the example of Fig. 4.7, which describes a typical shortest path problem in a network.
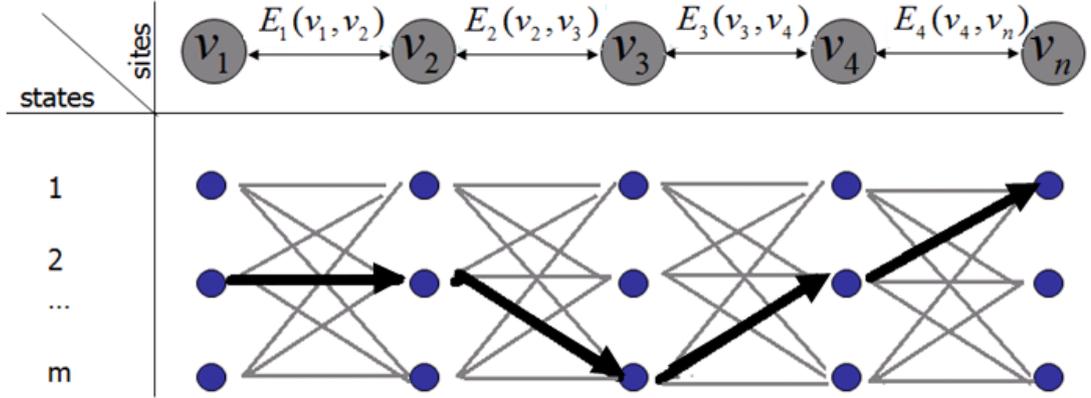
Figure 4.7: Schematic diagram illustrating a multiple stage decision process using a weighted network. Boldfaced arcs constitute the optimal path.

The graph was drawn for simplicity in a 5-stage arrangement, with the cost between the adjacent state variables at v_i and v_{i+1}, denoted by $E_i(v_i,v_{i+1})$. For each state variable, v_i, in the i-th decision stage, m possible choice of solutions are given. The shortest path, associated with the minimum cost of a sequence connecting v_0 and v_{k+1}, can be found using the recursive formulation as follows:

$$S_k(\mathbf{v}_{k+1}) = \begin{cases} \min_{v_k}\{S_{k-1}(\mathbf{v}_k)+E_k(\mathbf{v}_k,\mathbf{v}_{k+1})\}, & \text{if } k>0 \\ 0, & \text{if } k=0 \end{cases} \qquad (4.13)$$

where $S_k(v_{k+1})$ is the total cost of the path up to the $(k+1)$-th stage. Eq. (4.13) states that the minimal (shortest) path from the starting source up to the stage v_{k+1}, can be found by considering the (minimum) costs between the state variables v_k and v_{k+1}, and the optimal path from the starting variable v_0 to v_k. Such recursive solution provides an intuitive method for modelling the DP process, however, in practice the problem is usually solved numerically in an iterative manner for efficiency considerations. In addition to the cost matrix, whose elements are corresponding to the optimum cost (S_k), a position matrix, recording the position of the state variables which yield the optimum cost (minimising Eq. (4.13)), is needed. The optimal path can be found by back tracing in the position matrix. The above procedure forms a single iteration, with a computational complexity of $O(nm)$, where n denotes the number of decision stages of the dynamic process.

DP has been reported as an alternative approach to solving the variational problem in active contour like energy functionals [156, 157]. In this thesis, we follow the terminology and notation of the work by Amini and his co-workers [158], and the tube energy can be then expressed as the sum of triple-interaction potentials as follows:

$$
\begin{aligned}
E_{Total}(\boldsymbol{v}_1,\ldots,\boldsymbol{v}_N) &= \sum_{i=2}^{N-1} E_{i-1}(\boldsymbol{v}_{i-1},\boldsymbol{v}_i,\boldsymbol{v}_{i+1}) \\
&= E_1(\boldsymbol{v}_1,\boldsymbol{v}_2,\boldsymbol{v}_3) + E_2(\boldsymbol{v}_2,\boldsymbol{v}_3,\boldsymbol{v}_4) \\
&\quad + \cdots E_{N-2}(\boldsymbol{v}_{N-2},\boldsymbol{v}_{N-1},\boldsymbol{v}_N)
\end{aligned}
\tag{4.14}
$$

where,

$$
E_{i-1}(\boldsymbol{v}_{i-1},\boldsymbol{v}_i,\boldsymbol{v}_{i+1}) = E_{Ext}(\boldsymbol{v}_i) + E_{Int}(\boldsymbol{v}_i) + E_{Con}(\boldsymbol{v}_i)
\tag{4.15}
$$

The optimal value function, S_i, representing the optimal path up to the moving node $\boldsymbol{v}_{i+1}$ can be determined by two adjacent moving nodes on the tube centreline as follows:

$$
S_i(\boldsymbol{v}_{i+1},\boldsymbol{v}_i) = \min_{\boldsymbol{v}_{i-1}}\{S_{i-1}(\boldsymbol{v}_i,\boldsymbol{v}_{i-1}) + E_{i-1}(\boldsymbol{v}_{i-1},\boldsymbol{v}_i,\boldsymbol{v}_{i+1})\}
\tag{4.16}
$$

where the moving node $\boldsymbol{v}_i$ serves as the state variable in the *i*-th decision stage and is only allowed to move within the search space. For fixed values of $\boldsymbol{v}_i$ and $\boldsymbol{v}_{i+1}$, the value of the function $S_i(\boldsymbol{v}_{i+1},\boldsymbol{v}_i)$ is determined by finding the minimum value of the right-hand side of Eq. (4.16), when moving the node $\boldsymbol{v}_{i-1}$ over the space of its possible positions. In each decision stage, the optimal value function incorporates information from three successive moving nodes, and hence, the global optimal solution can be obtained recursively in terms of the consecutive nodes on the centreline. The computational complexity of the DP problem is $O(nm^2)$, which is inefficient for the solution of the tube registration problem when the solution space (*m*) is large. To remedy this problem, we propose the application of a hybrid optimisation strategy, combining local greedy search and dynamic programming, which ensures the global optimality of the solution, while maintaining the efficiency of the proposed algorithm at an acceptable level.

For each moving node on the centreline, *Num* suboptimal locations, associated with the lowest energy in the search space, are firstly determined using the exhaustive search algorithm. The node energies are obtained by the sum of the individual energy functions as defined in Eq. (4.10). The search space is defined as a four voxels width square grid with a step size of 0.2 voxels, which is perpendicular to the tangential direction of the centreline at each moving node (see Fig. 4.8). Next, dynamic programming is applied to determine the global optimal path of the centreline among all possible paths connecting these suboptimal solutions. The above procedure constitutes a single iteration, and the optimisation process terminates when the tube energy does not change with time, or the maximum number of iterations is reached.
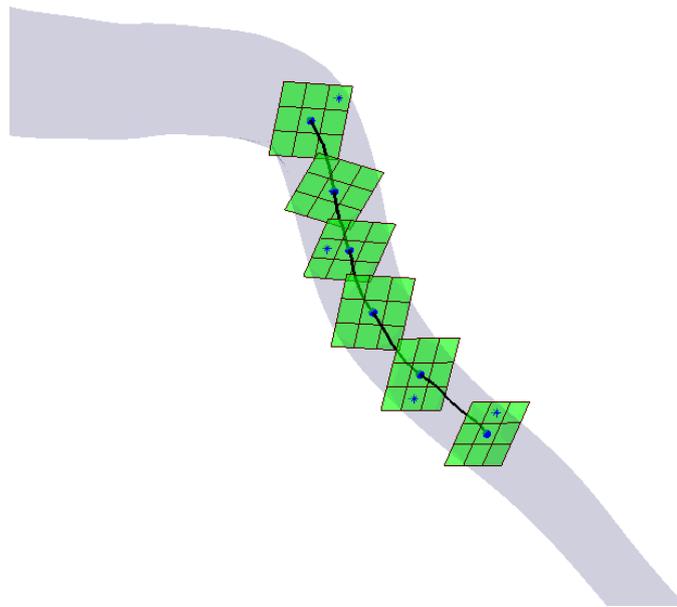
Figure 4.8: 3D schematic diagram illustrating the search space of the tube model registration problem. The optimal location of the central axis is shown in black. The green cross sections represent the search space at each moving node, shown by blue dots. The stars denote the possible movement of each moving node. Note that these grids were displayed in coarse resolution for visualisation purposes.

4.5 Experiments and Discussion

In this section, we apply our method to both synthetic and clinical images to demonstrate the efficiency and accuracy of the proposed method in defining the

centreline and reference vessel surface over the vessel bifurcation. We firstly compare the proposed image-driven energy functional with its volume domain counterparts, i.e., Wong and Chung's method [118] and the tube model proposed by Kang *et al.*, [120], to show the benefits offered by the proposed energy in fitting the tube model to the desired vessel segment. The comparison was carried out using synthetic 3D vascular images, which allow the testing of these energies on various types of vessel segments with known optimal solutions (i.e., ground truth data). Next, we validate our method in clinical CTA images and compare it against the approach reported by Antiga *et al.*, [54], for the determination of the centreline location in a vessel bifurcation.

4.5.1 Experiments on Synthetic Images

The synthetic images were created using the locus of the vessel's central axis and associated cross sections (for simplicity, the circular cross sectional tube model was used in the construction of the synthetic data). The tubes were represented by a binary volume, in both the mesh and volume domains, in order to derive the image-based energy terms for both volume domain methods and the proposed technique.

(a)   (b)   (c)
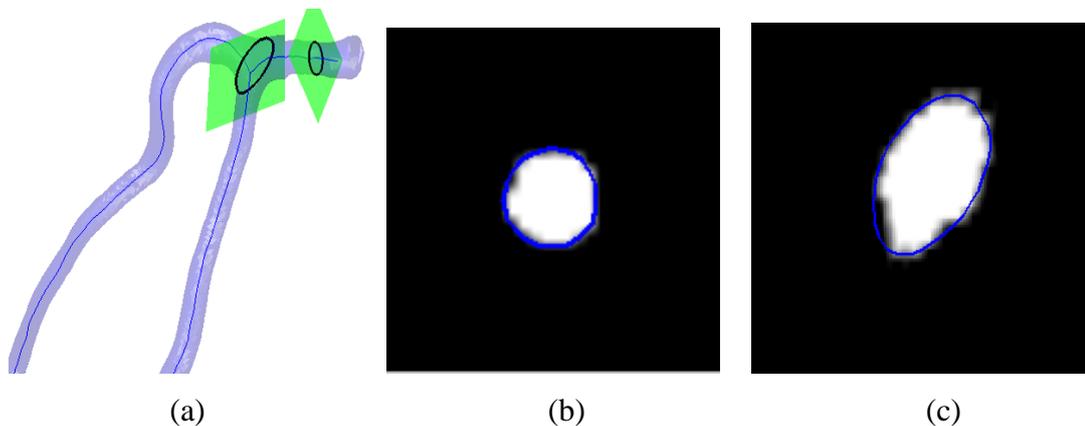
Figure 4.9: Examples illustrating a synthetic tube image. (a) The volume of the tube, (b) An example of the cross sectional image of the tube represented in the voxel domain, where pixels labelled as one represent the tube and zero for the background, and (c) illustrate the cross section taken at a bifurcation (linear interpolation was applied to increase the resolution). The semi-transparent blue structures shown in (a) represent the vessel surface and the green planes are the cross sections. The blue contours shown in (b) and (c) are associated with the intersections between the vessel surface and the cross section.

Fig. 4.9 illustrates examples of synthetic tubular images. The semi-transparent surface represents the boundary of the tube, and the blue curves are the centrelines of the tube. The volume domain representations were illustrated in Figs. 4.9(b) and (c), with cross sectional views, where pixels labelled as one represent vessels and zero for the background. Since the purpose of this experiment is to compare the performance of the aforementioned image-driven energies in measuring the fitness of the tube model at bifurcation areas, the central axis of the tube model was initialised using the optimal solution for all of the methods. In terms of the associated cross sections, they are determined by linear interpolation between two ending cross sections, located prior and distal to the bifurcation, for both Wong and Chung's and Kang *et al.*, methods. We follow the procedure described in Section 4.4.1 to determine the cross sections for the proposed tube model.

In the previously reported methods, the image-driven energies are generally defined by the 'goodness' of the fit between the tube and the vessel of interest in each cross section. This can be formulated either as the fitting error or defined as a degree of overlapping metric, where a unity measurement represents 100% overlapping. To conduct a fair comparison between these metrics, we utilise the fitting error as the 'goodness' measurement for all the energies. Firstly, we present their performance in measuring the 'goodness' of the fitness in a normal (single-branch) vessel cross section. In Wong and Chung's method, the 'goodness' of the fit is measured using the weighted average value calculated based on a set of sampling points. As illustrated in Fig. 4.10(a), the sampling points, shown as stars, are evenly spaced on the concentric circles, with the radius of the outmost circle equal to the radius of the tube model. The values at these sampling points are determined by linear interpolation of the binary volume. The calculation of Kang *et al.*, image energy is illustrated in Fig. 4.10(c), where the image energy is obtained based on the misclassification error by measuring the overlapping rate between the cross sections of the tube (the area within the blue circle, with right-slanted lines) and the vessel. For the proposed image energy metric, which is shown in Fig. 4.10(e), the weighted distance between the vessel's boundary (shown in blue) and

the fitting ellipse (delineated by the red contour) is calculated to measure the fitness

(a)

(b)

(c)

(d)

(e)

(f)
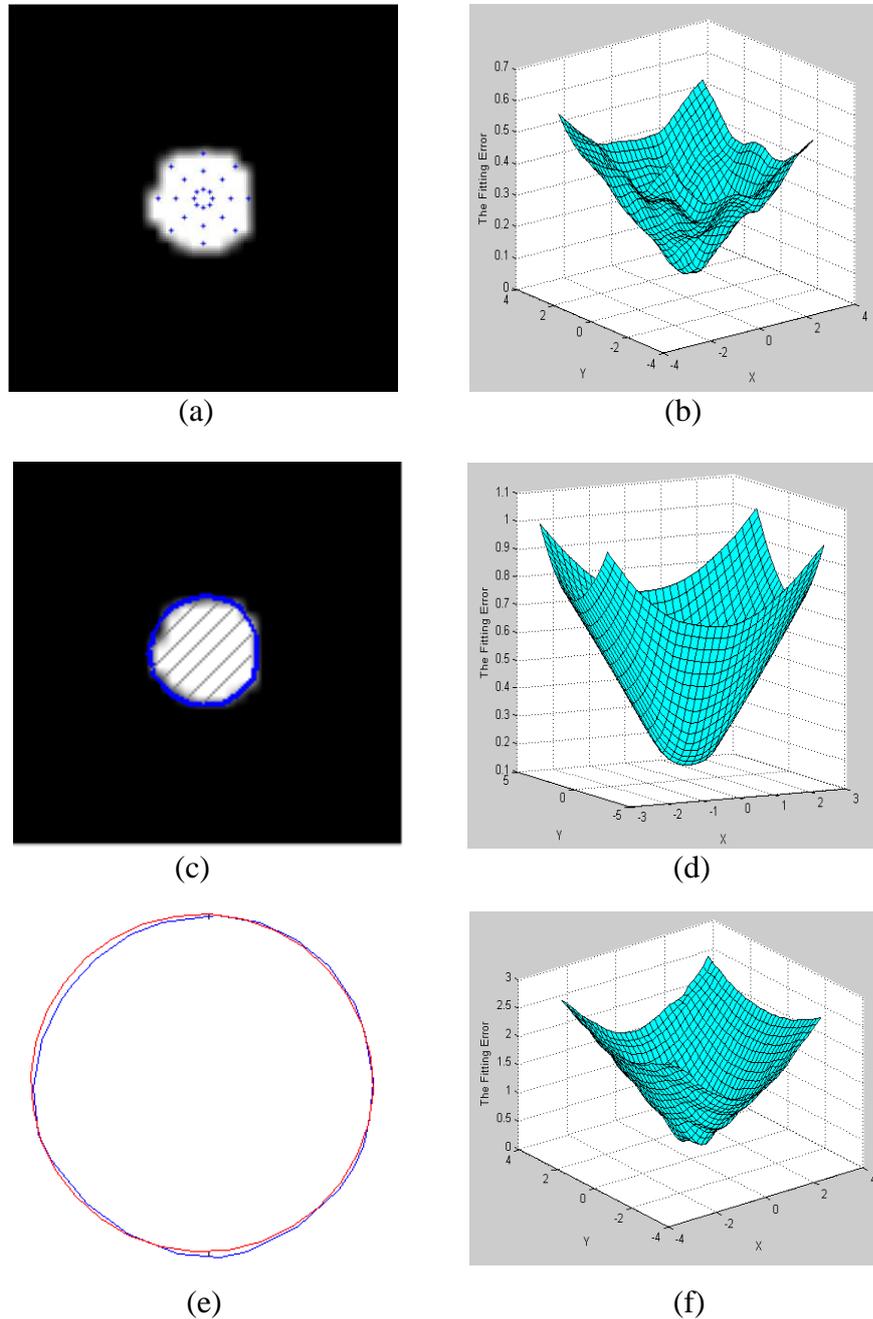
Figure 4.10: Examples illustrating the calculation of image-based energies in a normal vessel cross section using (a) Wong and Chung's energy, (c) Kang *et al*., energy, and (e) The proposed image energy. (b), (d) and (f) delineate the change in the magnitude of the image energies with respect to the distance of the moving node from the optimal solution at the normal vessel segment for Wong and Chung's energy, Kang *et al.,* energy, and the proposed energy formulation, respectively.

between the model and the vessel surface. Figs. 4.10 (b), (d) and (f) depict the change of magnitude of the image-driven energies with respect to the distance of the control point from the optimal position at the bifurcation area. In this experiment, the control point is only allowed to move on a square grid, perpendicular to the tube centreline at each control point. The radius of the grid was set to three voxels, and the grid size was chosen to be 0.2 voxels. Linear interpolation was applied for image upsampling in the calculation of the image energies for the volume domain methods. It can be seen that the fitting error increases as the centre of the tube cross section moves away from the optimal solution, which indicates that all of these algorithms enable accurate registration of the tube model to the vessel boundaries in the normal portion of the vessels.

In Fig. 4.11, we present the previous measurements obtained at the locations of vessel bifurcations. Both Wong and Chung's (Fig. 4.11(b)) energy and Kang *et al*., metric (Fig. 4.11(d)), have a flatten region near the optimal location. This is due to the fact that both of these image-driven energies are based on the degree of overlapping between the tube model and the vessel segment. At a vessel bifurcation, the cross sectional shape of the vessel, as shown in Fig. 4.11(c), deviates from being circular, and thus, the same fitting error is found when the cross section of the tube model is located anywhere within the interior of the vessel area. In this case, the internal energy of the tube model becomes the dominant contributor in these two methods in the vicinity of bifurcations, and thus, the location of the tube is almost entirely determined by this energy term. This may result to erroneous estimation of the reference surface and vessel centrelines, since the internal energy favours a 'straight' tube. On the contrary, only a small number of local minima were identified around the optimal position in the proposed image-driven energy formulation. As shown in Fig. 4.11(e), our image-driven energy generally increases with the distance from the optimal position. Therefore, the proposed model is capable of producing accurate estimation of vessel centrelines and the reference surface. As previously discussed in Section 2.4, image upsampling (interpolation) is usually required for the calculation of the image-based energy in volume domain methods, when the in-plane resolution is insufficient.

(a)

(b)

(c)

(d)

(e)

(f)
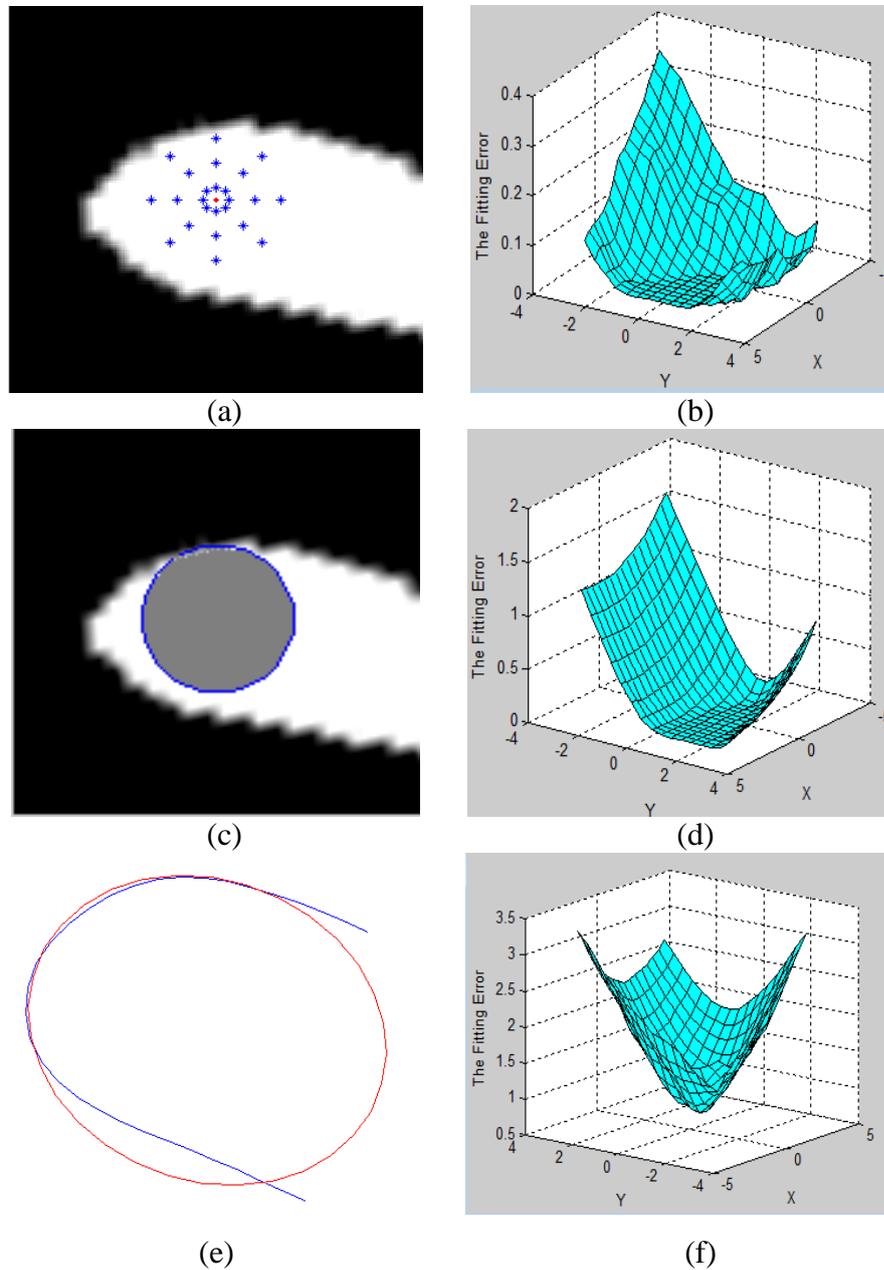
Figure 4.11: Examples illustrating the calculation of image-based energies near the vessel bifurcation using (a) Wong and Chung's energy, (c) Kang *et al.*, energy, and (e) The proposed image energy. (b), (d) and (f) delineate the change in magnitude of image energies with respect to the distance of the moving node from the optimal solution at the bifurcation area for Wong and Chung's energy, Kang *et al.*, energy, and the proposed energy, respectively. The grey area shown in (c) denotes the cross sectional area of the tube located in the interior of the vessel cross section.

Table 4.1: Effect of interpolation methods on image energy

Interpolation Method	Wong and Chung's Energy	Kang's et al., Energy
Nearest neighbour	0.2083	0.1773
Linear	0.0727	0.1600
Cubic	0.0275	0.1629
Cubic spline	0.0043	0.1501

In Table 4.1, we present a comparison of different interpolation methods in the calculation of both Wong and Chung's image-driven energy and the external energy proposed by Kang and his colleagues. The experiment was performed on the vessel cross section shown in Fig. 4.9(b), and the width of the cross section was set to its optimal value. It can be observed from Table 4.1 that Wong and Chung's image-based energy varies in the range of 0.0043 to 0.2083 for different interpolation methods. The maximum value is almost 50 times greater than the minimum, indicating that their method is sensitive to the choice of interpolation scheme. In addition, image upsampling is a computationally expensive operation with the 3D linear interpolation taking approximately 0.4s, while the proposed image energy can be calculated within 3ms for the same cross section. This indicates that the execution time may significantly increase, when the size of the solution space is large.

4.5.2 Experiments on Clinical Images

The same clinical datasets, used previously in Section 3.4, were utilised to quantify the performance of the proposed technique. Two distance metrics, namely, the Mean Square Error (MSE) between the ground truth centreline data and the central axis of the fitting tube, and the MSE between the fitting tube surface and the vessel boundaries, are used to validate the performance of the previously reported algorithms. The tuning parameters of the proposed method are empirically determined based on a training set, which consists of three CT studies randomly

selected from the whole CTA data. In Table 4.2, we show the optimal parameters settings for the proposed algorithm.

Table 4.2: Parameter settings of the tube registration algorithm

Maximum number of iterations, *iter*	20
Number of suboptimal solutions for each node, *Num*	10
Elasticity weight, α	0.2
Stiffness weight, β	0.2
Constrained energy weight, γ	0.15
External energy weight, η	1
Axis constraint, *c*	0.2
Radius of the search space, *rad*	4
Grid size of the searching space, *ds*	0.2
Stop criterion, *eps*	10^{-6}
Circularity criterion for selection of endpoints, *comp*	0.9

Clearly, the choice of parameters in the proposed method can influence its performance. For instance, the elasticity weight α controls the degree of stretching (length) of the centreline. Small values of α would increase the resistance of the centreline curve, while large values may result in shortening of the centreline. The effect of the centreline smoothness (stiffness) parameter β is illustrated in Fig. 4.12, when β is set to relatively small values. The image based energy term dominates the tube fitting process, thus leading to a jagged tube centreline (see Fig. 4.12(a)). Conversely, when β takes large values, the smoothness constraint becomes the major contributor to the total energy, thus resulting in a 'straight' tube, as shown in Fig. 4.12(b).

(a)   (b)
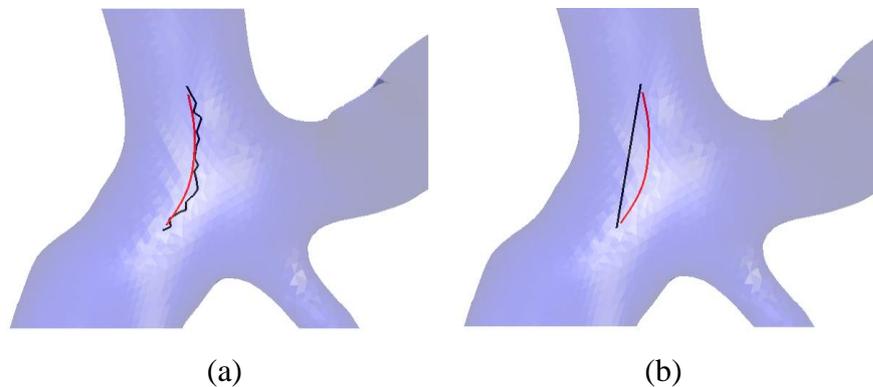
Figure 4.12: The tube centreline obtained by using extreme values for the weights of the smoothness constraints. The tube centrelines obtained by using the standard parameter settings,

listed in Table II, are shown in red. The black curves are the centrelines obtained with (a) low, and (b) high weights for the smoothness (stiffness) parameter β.
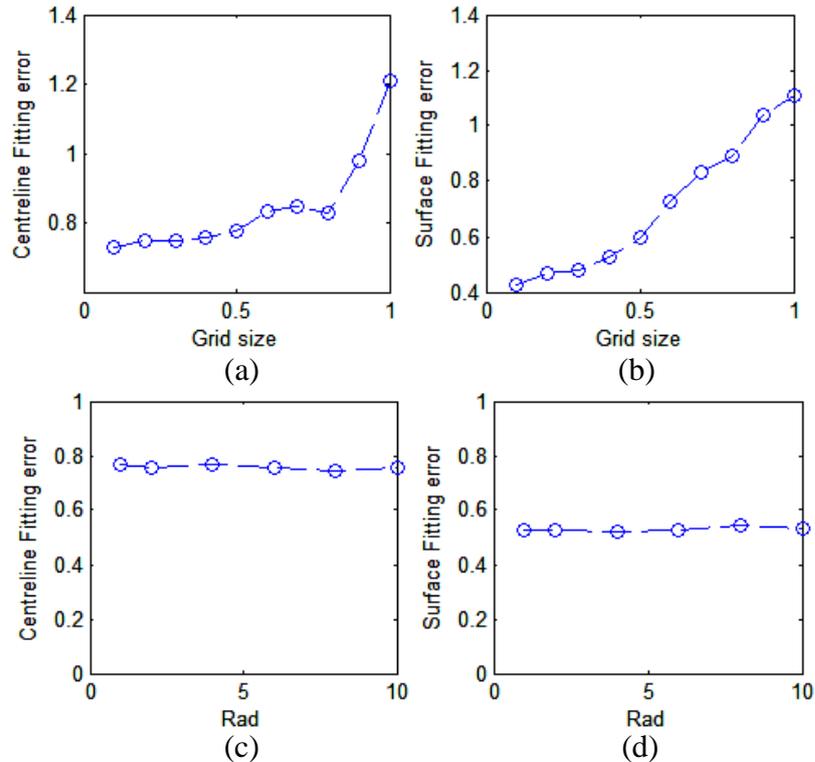
Figure 4.13: Comparison of the tube fitting results in terms of centreline fitting and surface fitting errors. Plots (a) and (b) correspond to the influence of parameter *ds*, while plots (c) and (d) correspond to the influence of parameter *rad*, respectively.

The search space of the proposed method is defined as a square grid, described by the window's radius (*rad*) and step size (*ds*), centred at each moving point along the centreline. We use the vessel segment of Fig. 4.5(a) to evaluate the performance of the tube fitting process with respect to the *rad* and *ds* parameters. It can be seen in Figs. 4.13(a) and (b) that the results change dramatically as the search space step *ds* increases. This is because a small step size for the search space (i.e, finer resolution) allows a larger number of alternative locations for the node to move and thus improves the overall performance. Large values for the step size (i.e., coarser resolution), however, may result in the node making large and potentially erratic movements. On the other hand, the influence of parameter *rad*, as shown in Figs. 4.13(c) and (d), to the fitting results is not as significant, since the minimum value of the local energy for each node is usually found within a small distance from its

initial position. In theory, the choice of parameter *rad* should not introduce significant changes in the results. However, this parameter still needs to be chosen at the appropriate scale, with the optimal value being the width of the vessel, at the vessel bifurcation. The reason for this is that a large value for the parameter *rad* can increase the probability for erroneous movement of the centreline and subsequently increase the computational cost of the optimisation procedure. Since the initial centreline is already near the optimal position, we set the radius of the search space to four voxels in order to improve the efficiency of the proposed algorithm.

(a)

(b)

(c)

(d)
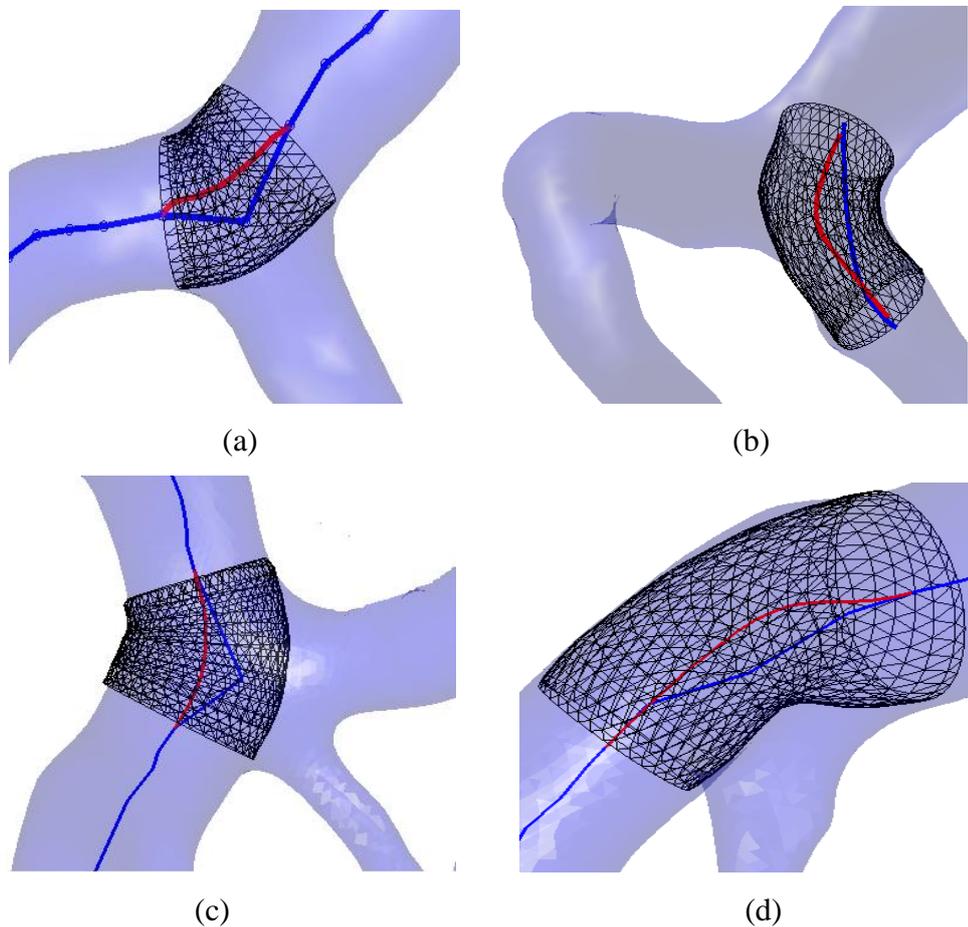
Figure 4.14: Tube registration/fitting results obtained from major bifurcations of coronary arteries: (a) Main vessel in a bifurcation, (b) A highly curved side branch, (c) A complex bifurcation, and (d) A tapering vessel. The semi transparent structure represents the vessel surface (blue surface). The fitting tube is represented by its central axis (in red) and the outer surface (in black) is reconstructed from the cross sections. The blue line denotes the initial centreline estimations.

Fig. 4.14 illustrates the results obtained from the application of the proposed method on four clinical datasets, where the semi-transparent structures (shown in blue) are the arterial lumen surfaces, obtained from the vessel segmentation, and the original centrelines are shown in blue. The central axis of the fitting tube is delineated in red, while the corresponding surface is represented in black. Fig. 4.14(a) shows the fitting of the proposed tube model on the main vessel in the bifurcation. Fig. 4.14(b) illustrates the registration of the fitting tube onto a highly curved side branch. Fig. 4.14(c) depicts the result obtained in the neighbourhood of a complex bifurcation, while the ability of our method in fitting a tapering vessel is demonstrated in Fig. 4.14(d).

Fig. 4.15 depicts the correlation between the tube energy (shown in blue) and the MSE of the fitted centrelines (red curves) with varying parameter settings. Parameter *rad* is fixed to the standard value since it has little influence on the fitting results. We assume that parameters α and β have equal values and evaluate their effect when they take the values of {0.05, 0.2, 0.5}. The grid size parameter takes the values of {0.1, 0.5, 1}, while the remaining parameters are set to their standard values. Note that to facilitate comparison, the values of the MSE and the tube energy were normalised between 0 and 1. By observing the results of Fig. 4.15, we can see that there is a high degree of correlation between the MSE of the centreline and the total tube energy, apart from the cases of Figs. 4.15 (c), (f), (h) and (i). This is because the combination of high smoothness constraints and large search space step size imposes a limit on the possible locations of the tube centreline. Nevertheless, the results provide sufficient evidence that for an appropriate choice of parameters, minimising the energy functional of the entire tube is equivalent to minimising the MSE of the fitting tube, and thus, it is reasonable to terminate the tube registration process, when the tube energy stops decreasing.

111
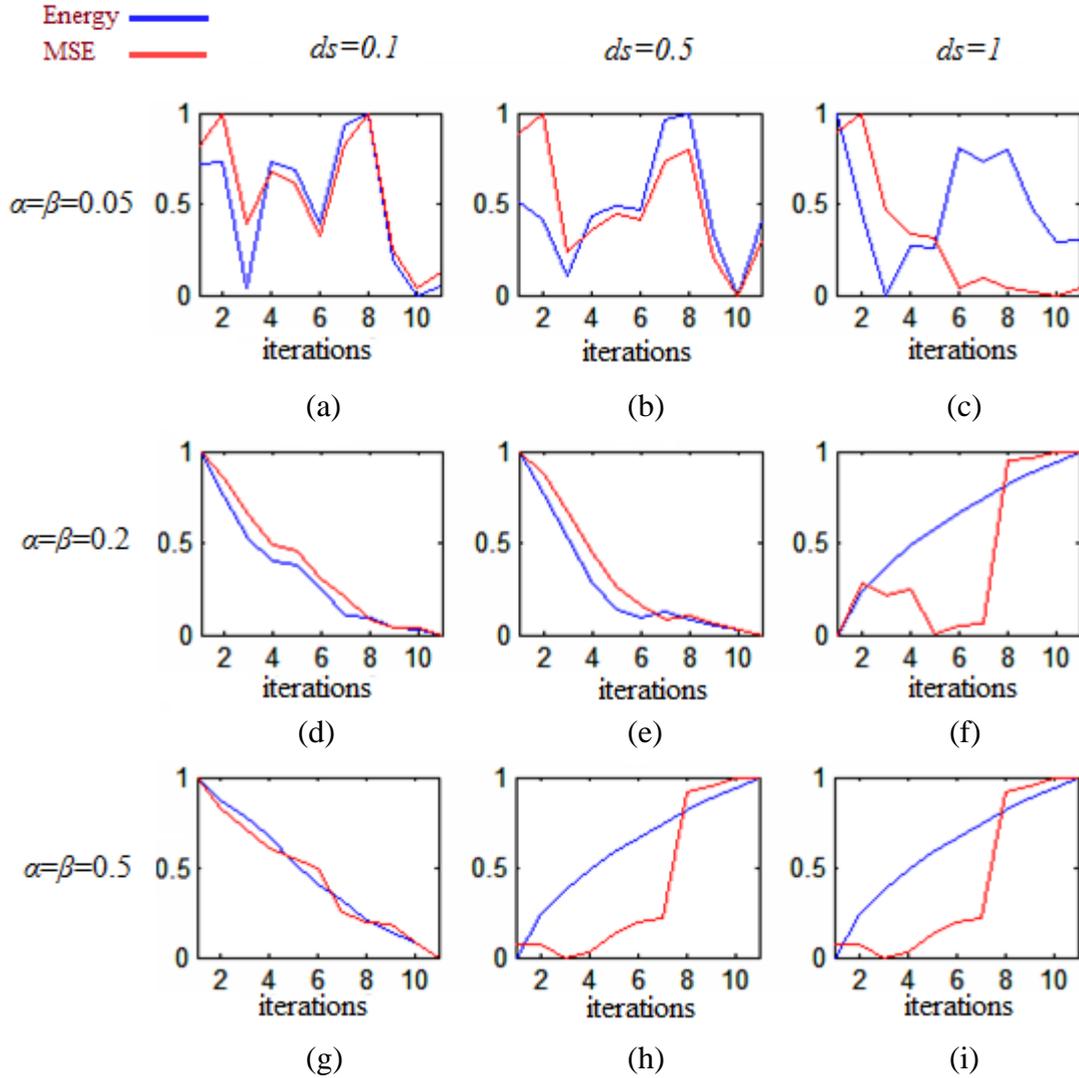
Figure 4.15: Correlation between the tube energy and the MSE of the centreline for different parameter settings. The x-axis of the plot corresponds to the number of iterations, while the y-axis corresponds to the normalised MSE and tube energy values. The tube energy and MSE are plotted in blue and red colours, respectively. Plots (a)-(c) show the MSE and tube energy with parameters *rad*=2, $\alpha=\beta$=0.05, *ds*={0.1, 0.5, 1}, respectively, plots (d)-(f) for *rad*=2, $\alpha=\beta$=0.2, *ds*={0.1, 0.5, 1}, and plots (g)-(i) for parameters *rad*=2, $\alpha=\beta$=0.5, *ds*={0.1, 0.5, 1}, respectively.

We also compared the performance of the proposed method using two tube models, i.e., both circular and elliptical cross sectional tubes, with the centreline extraction algorithm reported by Antiga *et al.*, in the determination of vessel centrelines near bifurcations. For the circular cross sectional model, we initialise the tube in a similar way as in Wong and Chung's method, where the central axis of the tube is defined as the initial centreline of the arteries and the corresponding width of

the cross sections along the centreline is determined by linear interpolation between the diameters estimated at the two endpoints. The tuning parameters for the circular cross sectional tube were determined in the case of the elliptical tube, with the help of the same training set. The VMTK toolkit [159] was used to perform the centreline extraction algorithm in [54], and the 3D slicer [160] was employed to interactively select the end points for each vessel segment.
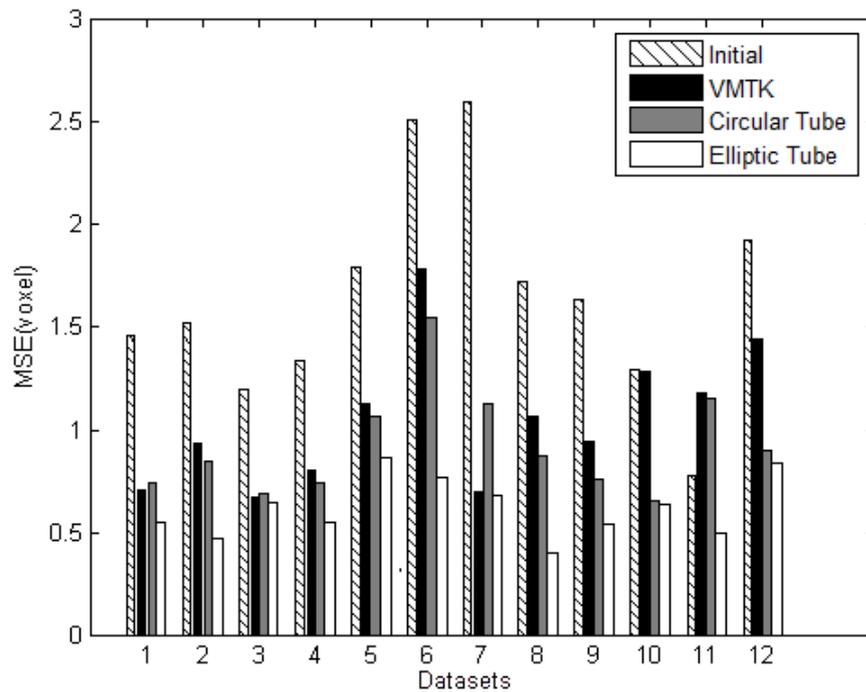
Figure 4.16: Comparison of the centrelines extracted at the vicinity of the bifurcations using the various methods.

As can be observed in Fig. 4.16, the average MSE of the initial centrelines near the bifurcation is approximately 1.71 voxels. The error can be reduced by 36% on average with the Antiga *et al.*, method (the MSE was found at 1.05 voxels). For the proposed algorithm, the circular cross sectional tube has a similar performance to the Antiga *et al.*, method, where the mean MSE for all the test datasets was 0.92 voxels. A further improvement on performance is achieved (i.e., the MSE is reduced by 62.3% on average compared with the initial centrelines), when using the elliptical cross section tube model. The box and whisker plots of the centreline fitting errors of these models for these datasets are presented in Fig. 4.17. It can be

seen that the dispersion of the centreline fitting errors when using the elliptical cross section tube model is the least. This indicates that the proposed elliptical cross section tube model has a higher degree of reproducibility and is more insensitive to the input datasets. The maximum fitting error of our method, when using the elliptic cross section tube model, was found to be equal to 0.86 voxels, which implies that the proposed model is able to estimate the locations of the centrelines over the region of the bifurcation with sub-voxel accuracy.
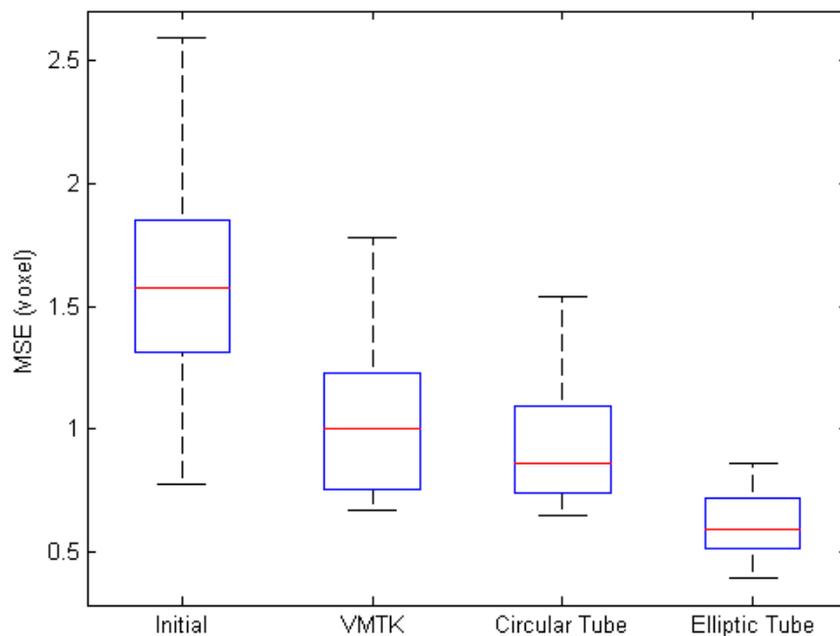
Figure 4.17: Centreline fitting errors for the clinical datasets obtained using the various models.

The proposed approach was implemented in MATLAB (R2010b) on a standard specification PC (Dell Precision T3500, Inter(R) Xeon(R) CPU at 2.67GHz), and the average execution time was found to be 61.3 seconds for fitting each constituent branch of a bifurcation. VMTK, on the other hand, requires roughly 100s to carry out the same process (when implemented using the 3D slicer).

4.6 Conclusions

The luminal area and the centrelines of arteries are the key parameters for performing quantitative analysis of the abnormal coronaries in clinical practice. As

previously discussed in Chapter 2.4, conventional methods were designed for analysis of 'straight' segments of the vessels, and have limitations in defining both the centreline and the reference surface for vessel bifurcations. To address these issues, we propose a dedicated algorithm to simultaneously determine the reference surface and the centreline for arterial bifurcations based on deformable tube model. Followed by outlining the work flow of the proposed algorithm in Section 4.1, we continue with our discussion regarding the initialisation of the tube model in Section 4.2. In Section 4.3, we detailed the construction of the explicit tube model and defined the tube energy that would be used to guide the tube model registration process. This is followed by presentation of the hybrid optimisation scheme, combining local search and dynamic programming, in Section 4.4. Experimental results on both synthetic and clinical datasets were given in Section 4.5.

Compared to state-of-the-art algorithms, the proposed method offers a number of advantages. Firstly, it works directly on the mesh domain, which alleviates the requirement for image upsampling. Secondly, contrary to conventional circular cross sectional tube models, which use linear interpolation to determine the width along the tube, the proposed method estimates the tubular cross sections based on partial information about the vessel surface to be fitted. Specifically, the cross sections of the tube are adaptively estimated by finding the best fitting ellipse to the intersection points (obtained by slicing the vessel surface using the cross section) belonging to the desired constituent branch of the bifurcation. Thirdly, a weighted directional distance metric is employed to measure the fitness between the tube and the vessel of interest in the energy calculation, which facilitates tube registration at the desired location of the bifurcation. In addition, we propose the use of a hybrid optimisation method to minimise the tube energy functional. In particular, a local greedy search is used to determine the initial solutions, which are then optimised through dynamic programming. The proposed optimisation strategy ensures the global optimality of the solution, and permits the incorporation of hard constraints posed to the tube within a natural and direct framework.

The efficiency of our method was demonstrated on both synthetic and clinical datasets, with encouraging results. Experiments on synthetic tube images have

shown that the proposed image-driven energy is more efficient and accurate in measuring the fitness of the tube model at bifurcation areas. For the real clinical data, the proposed method can produce smooth and morphologically correct centrelines and reference surfaces for both the main vessel and the side branch in the region of a bifurcation. The fitting results show that the proposed method leads to an improvement of 62.3% in accuracy (on average), when compared to the original centreline locations.

The application of the proposed tube model allows for the local geometric parameters of the vessel bifurcation to be easily and robustly estimated, which in turn can be used as a starting point for further clinically relevant researches. The next chapter of this thesis (Chapter 5) will be dedicated to the conclusions of this research and present a detailed discussion of possible future directions for this work.

Chapter 5

Conclusions and Future Work

5.1 Introduction

In the final chapter of this thesis, we conclude our current research and make recommendations regarding possible extensions and future directions. The goal of this project has been to develop an automated system for quantitative vascular shape analysis of coronary arteries based on coronary CT images, which would assist the clinician in the diagnosis of coronary heart disease and the reporting of the angiographic results. Existing systems are commonly designed based on single-branch vascular models, thus lacking flexibility in the assessment of atherosclerotic lesions located in bifurcations. The proposed framework, by contrast, is capable of producing reliable reference surface and centreline data for diseased segments of coronary arteries at both normal branch and bifurcation sites, which provides clinically meaningful measurements for quantification of the severity of the stenotic lesions. Additionally, the proposed techniques can be operated in a fully automated fashion, which minimises the interaction from users and reduces the inter- and intra-user variability in the quantification of atherosclerotic lesions. In contrast with conventional techniques based on 2D images, the proposed framework performs the analysis in 3D space, thus eliminating the fore-shortening and out of plane magnification artifacts which are usually encountered in conventional 2D based approaches. The algorithms were integrated in a MATLAB based GUI, which allows for non-technical users to access the full functionality of the proposed system.

The aims of this thesis have been two-fold:

- Firstly, development of an automated segmentation framework dedicated to the extraction of the coronary arteries in 3D contrast enhance coronary

CT images, which defines the physical bounds of the coronary arteries for various clinical tasks.

- Secondly, introduction of a reproducible and robust vascular shape analysis technique to estimate the coronary geometries, based on the resulting segmentation (obtained from Chapter 3). Emphasis has been on the arterial bifurcations, since existing systems are commonly designed based on singe straight branch vessel model and have limitations in accurately estimating coronary geometries in the vicinity of bifurcations.

Followed by this introduction, the remaining sections of this chapter are organised as follows: In section 5.2, we present the conclusions related to the coronary artery segmentation techniques, described in Chapter 3. In section 5.3, the conclusions drawn from the development of the dedicated algorithm for quantitative vascular shape analysis in Chapter 4 are presented. This is followed by presentation of the contributions of this thesis in Section 5.4. Possible extensions and recommendations for future research are given in Section 5.5.

5.2 Coronary Artery Segmentation

In Chapter 3, we intend to develop a fully automated algorithm dedicated to the extraction of the coronary arteries in 3D contrast enhanced CTA images. This chapter is comprised of a series of algorithms towards this end. Specifically, we firstly described an automated pre-processing framework, based on morphological operations and second-order derivative information, which defines the region of interest and creates an initial segmentation of the coronary arteries for subsequent processing. Then, we present a two-stage segmentation algorithm to detect the coronary arteries. In the first stage of the segmentation, the initial segmentation of the coronary arteries was refined using a generalised active contour model. Possible outliers, such as kissing vessel artifacts, are removed in the second stage of the segmentation by using a slice-by-slice correction algorithm. The various of active contours based segmentation techniques were firstly applied to synthetic vascular images to evaluate the performance of the proposed model. The use of the synthetic

images permits generation of vascular images under various conditions, such as varying brightness, noise level and kissing vessels, with pre-determined ground truth segmentation. Experiments on synthetic images have shown that the proposed method is capable of producing satisfactory segmentation in the presence of changing brightness conditions and kissing vessels, by taking both global and local image statistics into account.

In the case of clinical datasets, we compare the proposed technique and active contour model reported by Yang and her colleagues [88] with respect to the manually delineated reference data (i.e., a binary volume data, with voxels labelled as one representing coronary arteries, and zeros for anything else). For both methods, the tuning parameters were determined by using a training set, which consists of three CT volumetric images, randomly selected from the whole 12 datasets. Compared with Yang *et al.*, active contour model, the presented method is less sensitive to the image brightness changes, which is agreed with the conclusions drawn from the synthetic images. It enables the extraction of the major branches of the coronary arterial tree with a voxel-wise error at 0.73 voxels to the manually delineated ground truth data. We also found that the TP and OM rates of the proposed method tend to decrease when approaching the distal and small segments of the arteries. However, clinically significant coronary lesions are usually identified in the main and proximal branches of the arteries [5], which can be well defined by the proposed model. Nevertheless, we can conclude that our technique is able to delineate the vessel boundaries in clinically important coronary segments with a level of variability similar to those obtained through manual segmentation.

In terms of the kissing vessel artifacts, two CT studies were identified with the presence of kissing vessels, and the slice-by-slice correction scheme was applied on the initial segmentation of the arteries. The results demonstrate that the erroneous segmentations caused by kissing vessels have been significantly reduced, with the false positive rates reduced from 294% to 22.8% for those segments distorted by the kissing vessels.

5.3 Quantitative Vascular Shape Analysis

In Chapter 4, we developed an automated algorithm, with particular focus on arterial bifurcations, for the construction of the reference surface and the associated centreline for the diseased portions of the arteries based on dynamic tube model fitting. To this end, we aim to register a deformable tube model to each constituent branch of a bifurcation, which facilitates the estimation of the reference surface and the locations of centreline data. Extensive experiments, based on both synthetic and clinical datasets, have been undertaken to demonstrate the benefits offered by using the proposed technique.

Firstly, we compare the performance of the proposed image-energy with its volume domain counterparts, i.e., the deformable tube energies reported in [118, 120], in measuring the fitness of the tube model at both normal vessel segments and bifurcation locations using synthetic images. Experimental results demonstrated that the proposed image-driven energy outperforms than other energy terms in terms of the efficiency and accuracy, particularly in the vicinity of bifurcations. Hence, the use of the directional distance metric as the image-based energy could potentially improve the overall performance of the proposed in bifurcation regions. For the clinical datasets, twelve coronary CT studies were used to validate the performance of the proposed approach. The evaluation was conducted by comparing the resulting centreline data, obtained using various techniques (described in Section 4.5.2), with the manually annotated gold standard. It was found that, in general, the centreline errors are reduced by an average of 62.3% in the regions of the bifurcations, when compared to the results of the initial solution obtained through the use of mesh contraction method [144]. The maximum fitting error of the estimated centreline to the ground truth data was found at 0.86 voxels. From these observations, we can draw the conclusion that the new method is capable of estimating vessel centrelines and reference surfaces with a high degree of agreement to those obtained through manual delineation. Since presented algorithm is fully automated, which minimises the interactions from the user, it allows for robust and reproducible estimation of the geometrical parameters of the segmented arteries.

5.4 Contributions of the Thesis

The novelties of this research, i.e., those that form the basis of the thesis, are to be found in two main areas, associated with the segmentation and quantitative vascular shape analysis of the coronary arteries in coronary CT images, described in Chapters 3 and 4, respectively. Specifically, the contributions of this thesis are summarised as follows:

- A novel algorithm is proposed for the segmentation of coronary arteries in CT images based on the framework of active contours. In the proposed method, both global and local intensity information are utilised in the energy functional. Particularly, the global term is defined as a normalised cumulative distribution function (CDF), which contributes to the overall active contour energy in an adaptive fashion based on image histogram information, to deform the contour away from local stationary points. The local image energy, on the other hand, enables to deal with varying brightness conditions along the vessel. Experimental results obtained from clinical datasets have shown that this method is capable of extracting the major branches of arterial trees with an average distance of 0.73 voxels to the manually delineated ground truth data. The proposed technique leads to an improvement of 31.8% in accuracy (in terms of the voxel-wise distance to the ground truth data), when compared with segmentation results using the active contour model developed by Yang and her co-workers [88] (Aspects of this work are published in [161-163]).

- A new algorithm is developed to suppress kissing vessel artifacts (i.e., vessels in close proximity to each other), which cannot be distinguished with conventional methods. In particular, a slice-by-slice correction scheme, based on multiple regions competition, is applied to identify and track the kissing vessels throughout the transaxial images of the CTA data. Results on CTA images have shown that by using the proposed slice-by-slice scheme, the erroneous segmentation caused by kissing vessels is dramatically reduced in terms of misclassified voxels (the false positive rate reduces from 294% to

22.8% for those arterial segments affected by kissing vessel artifacts). (Aspects of this work are published in [162, 163]).

- A dedicated algorithm is proposed to perform quantitative vascular shape analysis of the coronary arteries, with focus on vessel bifurcations. Specifically, we propose the estimation of the centreline and the reference surface by registering an elliptical cross sectional tube onto the desired constituent branch in each major bifurcation of the arterial tree. The registration problem is solved through the use of a hybrid optimisation method, combining local greedy search and dynamic programming, which ensures the global optimality of the solution and permits the incorporation of any hard constraints posed to the tube model within a natural and direct framework. This technique works directly on mesh domain, thus alleviating the need for image upsampling, usually required in conventional volume domain approaches. We demonstrate the efficiency and the accuracy of our method on both synthetic images and clinical coronary CTA images. Experimental results show that the proposed method is capable of estimating vessel centrelines and reference surfaces with a high degree of agreement to those obtained through manual delineation. The centreline errors are reduced by an average of 62.3% in the regions of the bifurcations, when compared to the results of the initial solution obtained through mesh contraction algorithm (Aspects of this work are published in [164]).

5.5 Recommendations for Future Work

5.5.1 Improvements Regarding Coronary Segmentation

1. Coupling local shape constraints to the proposed segmentation framework

In this thesis, we extracted the coronary arteries solely based on intensity (appearance) information. This is not sufficient in the presence of coronary pathologies and image artifacts, where intensity features are usually ambiguous. In order to more robustly detect the coronary arteries, we propose the incorporation of shape priors into the proposed segmentation framework. As previously discussed in

Chapter 2, conventional parametric shape models require a large training set to cover the variability of vessels, which is difficult to obtain in practice, and are not straightforward to be encoded/parameterised as a signed distance function [94]. To remedy this problem, it is possible to use non-parametric models to locally describe the shape of current segmentations. Qian and his colleagues proposed a non-parametric vesselness metric, which is based on the analysis of local intensity patterns centred at each voxel, offering an alternative for the detection of vascular geometries in medical images [165]. By introducing the shape information using Qian *et al.*, vesselness measurement, the active contour would expand quickly when it is located within a vessel, on the other hand, when the shape of the current segmentation strongly deviates from being vascular, the shape prior would provide a penalised force to pull it back. Hence, through the combination of the shape information of the current segmentation, the accuracy of the presented segmentation framework could be potentially improved with respect to the presence of spurious intensity features.

2. Clinical validation of the proposed segmentation framework with invasive standard

In this research, the accuracy and capability of the proposed system was quantified by comparing the segmented arteries with manual delineation, which lacks validation with an invasive standard such as cardiac catheterisation. In order to determine the true clinical applicability of the proposed framework, a comparison of the diagnostic results obtained through the proposed algorithms with the actual diagnosis based on standard invasive procedure is required to carry out in a per-vessel and per-patient basis.

5.5.2 Improvements for Quantitative Shape Analysis

The tube registration problem, discussed in Chapter 4.4, was solved in a 2D cross-section basis, where the tube energy was minimised at each cross section in turn, and by allowing the model to move as a whole to fit the vessel surface through an iterative process. The robustness of the proposed algorithm can be further improved, if the full 3D information about the vessel is utilised in the registration

process. To this end, further work will be directed towards constructing the tube model by a series of short tubular segments (i.e., a generalised cylinder with varying diameters), which allows more robust and accurate approximation of vessel geometries [77-79]. In order to ensure the smoothness of the estimated reference surface, we propose that the tube model is designed in such a way so that the adjacent tube segments are overlapping, as shown in Fig. 5.1. Hence, the optimal configurations for each tube segment can be determined by simultaneously minimising the fitting error between the current tube segment and the desired vessel surface, and the inter-tube differences within the overlapping area, which maintains the global smoothness of the solution.
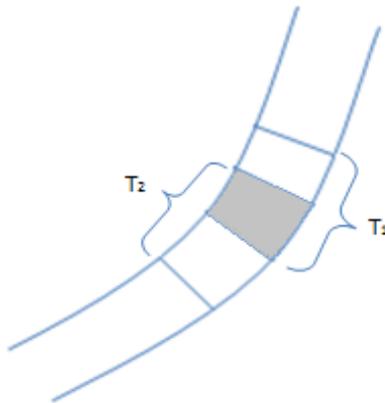
Figure 5.1: 2D schematic diagram showing the construction of a dynamic tube model by using tubular segments. T_1 and T_2 denote two successive tubular segments, respectively, and the overlapping area between these two tubes is shown in grey.

5.5.3 Detection of Vulnerable Plaques

Recent studies suggest that vulnerable plaques, mainly made of fibrotic components, are particularly unstable and prone to rupture, and thus, there is a higher likelihood that they may lead to further complications, such as heart attack and stroke. In contrast with calcified plaques, which usually exhibit hyper-densities in CT angiographies, fibrotic plaques (also known as soft plaques) cannot always be discriminated from the arterial lumen due to the absence of strong intensity features. Hence, there is a great interest in developing dedicated algorithms for quantification and characterisation of soft plaques in coronary arteries. Textural features, which

are powerful descriptors in the modelling of local image appearance, have been reported to differentiate different tissues in CT images [166]. Thus, the capability and flexibility of existing approaches, relying on (first-order) intensity features alone, could be potentially improved by taking both of these sets of features into account. Instead of using conventional deterministic methods, which may lead to inaccurate estimation, when the pre-assumed criterion does not hold, we propose employing particle filter based methods, allowing for the incorporation of multiple hypotheses in a natural and straightforward framework, for detecting the presence of soft plaques.

5.5.4 Quantification of Functional Significance of Atherosclerotic Lesions

Various clinical studies indicate that although coronary CTA has particular strengths in excluding the presence of significant coronary diseases, it performs less well in terms of its positive predictive accuracy, often resulting in unnecessary catheterisation. This is mainly because coronary occlusions, with no significant effects on the function of coronary circulation, cannot be distinguished from those associated with a higher risk of developing myocardial ischemia by means of static coronary CT images. Fractional Flow Reserve (FFR), a technique measuring pressure differences between a stenotic artery and its normal proximal segments, is the current golden standard for diagnosis of myocardial ischemia [167]. Complications associated with the conventional invasive FFR procedure, however, restrict its application to a certain groups of patients with hypertension and hypercholesterolemia. Recent advances in image-based blood flow analysis have provided a non-invasive alternative for the assessment of the functional significance of the coronary lesions. Preliminary research suggested that diagnostic results obtained from virtual FFR based on coronary CT angiograms have a high degree of correlation with conventional FFR [168].

Through the application of Computational Fluid Dynamics (CFD) in simulating blood flow in the cardiovascular system, haemodynamic parameters, such as velocity, stress/pressure as well as shear stress distribution, can be estimated *in silicon*, which could provide the clinician with essential information in determining

the associated risk for a patient. Functional information, obtained from a patient-specific geometric model of the artery, may potentially enhance the diagnostic capability of standard coronary CT in high risk patients, without changing the imaging protocol. The framework presented in this thesis allows the construction of patient-specific models of coronary arteries, which in turn could be used as a starting point for analysing the fluid mechanical properties of blood flow in the coronary circulation.

Bibliography:

[1]   E. N. Marieb and K. N. Hoehn, *Human Anatomy and Physiology*, 8 ed. Redwood City, California, USA: Pearson Education, 2010.

[2]   F. H. Netter, *Atlas of Human Anatomy 2nd Edition*. King of Prussia, PA, USA: Rittenhouse Book Distributors Inc, 1997.

[3]   WHO. (2010, Coronary Heart Disease. Available: http://www.who.int/en/.

[4]   WHO.   Atherosclerosis   [Online].   Available: http://www.nhlbi.nih.gov/health/dci/index.html

[5]   P. Pavone, M. Fioranelli, and D. A. Dowe, *CT Evaluation of Cornary Artery Disease*, 1 ed. New York, NY, USA: Springer Press, 2008.

[6]   T. M. Bashore*, et al.*, "American College of Cardiology/Society for Cardiac Angiography and Interventions Clinical Expert Consensus Document on cardiac catheterization laboratory standards. A report of the American College of Cardiology Task Force on Clinical Expert Consensus Documents," *Journal of the American College of Cardiology* vol. 37, pp. 2170-2214, 2001.

[7]   J. N. Karbhase, S. R. Panday, G. B. Parulkar, and M. D. Kelkar, "Complications of Cardiac Catheterization Needing Emergency Surgery," *Journal of Postgraduate Medicine,* vol. 30, pp. 237-240, 1984.

[8]   F. J. Rybicki*, et al.*, "Initial Evaluation of Coronary Images from 320 Detector Row Computed Tomograhpy," *International Journal of Cardiovascular Imaging,* vol. 24, pp. 535-546, 2008.

[9]   E. M. Hsiao, F. J. Rybicki, and M. Steigner, "CT Coronary Angiography: 256-Slice and 320 Detector Row Scanners," *Current Cardiology Reports,* vol. 12, pp. 68-75, 2010.

[10]   M. Mahesh and D. D. Cody, "Physics of Cardiac Imaging with Multiple Row Detector CT," *Radio Graphics,* vol. 27, pp. 1495-1509, 2007.

[11]   A. Kanitsar, R. Wegenkittl, D. Fleischmann, and M. E. Groller, "Advanced Curved Planar Reformation: Flattening of Vascular Structures," in *Proc. of The 2003 IEEE Visualization* Washington US, 2003, pp. 43-50.

[12]   A. Kanitsar, D. Fleischmann, R. Wegenkittl, P. Felkel, and M. E. Groller, "CPR - Curved Planar Reformation," in *Proc. of The 2002 IEEE Visualization*, Boston MA USA, 2002, pp. 37-45.

[13]   C. Kirbas and F. Quek, "A Review of Vessel Extraction Techniques and Algorithms," *Association for Computing Machinery Computing Survery,* vol. 36, pp. 81-121, 2004.

[14]   D. Lesage, E. D. Angelini, I. Bloch, and G. F. Lea, "A Review of 3D Vessel Lumen Segmentation Techniques: Models, Features and Extraction Schemes," *Medical Image Analysis,* vol. 13, pp. 819-845, 2009.

[15]   L. D. Cohen and R. Kimmel, "Global Minimum for Active Contour Models: A Minimal Path Approach," *International Journal of Computer Vision,* vol. 24, pp. 57-78, 1997.

[16]   E. W. Dijkstra, "A Note on Two Problems in Connection with Graphs," *Numerische Mathematik,* vol. 11, pp. 269-271, 1959.

[17]   U. Montanari, "On the Optimal Detection of Curves in Noisy Pictures," *Communications of the ACM,* vol. 14, pp. 335-345, 1971.

[18]   M. A. Fischler, J. M. Tenenbaum, and H. C. Wolf, "Detection of Roads and Linear Structures in Low Resolution Aerial Imagery using a Multisource Knowledge Integration Technique," *Computer Graphics and Image Processing,* vol. 15, pp. 201-223, 1981.

[19]   S. Chandran, T. Meajima, and S. Miyazaki, "Global Minima via Dynamic Programming: Energy Minimizing Active Contours," in *Proc. of Geometric Methods in Computer Vision*, San Diego, 1991, pp. 391-402.

[20]   J. A. Sethian, "Fast Marching Methods," *Society for Industrial and Applied Mathematics,* vol. 41, pp. 199-235, 1999.

[21]   J. A. Sethian, "A Fast Marching Level Set Method for Monotonically Advancing Fronts," in *Proc. of the National Academy of Sciences*, 1996, pp. 1591-1595.

[22]   Y. Samara*, et al.*, "Automatic Calculation of the Ceterline of the Human Colon on CT Images," *Academic Radiology,* vol. 6, pp. 352-359, 1999.

[23]   Y. Ge, D. Stelts, and D. Vining, "Computing the Centerline of a Colon," in *Proc. of Visualization in Biomedical Computing*, 1996, pp. 449-454.

[24]   T. Saito and J. Toriwaki, "New Algorithm for Euclidean Distance Transformation of an N Dimensional Digitized Picture with Applications," *Pattern Recognition,* vol. 27, pp. 1151-1565, 1994.

[25]   M. Wan, D. Frank, and A. Kaufman, "Distance Field Based Skeletons for Virtual Navigation," in *Conference on Visualization'01*, 2001, pp. 239-245.

[26]   M. Wan*, et al.*, "Automatic Centreline Extraction for Virtual Colonoscopy," *IEEE Transacation on Medical Imaging,* vol. 21, pp. 1450-1460, 2002.

[27]   I. Bitter*, et al.*, "CEASAR: A Smooth, Accurate and Robust Centerline Extraction Algorithm," in *Proc. of Visualization*, 2000, pp. 45-52.

[28]   I. Bitter, A. Kaufman, and M. Sato, "Penalized Distance Volumetric Skeleton Algorithm," *IEEE Transactions on Visualization and Computer Graphics,* vol. 3, pp. 195-206, 2001.

[29]   M. Sato, I. Bitter, M. Bender, A. Kaufman, and M. Nakajima, "TEASAR: Tree-Structure Extraction Algorithm for Accurate and Robust Skeletons," in *Proc. of Pacific Graphics*, 2000, pp. 281-289.

[30]   G. Jiang and L. Gu, "An Automatic and Fast Centreline Extraction Algorithm for Virtual Colonoscopy," in *Proc. of IEEE Engineering in Medicine and Biology 27th Annual Conference*, Shanghai, China, 2005, pp. 1-4.

[31]   C. Lorenz, I. C. Garlsen, T. M. Buzug, C. Fassnacht, and J. Weese, "Multi-Scale Line Segmentation with Automatic Estimation of Width, Contrast and Tangential Direction in 2D and 3D Medical Images," in *Lecture Notes in Computer Science* vol. 1205, ed: SpringLink, 1997, pp. 223-242.

[32]   Y. Sato, S. Nakajima, and N. Shiraga, "3D Multi-scale Line Filter For Segmentation and Visualization of Curvilinear Structures in Medical Images," *Medical Image Analysis,* vol. 2, pp. 143-168, 1998.

[33]   A. F. Frangi, W. J. Niessen, K. L. Vincken, and M. A. Viergever, "Multiscale Vessel Enhancement Filtering," in *Proc. of Medical Image Computing and Computer-Assisted Intervention, MICCAI'98*, Berlin, Germany, 1998, pp. 130-137.

[34]   O. Wink, A. F. Frangi, B. Verdonck, M. A. Viergever, and W. Niessen, "3D MRA Coronary Axis Determination Using a Minimum Cost Path Approach," *Magetic Resonance in Medicine,* vol. 47, pp. 1169-1175, 2002.

[35]   O. Wink, W. Niessen, and M. A. Viergever, "Multiscale Vessel Tracking," *IEEE Transacation on Medical Imaging,* vol. 23, pp. 130-133, 2004.

[36]   J. N. Kaftan, H. Tek, and T. Aach, "A Two Stage Approach for Fully Automatic Segmentation of Venous Vascular Structures in Liver CT Images," in *Medical imaging 2009: Image Processing* vol. 7259, J. P. W. Pluim and B. M. Dawant, Eds., ed: SPIE, 2009.

[37]   M. A. Gulsun and H. Tek, "Robust Vessel Tree Modeling," in *Medical image computing and Computer-Assisted Intervention – MICCAI 2008*

Lecture Notes in Computer Science. vol. 5241/2008, ed: SpringerLink, 2008, pp. 602-611.

[38]   M. Pechaud, G. Peyre, and R. Keriven, "Extraction of Vessels Networks Over an Orientation Domain " in *Proc. of IEEE International Conference on Computer Vision and Pattern Recognition*, 2009, pp. 336-342.

[39]   H. E. Cetingul, M. Gulsun, and H. Tek, "A Unified Minimal Path Tracking and Topology Characterization Approach for Vascular Analysis," in *Proc. of the 5th international conference on Medical imaging and augmented reality* 2010, pp. 11-20.

[40]   T. Deschamps and L. D. Cohen, "Fast Extraction of Minimal Paths in 3D Images and Applications to Virtual Endoscopy," *Medical Image Analysis,* vol. 5, pp. 281-299, 2001.

[41]   D. Adalsteinsson and J. Sethian, "A Fast Level Set Method for Propagating Interfaces," *Journal of Computational Physics,* vol. 118, pp. 269-277, 1995.

[42]   E. Rouy and A. Tourin, "A Viscosity Solution Approach to Shape from Shading," *SIAM Journal on Numerical Analysis,* vol. 29, pp. 867-884, 1992.

[43]   P. Dupuis and J. Oliensis, "An Optimal Control Formulation and Related Numerical Methods for a Problem in Shape Reconstruction," *Annals of Applied Probability,* vol. 4, pp. 287-346, 1994.

[44]   D. Chen*, et al.*, "A Tree Branch Searching Multiresolution Approach to Skeletonization for Virtual Endoscopy," in *Proc. of SPIE Medical Imaging*, 2000, pp. 726-734.

[45]   T. Deschamps and L. D. Cohen, "Fast Surface and Tree Structure Extraction of Vascular Objects in 3D Medical Images," in *Proc. of Fifth International Conference on Curves and Surfaces*, Saint Malo, 2002, pp. 10-18.

[46]   R. Cardenes, H. Bogunovic, and A. F. Frangi, "Fast 3D Centreline Computation For Tubular Structures by Front Collapsing and Fast Marching," in *Proc. of IEEE 17th International Conference on Image Processing*, 2010, pp. 4109-4112.

[47]   R. V. Uitert and I. Bitter, "Subvoxel Precise Skeletons of Volumetric Data based on Fast Marching Methods," *Medical Physics,* vol. 34, pp. 627-638, 2006.

[48]   S. Young, V. Pekar, and J. Weese, "Vessel Segmentation for Visualization of MRI with Blood Pool Contrast Agent," in *Lecture Notes in Computer Science* vol. 2208, ed: SpringerLink, 2001, pp. 491-498.

[49]   J. Mille and L. D. Cohen, "Deformable Tree Models for 2D and 3D Branching Structures Extraction," in *Proc. of 2009 IEEE Computer Society Conference on Computer Vision and Pattern Recognition Workshops*, Miami, FL, USA, 2009, pp. 149-156.

[50]   V. Caselles, R. Kimmel, and G. Sapiro, "Geodesic Active Contours," *International Journal of Computer Vision,* vol. 22, pp. 61-79, 1997.

[51]   T. F. Chan and L. A. Vese, "Active Contours Without Edges," *IEEE Transacation on Image Processing,* vol. 10, pp. 266-277, 2001.

[52]   H. Li and A. Yezzi, "Vessels as 4-D Curves: Global Minimal 4-D Paths to Extract 3-D Tubular Surfaces and Centerlines " *IEEE Transacations on Biomedical Engineering,* vol. 26, pp. 1213-1223, 2007.

[53]   H. Li and A. Yezzi, "Vessels as 4D Curves:Global Minimal 4D Paths to Extract 3D Tubular Surfaces," in *Proc. of IEEE Conference of Computer Vision and Pattern Recognition*, 2006, pp. 82-91.

[54]   L. Antiga, B. Ene-Iordache, and A. Remuzzi, "Centerline Computation and Geometric Analysis of Branching Tubular Surfaces With Application to Blood Vessel Modeling," in *Proc. of The11th International Conference in Central Europe on Computer Graphics, Visualization and Computer Vision 2003*, Campus Bory, Plzen - Bory, Czech Republic, 2004, pp. 11-18.

[55]   F. Benmansour, L. D. Cohen, M. W. K. Law, and A. C. S. Chung, "Tubular Anisotropy for 2D Vessels Segmentation " in *Proc. of IEEE Conference on Computer Vision and Pattern Recoginition*, 2009, pp. 2286-2293.

[56]   F. Benmansour and L. D. Cohen, "Tubular Structure Segmentation Based on Minimal Path Method and Anisotropic Enhancement " *International Journal of Computer Vision,* vol. 92, pp. 192-210, 2010.

[57]   M. W. K. Law and A. C. S. Chung, "Three Dimensional Curvilinear Structure Detection using Optimally Oriented Flux," in *Proc. of the 10th European conference on computer vision*, Berlin, Heidelberg, 2008, pp. 368-382.

[58]   D. L. Chopp, "Replacing Iterative Algorithms with Single Pass Algorithms," *Proceedings of the National Academy of Science of the USA,* vol. 98, pp. 10992-10993, 2001.

[59]   F. Bornemann and C. Rasch, "Finite-Element Discretization of Static Hamilton-Jacobi Equations based on a Local Variational Principle " *Computing and Visualization in Science,* vol. 9, pp. 57-69, 2006.

[60]   Q. Lin, "Enhancement, Extraction and Visualization of 3D Volume Data," Phd, Department of Electrical Engineering, Linkopings University, Linkoping, 2003.

[61]   D. Mueller and A. Maeder, "Robust Semi-Automated Path Extraction for Visualising Stenosis of the Coronary Arteries " *Compterized Medical Imaging and Graphics,* vol. 32, pp. 463-475, 2008.

[62]   T. Deschamps, "Curve and Shape Extraction with Minimal Path and Level-Sets techniques. Applications to 3D Medical Imaging," Ph.D., University of Paris Dauphine, Paris, 2001.

[63]   M. S. Arulampalam, S. Maskell, N. Grodon, and T. Clapp, "A Tutorial on Particle Filters for Online Nonlinear NonGaussian Bayesian Tracking," *IEEE Transacation on Signal Processing,* vol. 50, pp. 174-189, 2002.

[64]   G. Welch and G. Bishop, "An Introduction to the Kalman Filter," 1995.

[65]   R. E. Kalman, "A New Approach to Linear Filtering and Prediction Problems," *Journal of Basic Engineering,* vol. 82, pp. 35-45, 1960.

[66]   R. E. Kalman and R. S. Bucy, "New Results in Linear Filtering and Prediction Theory," *Journal of Basic Engineering,* vol. 83, pp. 95-107, 1996.

[67]   J. Carpenter, P. Clifford, and P. Fearnhead, "Improved Particle Filter for Nonlinear Problems," *IEE Proceeding Radar, Sonar & Navigation,* vol. 146, pp. 2-7, 1999.

[68]   D. Crisan, P. D. Moral, and T. J. Lyons, "Non Linear Filtering using Branching and Interacting Particle System," *Markov Processes Related Fields,* vol. 5, pp. 293-319, 1999.

[69]   P. D. Moral, "Non-linear filtering: Interacting particle solution," *Markov Processes Related Fields,* vol. 2, pp. 555-580, 1997.

[70]   A. Doucet, J. d. Freitas, and N. Gordon, *Sequential Monte Carlo Methods in Practice*. New York, USA: Springer Verlag, 2001.

[71]   N. Bergman, "Recursive Bayesian estimation: Navigation and tracking applications," Ph.D, Linkoping University, Linkoping, 1999.

[72]   C. Florin, N. Paragios, and J. Williams, "Particle Filters, a quasi-Monte-Carlo-Solution for Segmentation of Coronaries," *Medical Image Computing and Computer-Assisted Intervention – MICCAI 2004,* vol. 8, pp. 246-253, 2005.

[73]   C. Florin, N. Paragios, and J. Williams, "Globally Optimal Active Contour, Sequential Monte-Carlo and On-line Learning for Vessel Segmentation," in *Proc. of European Conference on Computer Vision*, 2006, pp. 476-489.

[74]   B. Appleton and C. Sun, "Circular Shortest Paths by Branch and Bound," *Pattern Recognition,* vol. 36, pp. 2513-2510, 2003.

[75]   H. Shim, D. Kwon, I. D. Yun, and S. U. Lee, "Robust Segmentation of Cerebral Arterial Segments by a Sequential Monte Carlo Method: Particle Filtering," *Computer Methods and Programs in Biomedicine,* vol. 84, pp. 135-145, 2006.

[76]   H. Shim, I. D. Yun, and S. U. Lee, "Tracking of Cerebral Arterial Segment by Particle Filtering in CT Angiography," in *World Congress on Medical Physics and Biomedical Engineering 2006*, 2007, pp. 4171-4174.

[77]   M. Schaap, I. Smal, C. T. Metz, T. v. Walsum, and W. Niessen, "Bayesian Tracking of Elongated Structures in 3D Images," in *Proc. of Information Processing in Medical Imaging*, 2007, pp. 74-85.

[78]   M. Schaap*, et al.*, "Bayesian Tracking of Tubular Structures and its Application to Carotid Arteries in CTA," *Medical Image Computing and Computer-Assisted Intervention – MICCAI 2007,* pp. 562-570, 2007.

[79]   S. Worz, W. J. Godinez, and K. Rohr, "Probabilistic Tracking and Model based Segmentation of 3D Tubular Structures," in *Algorithmen — Systeme — Anwendungen Proceedings des Workshops* H.-P. Meinzer, Ed., ed Berlin Heidelberg: Springer 2009, pp. 41-45.

[80]   S. Worz and K. Rohr, "Segmentation and Quantification of Human Vessels using a 3D Cylindrical Intensity Model," *IEEE Transacation on Image Processing,* vol. 18, pp. 1994-2004, 2007.

[81]   D. Lesage, E. D. Angelini, I. Bloch, and G. Funka-Lea, "Medial based Bayesian Traking for Vascular Segmentation: Application to Coronary Arteries in 3D CT Angiography," in *Proc. of IEEE International Symposium on Biomedical Imaging*, 2008, pp. 268-271.

[82]   F. Zhao, R. Bhotika, P. R. S. Mendonca, N. Krahnstoever, and J. V. Miller, "Adaptive Intensity Models for Probabilistic Tracking of 3D Vasculature " in *2010 IEEE International Symposium on Biomedical Imaging: From Nano to Macro*, Rotterdam, 2010, pp. 41-44.

[83]   H. E. Cetingul, G. Plank, N. Trayanova, and R. Vidal, "Stochastic Tractography in 3-D Images via Nonlinear Filtering and Spherical Clustering," in *Proc. of Probabilistic Models for Medical Image Analysis (PMMIA'09) Workshop at MICCAI'09*, London, UK, 2009, pp. 114-120.

[84]   D. Geman and B. Jedynak, "An Active Testing Model for Tracking Roads in Stellite Images," *IEEE Transacation on Pattern Analysis and Machnie intelligence,* vol. 18, pp. 1-14, 1996.

[85]   M. Kass, A. Witkin, and D. Terzopoulos, "Snakes: Active Contour Models," *International Journal of Computer Vision,* pp. 321-331, 1998.

[86]   S. Osher and R. Fediww, *Level Set Methods and Dynamic Implicit Surface*. New York, NY, USA: Springer Press, 1999.

[87]   S. Kichenassamy, A. Kumar, P. Olver, A. Tannenbaum, and A. Yezzi, "Gradient Flows and Geometric Active Contour Models," in *Proc. of Fifth International Conference on Computer Vision*, Boston, 1995, pp. 810-815.

[88]   Y. Yang, A. Tannenbaum, D. Giddens, and A. Stillman, "Automatic Segmentation of Coronary Arteries using Bayesian Driven Implicit Surfaces," in *Proc. of 4th IEEE International Symposium on Biomedical Imaging*, 2007, pp. 189-192.

[89]   Y. Chen*, et al.*, "Using Shape Priors in Geometric Active Contours in a Variational Framework," *International Journal of Computer Vision,* vol. 50, pp. 315-328, 2002.

[90]   A. Tsai, A. Yezzi, and A. S. Willsky, "Curve Evolution Implementation of the Mumford Shah Functional for Image Segmentation, Denosing, Interpolation and Magnification," *IEEE Transacation on Image Processing,* vol. 10, pp. 1169-1186, 2001.

[91]   M. E. Leventon, W. E. L. Grimson, and O. Faugeras, "Statistical Shape Influence in Geodesic Active Contours," in *Proc. of 5th IEEE EMBS International Summer School on Biomedical Imaging*, USA, 2002, pp. 8-18.

[92] M. Turk and A. Pentland, "Eigenfaces for Recognition," *Journal of Cognitive Neuroscience,* vol. 3, pp. 71-86, 1991.

[93] D. Cremers, S. J. Osher, and S. Soatto, "Kernel Density Estimation and Intrinsic Alignment for Shape Priors in Level Set Segmentation," *International Journal of Computer Vision,* vol. 69, pp. 335-351, 2006.

[94] D. Nain, A. Yezzi, and G. Turk, "Vessel Segmentation Using a Shape Driven Flow " in *Proc. of Medical Image Computing and Computer-Assisted Intervention – MICCAI 2004*, 2004, pp. 51-59.

[95] A. Gooya*, et al.*, "A Variational Method of Geometric Regularization of Vascular Segmentation in Medical Images," *IEEE Transacation on Image Processing,* vol. 17, pp. 1295-1312, 2008.

[96] J. Weickert, *Anisotropic Diffusion in Image Processing*. Stuttgart, Germany: Teubner-Verlag, 1998.

[97] R. Manniesing, M. A. Viergever, and W. J. Niessen, "Vessel Axis Tracking Using Topology Constrained Surface Evolution," *IEEE Transacation on Medical Imaging,* vol. 26, pp. 309-316, 2007.

[98] D. Mumford and J. Shah, "Optimal Approximations by Piecewise Smooth Functions and Associated Variational Problems," in *Proc. of Communications on Pure and Applied Mathematics*, 1989, pp. 577-685.

[99] S. C. Zhu and A. Yuille, "Region Competition: Unifying Snakes, Region Growing and Bayes/MDL for Multiband Image Segmentation," *IEEE Transacation on Pattern Analysis and Machnie intelligence,* vol. 18, pp. 884-900, 1996.

[100] T. F. Chan and L. A. Vese, "A Multiphase Level Set Framework for Image Segmentation Using the Mumford and Shah Model," *International Journal of Computer Vision,* vol. 50, pp. 271-293, 2002.

[101] M. Rousson, C. Lenglet, and R. Deriche, "Level Set and Region Based Surface Propagation for Diffusion Tensor MRI Segmentation " in *Proc. of Computer Vision Approaches to Medical Image Analysis (CVAMIA) and Mathematical Methods in Biomedical Image Analysis (MMBIA) Workshop*, 2004, pp. 123-134.

[102] F. Lecellier, S. Jehan-Besson, and M. Revenu, "Region based Active Contours with Exponential Family Observations," *Journal of Mathematical Imaging and Vision,* pp. 28-45, 2010.

[103] O. Michailovich, Y. Rathi, and A. Tannenbaum, "Image Segmentation Using Active Contours Driven by the Bhattacharyya Gradient Flow," *IEEE Transacation on Image Processing,* vol. 16, pp. 2787-2801, 2007.

[104] J. Kim, J. Fisher, A. Yezzi, M. Cetin, and A. Willsky, "A Non-parametric Statistical Methods from Image Segmentation using Information Theory and Curve Evolution," *IEEE Transacation on Image Processing,* vol. 14, pp. 1486-1502, 2005.

[105] C. Li, C. Y. Kao, J. C. Gore, and Z. Ding, "Implicit Active Contours Driven by Local Binary Fitting Energy," in *Proc. of IEEE Conference on Computer Vision and Pattern Recognition*, 2007, pp. 1-7.

[106] C. Li, C. Y. Kao, J. C. Gore, and Z. Ding, "Minimization of Region Scalable Fitting Energy for Image Segmentation," *IEEE Transacation on Image Processing,* vol. 17, pp. 1940-1949, 2008.

[107] L. Wang, L. He, A. Mishra, and C. Li, "Active Contours Driven by Local Gaussian Distribution Fitting Energy," *Signal Processing,* vol. 89, pp. 2435-2447, 2009.

[108] C. Darolti, A. Mertins, C. Bodensteiner, and U. G. Hofmann, "Local Region Descriptors for Active Contours Evolution," *IEEE Transacation on Image Processing,* vol. 17, pp. 2275-2288, 2008.

[109] S. Lankton and A. Tannenbaum, "Localizing Region-Based Active Contours," *IEEE Transacation on Image Processing,* vol. 17, pp. 2029-2039, 2008.

[110] J. Piovano and T. Papadopoulo, "Local Statistic Based Region Segmentation with Automatic Scale Selection," in *Proc. of 10th European Conference on Computer Vision Part II*, 2008, pp. 486-499.

[111] J. A. Sethian, "Evolution, Implementation, and Application of Level Set and Fast Marching Methods for Advancing Fronts," *Journal of Computational Physics,* vol. 169, pp. 503-555, 2001.

[112] C. Li, C. Xu, C. Gui, and M. D. Fox, "Level Set Evolution Without Re-initialization: A New Variational Formulation," in *Proc. of IEEE International Conference on Computer Vision and Pattern Recognition (CVPR)*, San Diego, 2005, pp. 430-436.

[113] V. Cheng*, et al.*, "Moving Beyond Binary Grading of Coronary Arterial Stenoses on Coronary Computed Tomographic Angiography: Insights for the Imager and Reffering Clinician," *Journal of the American College of Cardiology on Cardiovascular Imaging,* vol. 1, pp. 460-471, 2008.

[114] R. L. Raff, M. J. Gallagher, W. W. O'Neill, and J. A. Goldstein, "Diagnostic Accuracy of Noninvasive Coronary Angiography using 64-slice Sprial Computed Tomography," *Journal of Am Coll Cardiol,* vol. 46, pp. 552-557, 2005.

[115] S. B. Joshi*, et al.*, "Accuracy of Computed Tomographic Aniography for Stenosis Quantification Using Quantitatice Coronary Angiography or Intravascular Ultrasound as the Gold Standard," *Journal of the American College of Cardiology,* vol. 104, pp. 1047-1051, 2009.

[116] M. J. Boogers*, et al.*, "Automated Quantification of Stenosis Severity on 64-Slice CT," *Journal of the American College of Cardiology on Cardiovascular Imaging,* vol. 3, pp. 699-709, 2010.

[117] A. Kanitsar, D. Fleischmann, R. Wegenkittl, and P. Felkel, "CPR - curved planar reformation," in *IEEE Visualization 2002*, Boston, MA,USA, 2002, pp. 37-44.

[118] W. C. K. Wong and A. C. S. Chung, "Augmented Vessel for Quantitative Analysis of Vascular Abnormalities and Endovascular Treatment Planning," *IEEE Transacations on Medical Imaging,* vol. 25, pp. 665-684, 2006.

[119] W. C. K. Wong and A. C. S. Chung, "Probabilistic Vessel Axis Tracing and its Application on Vessel Segmentation with Stream Surface and Minimum Cost Paths," *Medical Image Analysis,* vol. 11, pp. 567-587, 2007.

[120] D. G. Kang, D. C. Suh, and J. B. Ra, "Three dimensional Blood Vessel Quantification via Centerline Deformation," *IEEE Transacations on Medical Imaging,* vol. 28, pp. 405-414, 2009.

[121] S. Ramcharitar, Y. Onuma, J. Aben, and C. Consten, "A Novel Dedicated Quantitative Coronary Analysis Methodology for Bifurcation Lesions," *EureIntervention,* vol. 3, pp. 553-557, 2008.

[122] S. Ramcharitar, J. Daeman, M. Patterson, and R. J. v. Guens, "First Direct in vivo Comparison of Two Commercially Available Three-Dimensional Quantitative Coronary Angiography Systems," *Catheterization and Cardiovascular Interventions,* vol. 71, pp. 44-50, 2008.

[123] M. Jiang, G. Wang, M. W. Skinner, J. T. Rubinstein, and M. W. Vannier, "Blind Deblurring of Spiral CT Images," *IEEE Transacation on Medical Imaging,* vol. 22, pp. 837-845, 2003.

[124] E. R. Hijarrubia, R. Manniesing, and W. J. Niessen, "Selective Deblurring for Imporved Calcification Visualization and Quantification in Carotid CT Angiography: Validation Using Micro-CT," *IEEE Transacation on Medical Imaging,* vol. 28, pp. 446-453, 2009.

[125] R. C. Gonzalez and R. E. Woods, *Digital Image Processing*, 2nd ed. New Jersey, USA: Prentice Hall, 2002.

[126] H. E. Cline*, et al.*, "Automated Coronary CT Angiography Plaque-lumen Segmentation," in *Proc. of SPIE on Medical Imaging*, Lake buena Vista, FL, USA, 2009, pp. 1-10.

[127] D. D. Cody, "AAPM/RSNA Physcis Tutorial for Residents: Topics in CT," *Radio Graphics,* vol. 22, pp. 1255-1268, 2002.

[128] J. T. Bushberg, *The Essential Physics of Medical Imaging*, 2nd ed. Philadelphia, PA, USA Lippincott Williams & Wilkins, 2002.

[129] K. Ibukuro, C. Charnsagavej, M. Chasen, and A. Cinqualbre, "Helical CT Angiography with Multiplanar Reformation: Techniques and Clinical Applications," *Radio Graphics,* vol. 15, p. 671, 1995.

[130] E. Caoili and E. Paulson, "CT of Small-bowel Obstruction: Another Perspective using Multiplanar Reformations," *American Journal of Roentgenology,* vol. 174, pp. 993-998, 2000.

[131] P. T. Johnson, E. K. Fishman, J. R. Duckwall, P. S. Cahoun, and D. G. Heath, "Ineractive Three-dimensional Volume Rendering of Spiral CT Data: Current Application to the Thorax," *RadioGraphics,* vol. 18, pp. 165-187, 1998.

[132] D. S. Ebert, D. G. Heath, and B. S. Kuszyk, "Evaluatiing the Potential of Problems of Three Dimensional Computed Tomography Measurments of Arterial Stenosis," *Journal of Digital Imaging,* vol. 11, pp. 151-157, 1998.

[133] D. M. Coll, B. R. Herts, W. J. Davros, R. G. Uzzo, and A. C. Novick, "Preoperative use of 3D Volume Rendering to Demonstrate Renal Tumors and Renal Anatomy," *Radio Graphics,* vol. 20, pp. 431-438, 2000.

[134] P. Koopman, "Bresenham Line-Drawing Algorithm," *Forth Dimensions,* vol. 8, pp. 12-16, 1987.

[135] C. Kimme, B. H. Ballard, and J. Sklansky, "Finding Circles by an Array of Accumulators," *Communications of the Association for Computing Machinery,* vol. 18, pp. 120-122, 1975.

[136] A. P. Dempster, N. M. Laird, and D. B. Rubin, "Maximum Likelihood from Incomplete Data via the EM Algorithm," *Journal of the Royal Statistical Society,* vol. 39, pp. 1-38, 1977.

[137] G. Grieg, O. Kubler, R. Kikinis, and F. A. Jolesz, "Nonlinear Anisotropic Filtering of MRI Data," *IEEE Transacation on Medical Imaging,* vol. 11, pp. 221-232, 1992.

[138] R. T. Whitaker, "A Level Set Approach to 3D Reconstruction from Range Data," *International Journal of Computer Vision,* vol. 29, pp. 203-231, 1998.

[139] T. Brox and J. Weickert, "Level Set Segmentation with Multiple Regions," *IEEE Transacation on Image Processing,* vol. 15, pp. 3213-3218, 2006.

[140] A. Zijdenbos, B. Dawant, R. Margolin, and A. Palmer, "Morphometric Analysis of White Matter Lesions in MR Images: Methods and Validation," *IEEE Transacation on Medical Imaging,* vol. 13, pp. 716-724, 1994.

[141] J. Drexl, V. Knappe, H. K. Hahn, and K. S. Lehmann. (2001, Accuracy Analysis of Vessel Segmentation for a Lift Dosimetry Planning System. *Perspective In Image-Guided Surgery.*

[142] R. T. Rockafellar and R. J.-B. Wets, *Variational Analysis* vol. 317. New York, NY, USA: Springer Press, 1998.

[143] W. Lorensen and H. E. Cline, "Marching Cubes: A High Resolution 3D Surface Construction Algorithm," *Computer Graphics,* vol. 21, pp. 163-170, 1987.

[144] O. K.-C. Au, C.-L. Tai, H.-K. Chu, D. Cohen-Or, and T.-Y. Lee, "Skeleton Extraction by Mesh Contraction," in *Proc. of SIGGRAPH '08 ACM SIGGRAPH 2008* New York, NY, USA, 2008, pp. 1-10.

[145] A. F. Frangi, W. Niessen, R. M. Hoogeveen, and M. A. Viergever, "Model Based Quatitiation of 3-D Magnetic Resonance Angiographic Images," *IEEE Transacation on Medical Imaging,* vol. 18, pp. 946-956, 1999.

[146] A. F. Frangi*, et al.*, "Quantitative Analysis of Vascular Morphology from 3D MR Angiograms: In Vitro and in Vivo Results," *Magnetic Resonance in Medicine,* vol. 45, pp. 311-322, 2001.

[147] P. J. Yim, J. J. Cebral, R. Mullick, H. B. Marcos, and P. L. Choyke, "Vessel Surface Reconstruction with a Tubular Deformable Model," *IEEE Transacation on Medical Imaging,* vol. 20, pp. 1411-1421, 2001.

[148] P. J. Yim, R. Mullick, H. B. Marcos, and P. L. Choyke, "Measurement of Stenosis from Magnetic Resonance Angiography using Vessel Skeletons," in *Medical Imaging 2000: Physiology and Function from Multidimensional Images*, 2000, pp. 245-255.

[149] W. Gander, G. H. Golub, and R. Strebel, "Least-Squares Fitting of Circles and Ellipses," *BIT Numerical Mathematics,* vol. 34, pp. 558-578, 1995.

[150] E. O. Kung*, et al.*, "In Vitro Validation of Finite Element Analysis of Blood Flow in Deformable Models," *Annals of Biomedical Engineering,* vol. 39, pp. 1947-1960, 2011.

[151] T. F. Coleman and Y. Li, "Trust Region Approach for Nonlinear Minimization Subject to Bounds," *SIAM Journal on Optimization,* vol. 6, pp. 418-445, 1996.

[152] T. F. Coleman and Y. Li, "On the Convergence of Reflective Newton Methods for Large-Scale Nonlinear Minimization Subject to Bounds," *Mathematical Programming,* vol. 67, pp. 189-224, 1994.

[153] O. Goktekin, S. Kaplan, K. Dimopoulos, P. Barlis, and J. Tanigawa, "A New Quantitative Analysis System for the Evaluation of Coronary Bifurcation Lesions: Comparison with Current Conventional Methods," *Catheterization and Cardiovascular Interventions,* vol. 69, pp. 172-180, 2007.

[154] W. Wang and B. Joe, "Robust Computation of the Rotation Minimizing Frame for Sweep Surface Modeling," *Computer-Aided Design,* vol. 29, pp. 379-391, 1997.

[155] S. S. Rao, *Engineering Optimization Theory and Practice*, Fourth Edition ed. Hoboken, NJ, USA: John Wiley & Sons. INC., 2009.

[156] C.-t. Kim and J.-J. Lee, "An Active Contour Model for Object Tracking using the Previous Contour," *Artif Life Robotics,* vol. 7, pp. 6-11, 2003.

[157] J. Yan, K. Zhang, C. ZHang, S.-C. Chen, and G. Narasimhan, "A Graph Reduction method for 2D Snake Problems," in *Proc. of 2007 IEEE Conference on Computer Vision and Pattern Recognition*, Minneapolis, USA, 2007, pp. 1-6.

[158] A. A. Amini, T. E. Weymouth, and R. C. Jain, "Using Dynamic Programming for Solving Variational Problems in Vision," *IEEE Transactions on Pattern Analysis and Machine intelligence,* vol. 12, pp. 855-867, 1990.

[159] VMTK. *Vascular Modeling Toolkit*. Available: http://www.vmtk.org/

[160] 3DSlicer. Available: http://www.slicer.org/

[161] Y. Wang and P. Liatsis, "A Fully Automated Framework for Segmentation and Stenosis Quantification of Coronary Arteries in 3D CTA Images," in *Proc. of Developments in eSystems Engineering* Abu Dhabi, 2009, pp. 136-140.

[162] Y. Wang and P. Liatsis, "An Automated Method for Segmentation of Coronary Arteries in Coronary CT Imaging," in *Proc. of Third International Conference on Developments in eSystems Engineering (DeSE '2010)*, London,United Kingdom, 2010, pp. 12-16.

[163] Y. Wang and P. Liatsis, "Automated Segmentation of Coronary Arteries in 3D CTA Images by Considering Kissing Vessel Artifacts," *IEEE Transactions on Information Technology in Biomedicine, Submitted for Review,* 2011.

[164] Y. Wang and P. Liatsis, "3D Quantitative Vascular Shape Analysis for Arterial Bifurcations via Dynamic Tube Fitting," *IEEE Transactions on Biomedical Engineering, under second review,* 2011.

[165] X. Qian*, et al.*, "A Non-parametric Vessel Detection Method for Complex Vascular Structures," *Medical Image Analysis,* vol. 13, pp. 49-61, 2008.

[166] V. R. Ratnaparkhe, R. R. Manthalkar, and Y. V. Joshi, "Texture Characterization of CT Images Based on Ridgelet Transform," *International Journal on Graphics, Vision and Image Processing* vol. 8, pp. 1-11, 2009.

[167] P. A. L. Tonino*, et al.*, "Fractional Flow Reserve versus Angiography for Guiding Percutaneous Coronary Intervention," *New England Journal of Medicine* vol. 360, pp. 213-224, 2009.

[168] B.-K. Koo, "Pre-Catheterisation Treatment Planning using Coronary Computed Tomography Angiography and Computational Assessment of Fractional Flow Reserve " in *Proc. of EuroPCR 2011* Pairs, France, 2011.